

Electronic Thesis and Dissertation Repository

10-4-2022 11:00 AM

Finite Element Analysis of Conductive Carbon-Based Thin Films Modified by Ultrashort Pulsed Laser Processing

Andrew Dwyre, *The University of Western Ontario*

Supervisor: Knopf, George K., *The University of Western Ontario*

A thesis submitted in partial fulfillment of the requirements for the Master of Engineering Science degree in Mechanical and Materials Engineering

© Andrew Dwyre 2022

Follow this and additional works at: <https://ir.lib.uwo.ca/etd>

Recommended Citation

Dwyre, Andrew, "Finite Element Analysis of Conductive Carbon-Based Thin Films Modified by Ultrashort Pulsed Laser Processing" (2022). *Electronic Thesis and Dissertation Repository*. 8897.
<https://ir.lib.uwo.ca/etd/8897>

This Dissertation/Thesis is brought to you for free and open access by Scholarship@Western. It has been accepted for inclusion in Electronic Thesis and Dissertation Repository by an authorized administrator of Scholarship@Western. For more information, please contact wlsadmin@uwo.ca.

Abstract

A COMSOL Multiphysics simulation study on the relationship between ultrashort pulsed laser process parameters and the thermal modification of conductive carbon-based (e.g., graphite, graphene) thin films is presented in this thesis. The research objective is to utilize the theoretical models of heat transfer in thin films with finite element analysis (FEA) techniques to understand the impact of laser process parameters on the heat affected zone (HAZ) profile when an ultrashort pulsed laser beam strikes a thin conductive carbon film deposited on a polymer substrate. The goal is to be able to anneal or ablate the carbon-based films without causing thermal or structural damage to the underlying substrate. The laser process parameters include wavelength, pulse width, pulse energy, and beam diameters. In this study, the two-temperature model (TTM) and multi-temperature model (MTM) are examined in detail for different types of graphene layered films. The simulation experiments demonstrate that TTM is a suitable model for highly oriented pyrolytic graphite (HOPG) and reduced graphene oxide (rGO) films, whereas MTM is more appropriate for modeling single layer graphene. The impact of laser wavelength on surface annealing and ablation on graphite (HOPG) and graphene derivative films on different substrates is explored in greater detail. The simulation results are compared with experimental observations reported in the published literature and found to be a realistic reflection of the physical processes. The FEA study provides the groundwork for using ultrashort laser pulses to anneal carbon-based conductive films and electrodes, micromachine printed films to remove excess material, and to reduce the thickness of functional layers. Furthermore, laser thermal processing represents an environmentally benign method of creating a wide variety of single-use disposable electrical and electrochemical sensors for healthcare, food safety inspection, intelligent packaging, environmental monitoring, and public security.

Keywords

Laser material processing, COMSOL Multiphysics, ultrashort laser ablation, ultrashort laser annealing, finite element analysis, graphite, graphene, two-temperature model, laser processing efficiency

Summary for Lay Audience

Graphene oxide (GO) is an electrically insulating material that can be printed onto a polymer substrate, and using a pulsed laser, the film can be annealed to improve electrical conductivity producing reduced graphene oxide (rGO) or micromachined to reduce the thickness and remove excess material. The laser parameters must be precisely controlled to achieve the desired result and their influence on the temperature distribution and material removal in GO are not well understood. This thesis presents numerical simulations using the software COMSOL Multiphysics to investigate the impact of different laser parameters on the annealing and material removal of GO and rGO respectively. Preliminary simulations are performed on graphite (HOPG) and compared to physical experiments which are found to be in good agreement at certain fluences. Simulations are then performed on rGO for a range of laser parameters to determine the ideal parameters for material removal and annealing. An analysis of different substrates is also conducted to determine the amount of substrate damage experienced during laser micromachining. Overall, the models presented in this thesis can offer time and cost savings to realize processing parameters for carbon-based electronics and help to better understand laser-material interaction required for their fabrication.

Acknowledgments

This research would not be possible without the support of my supervisor, Dr. Knopf, and my colleagues, family, and friends. I would like to acknowledge the Department of Mechanical and Materials Engineering at Western University and the NSERC Discovery Grant program for financial support. I would also like to acknowledge the support of CMC Microsystems (Kingston, Ontario) in providing access to the COMSOL Multiphysics software through their Designer subscription programs.

Table of Contents

Abstract	ii
Keywords	ii
Summary for Lay Audience	iii
Acknowledgments	iv
Table of Contents	v
List of Figures	viii
List of Tables	xii
List of Appendices	xiii
Nomenclature	xiv
Chapter 1 Introduction	1
1.1 The Research Problem	2
1.2 Applications to Laser Annealing and Ablation	3
1.3 Research Motivation and Objectives	3
1.4 Overview of the Thesis	4
Chapter 2 Literature Review of Laser-Material Interaction and Graphene Properties ...	5
2.1 The Heat Equation	5
2.2 Optical Absorption and Laser Micromachining	6
2.3 Overview of Graphite, Graphene and Graphene Derivatives	19
2.3.1 Graphene Oxide	20
2.3.2 Thermal Properties of Graphene	22
2.3.3 Optical Properties of Graphene	25
2.4 Graphene Synthesis	28
2.5 Graphite Ablation Experiments	29
2.6 Graphene Phonon Properties	32
2.7 Graphene Ablation Experiments	33
2.7.1 Printed Graphene-Oxide (GO) Ablation Experiments	36
2.7.2 Graphene-Oxide (GO) Annealing Experiments	37
2.8 Mathematical Models for Laser Ablation	40
2.9 Concluding Remarks	42
Chapter 3 Finite Element Analysis of Ultrashort Laser Pulses Irradiating Graphitic Materials	43
3.1 Introduction	43
3.2 Finite Element Modelling (FEM)	43

3.3	COMSOL Multiphysics	44
3.4	Two Temperature Model (TTM).....	46
3.5	Laser Ablation of Highly Oriented Pyrolytic Graphite (HOPG)	49
3.5.1	Equations Describing Laser Beam Intensity	49
3.5.2	HOPG Modelling Domain	50
3.5.3	Material Properties of HOPG Films	52
3.6	Simulation Study of Irradiating HOPG Films.....	56
3.6.1	Boundary and Initial Conditions.....	58
3.6.2	Meshing Parameters.....	58
3.6.3	Solver Settings	60
3.6.4	Model Assumptions	61
3.6.5	Simulation Results for Laser Ablation of HOPG Thin Film	61
3.7	Concluding Remarks	69
Chapter 4	Finite Element Analysis of Ultrashort Laser Pulses Irradiating Graphene-Derivative Films.....	70
4.1	Reduced Graphene Oxide (rGO) Materials.....	70
4.1.1	Laser Parameters and Reduced Graphene Oxide (rGO) Material Properties ..	70
4.1.2	rGO Simulation Results	74
4.2	Single Layer Graphene (SLG).....	79
4.2.1	Multi-temperature Model (MTM).....	79
4.2.2	SLG Modelling Domain	81
4.2.3	Material Properties of SLG and Laser Parameters.....	82
4.2.4	Simulation Study of Irradiating SLG	83
4.3	Concluding Remarks	90
Chapter 5	Impact of Laser Parameters on Annealing, Ablation and Substrate	91
5.1	Introduction	91
5.2	Laser Wavelength Analysis.....	91
5.3	Substrate Damage Analysis.....	95
5.4	Ablation Efficiency	99
5.5	Annealing Efficiency.....	105
5.6	Concluding Remarks	109
Chapter 6	Conclusions.....	111
6.1	Research Outcomes	111
6.2	Contributions.....	112

6.3 Future Research.....	113
References.....	115
Appendix.....	124
Appendix A: Preliminary Simulation Results.....	124
A.1: Stainless Steel Ultrashort Laser Ablation	124
Curriculum Vitae	126

List of Figures

Figure 2.1 Timescales of processes in ultrashort laser irradiation [15].	9
Figure 2.2 Single-photon absorption (a) and multiphoton absorption (b).	10
Figure 2.3 Schematic drawing showing the impact ionization process.	11
Figure 2.4 Carrier-carrier scattering (a) and carrier-phonon scattering showing intervalley and intravalley scattering (b).	12
Figure 2.5 Carrier recombination mechanisms. (a) radiative recombination (b) Auger recombination (with electron) (c) Auger recombination (with hole) (d) defect and surface recombination	14
Figure 2.6 A comparison of HAZs for long pulse and femtosecond pulse lasers.....	18
Figure 2.7 Molecular structure of graphene oxide [23].	21
Figure 2.8 (a) In-plane thermal conductivity for multilayer graphene sheets (b) c-axis thermal conductivity for multilayer graphene sheets (Reprinted with permission from Appl. Phys. Lett. 104, 031903 (2014), Copyright 2014 AIP).....	23
Figure 2.9 Specific heat capacity for graphene layer number with temperature (Reprinted with permission from Appl. Phys. Lett. 104, 031903 (2014), Copyright 2014 AIP).	24
Figure 2.10 Reflectivity spectrum of HOPG (a) and optical penetration depth of HOPG (b).	26
Figure 2.11 Reflectivity spectrum of printed rGO and (a) and optical penetration depth of printed rGO (b).	27
Figure 2.12 Single pulse ablation depth on HOPG as a function of energy fluence and pulse width (Reprinted with permission from [45], Copyright 2001 Elsevier).	31
Figure 2.13 Calculated percentage of energy flow for carriers in laser irradiated graphene (Reprinted with permission from [51], Copyright 2016 American Physical Society).....	33
Figure 2.14 Peak intensity and fluence threshold on SLG as a function of pulse duration (Reprinted with permission from [52], Copyright 2018 AIP).	34
Figure 2.15 Change in graphene oxide electrical resistance and temperature with time (Reprinted with permission from [25] Copyright 2008 American Chemical Society).....	37
Figure 2.16 Temperature ranges and processes for thermal reduction of GO © 2011, Seung Hun Huh. Originally published in [10] under Creative Commons Attribution-NonCommercial-ShareAlike-3.0 license. Available from: 10.5772/14156.....	38

Figure 2.17 Sheet resistance of rGO as a function of laser intensity corresponding to grayscale color from laser program (Reprinted with permission from [26], Copyright 2012 American Chemical Society).	39
Figure 2.18 Sheet resistance of rGO as a function of number of laser passes, laser power and scan speed © [2014] IEEE. Reprinted, with permission, from [Sinar et al., Laser assisted reduction of printed GO films and traces]	40
Figure 3.1 Predefined heat transfer modules in COMSOL Multiphysics.	45
Figure 3.2 Magnitude of the pulse $P(t)$ over time for 120 fs pulse.	50
Figure 3.3 Visualization of the domain for 1D and 2D axisymmetric.	51
Figure 3.4 (a) 1D domain representing the material depth at the centre of the laser spot. (b) Illustration of 1D and 2D modelling domains. Figure 3.4a is oriented next to the illustration and represents the axis of 1D heat transfer.	51
Figure 3.5 2D axisymmetric model domain where the heat source is applied to the surface 3. Red line shows 1D domain.	52
Figure 3.6 Temperature dependent c-axis electron thermal conductivity of HOPG.	54
Figure 3.7 Temperature dependent ab-plane electron thermal conductivity HOPG.	54
Figure 3.8 Temperature dependent electron specific heat capacity HOPG.	55
Figure 3.9 50 element mesh for 1D model representing the depth at the center of the laser spot. 0 μm represents the material surface where elements are closer together.	59
Figure 3.10 Mesh for 2D axisymmetric model representing one half of the irradiated material. A length to depth scale of 1: 20 is used. Center of laser spot is applied at the origin where elements are distributed closer to.	60
Figure 3.11 Electron and lattice temperatures over time for 4.2 J/cm ² laser ablation of HOPG.	62
Figure 3.12 Electron temperatures with respect to depth at different times.	63
Figure 3.13 Lattice temperatures with respect to depth at different times.	63
Figure 3.14 Single pulse ablation depth of HOPG for different fluences in simulation and experiment described by Shirk et al. [45].	64
Figure 3.15 Multiple pulse ablation depth of HOPG at 2.1 J/cm ² for simulation and experiment.	66

Figure 3.16 Multiple pulse ablation depth of HOPG at $4.2 J/cm^2$ for simulation and experiment.....	66
Figure 3.17 Multiple pulse ablation depth of HOPG at $10.6 J/cm^2$ for simulation and experiment.....	67
Figure 3.18 Illustration of the full cross-section crater profile with incident laser beam. The 2D axisymmetric domain is highlighted.....	68
Figure 3.19 2D crater profile of HOPG after single pulse at $4.2 J/cm^2$	68
Figure 4.1 Typical surface roughness of printed rGO film [60].	71
Figure 4.2 Temperature dependent electron thermal conductivity for printed rGO.	73
Figure 4.3 Temperature dependent electron specific heat capacity for printed rGO.	73
Figure 4.4 Electron and lattice temperatures at surface of printed rGO for $1.2 \mu J$ pulse energy and effective pulse number of 0.97.	75
Figure 4.5 Electron temperatures with respect to depth at different times during simulation.....	76
Figure 4.6 Lattice temperatures with respect to depth at different times during simulations.	77
Figure 4.7 Simulated 2D crater profile after laser irradiation. 6:1 depth to length ratio. .	78
Figure 4.8 Ablation depth with respect to effective pulse number for 250, 500, 750 and 1000 Hz pulse repetition rate.	79
Figure 4.9 Modelling domain for SLG with 2500:1 depth to length ratio.....	81
Figure 4.10 Meshing for SLG domain with 50 elements.....	85
Figure 4.11 Phonon branch resolved temperature plot for laser irradiation of SLG.	86
Figure 4.12 Temperature plot comparing the thermal lattice reservoir temperature and weighted average phonon temperature for SLG irradiation.....	87
Figure 4.13 Temperature plot for TTM of SLG irradiation.	88
Figure 4.14 MTM weighted phonon average temperature plot at the point of equilibrium.	89
Figure 4.15 TTM lattice temperature at the point of equilibrium.	90
Figure 5.1 Single pulse ablation depth of HOPG at $5.2 J/cm^2$ for different wavelengths.	92

Figure 5.2 Single pulse ablation depth of HOPG with respect to fluence for different wavelengths.....	93
Figure 5.3 Single pulse ablation depth at different fluences for printed rGO.....	94
Figure 5.4 Single pulse ablation depth of printed rGO with respect to fluence for different wavelengths.....	95
Figure 5.5 Length of damaged substrate with respect to pulse energy for different substrates.....	97
Figure 5.6 Comparison of single pulse ablation depth-fluence curves for simulated rGO and HOPG and experimental HOPG.	101
Figure 5.7 Simulated cross-sectional area of ablation for rGO using different beam radii.	103
Figure 5.8 Simulated volume removal rate of rGO using different beam radii.	104
Figure 5.9 Simulated cross-sectional area of annealing for rGO using different beam radii.	107
Figure 5.10 Simulated volume annealing rate of rGO using different beam radii.....	108
Figure 5.11 Time at which the cross-sectional area of rGO remain above 1000 K for different beam radii.....	109

List of Tables

Table 3.1	HOPG material properties.....	57
Table 3.2	Laser parameters for experiment by Shirk et al. [45].	57
Table 4.1	Laser parameters of Sinar experiment [74].....	74
Table 4.2	Derived laser parameters for rGO simulation.	75
Table 4.3	Phonon branch properties for SLG [76].....	82
Table 4.4	Laser parameters from Roberts' experiment [52].	83
Table 5.1	Thermal properties of common substrates for printed electronics.....	97
Table 5.2	Results of substrate damage simulations.	99
Table 5.3	Adjusted laser parameters for rGO and HOPG comparison.	100
Table 5.4	Laser parameters used for Sinar experiment [74].	103

List of Appendices

Appendix A: Preliminary Simulation Results.....124

Nomenclature

Abbreviations

HOPG	highly oriented pyrolytic graphite
SLG	single layer graphene
BLG	bilayer graphene
TLG	trilayer graphene
MLG	multilayer graphene
GO	graphene oxide
rGO	reduced graphene oxide
CVD	chemical vapour deposition
DoD	drop-on-demand
FEM	finite element modelling
FEA	finite element analysis
TTM	two temperature model
MTM	multitemperature model
R.T.	room temperature
RTA	relaxation time approximation
PDE	partial differential equation
CW	continuous wave
HAZ	heat affected zone
CTE	coefficient of thermal expansion
SEM	scanning electron microscopy
AFM	atomic force microscopy
W/m·K	watts per metre per kelvin

$J/kg \cdot K$	joules per kilogram per kelvin
J/cm^2	joules per square centimeter
W/cm^2	watts per square centimeter

Variables and Constants

A	absorptivity
b	distance between pulses
C'_e	electron heat capacity constant
C_e	electron specific heat capacity
C_l	lattice specific heat capacity
C_m	speed of rarefaction wave
C_p	specific heat capacity
D	heat diffusion coefficient
d	laser spot diameter
E_g	bulk bandgap energy
E_p	pulse energy
e	Euler's constant
F	laser fluence
F_{th}	laser fluence threshold
$F_{th}(1)$	single pulse fluence threshold
$F_{th}(N)$	multiple pulse fluence threshold
F_{th2}	fluence threshold for 2nd fluence regime
f	pulse frequency
f_H	Heaviside step function

G_{ep}	electron-phonon coupling constant
G_{pp}	phonon-phonon coupling coefficient
I_0	incident laser intensity
k	thermal conductivity
k_{AB}	in-plane thermal conductivity
k_B	Boltzmann constant
k_C	cross-plane lattice thermal conductivity
k_e	electron thermal conductivity
k_{e0}	electron thermal conductivity at ambient temperature
k_{eAB}	in-plane electron thermal conductivity
k_{eC}	cross-plane electron thermal conductivity
k_l	lattice thermal conductivity
k_{LAB}	in-plane lattice thermal conductivity
k_{lC}	cross-plane lattice thermal conductivity
k_p	phonon thermal conductivity
k	extinction coefficient
L_0	Lorenz constant
L	ablation depth per pulse
l_d	diffusion length
l_e	electron energy transfer depth
l_p	optical penetration depth
l_{p2}	optical penetration depth for 2 nd fluence regime
N_A	Avagadro's number
N_e	electron density

N_{eff}	effective pulse number
N	number of pulses
n	refractive index
O	pulse overlap
P_{ave}	average laser power
Q	heat source
Q'	linear heat source
q	heat flux per unit area
R	reflectivity
r	radial coordinate
T	temperature
T_F	Fermi temperature
T_c	critical temperature
T_e	electron temperature
T_g	glass transition temperature
T_l	lattice temperature
T_{lat}	thermal lattice reservoir temperature
T	transmissivity
t	time
t_s	thickness of material
U	energy density
v	laser scanning speed
v_F	Fermi velocity
z	depth coordinate

λ_E	mean free path of charge carriers
τ_m	mechanical relaxation time
τ_p	pulse width
ω_0	beam spot radius
Θ	Debye temperature
α	linear absorption coefficient
ζ	incubation coefficient
ρ	density
σ	electrical conductivity

Chemicals and Materials

Ar	argon
C	carbon
Ge	germanium
H	hydrogen
H ₂ O	water
NO ₂	nitrogen dioxide
PDMS	polydimethylsiloxane
PET	polyethylene terephthalate
PLA	polylactic acid
PMMA	polymethyl methacrylate
Pt	platinum
PVA	polyvinyl alcohol
Si	silicon

SiO ₂	silicon dioxide
Ti:sapphire	titanium-sapphire

Chapter 1 Introduction

The recent emergence of 2D materials, a material consisting of a single atomic crystalline layer, has inspired extensive research into their potential applications from transparent conductive electrodes to water filtration systems. The 2D nature of these materials give rise to properties such as a high strength-to-weight ratio from the removal of interlayer van der Waals forces, a high sensitivity due to a large surface-to-volume ratio, and a high electrical conductivity due to the confinement of electrons in a single plane. The concept of a 2D material was first modelled by Wallace *et al.* [1] in an attempt to explain the properties of graphite through monolayer graphene, however at the time it was believed that 2D materials were thermodynamically unstable and could not exist independently [2]. In 2004, Geim *et al.* [3] put an end to this notion by isolating single layer graphene through mechanical exfoliation and transferring it to a Si/SiO₂ substrate that weakly interacted with the graphene monolayer. Since its physical discovery, researchers have uncovered unique properties such as high electrical conductivity, thermal conductivity, Young's modulus and optical transparency making it an attractive material for many applications. The main challenge inhibiting graphene in its widespread use comes with its procurement as it is very difficult to produce high quality, high yield, and low-cost graphene.

One alternative method to producing graphene is through the reduction of graphene oxide (GO), an electrically insulating derivative of graphene, in which the oxygen functional groups can be removed from the graphene layer by chemical or thermal methods to produce reduced graphene oxide (rGO). In chemical reduction methods hydrazine is typically employed as a reagent and combined with thermal annealing in an Ar/H atmosphere. In a thermal reduction method, GO can be heated to temperatures between 200 and 1000 °C to remove the functional groups, however in both methods complete removal of functional groups can not be achieved which results in properties closer to but not exactly those of pristine graphene. Still, the reduction of GO to rGO is capable of producing a scalable and inexpensive derivative of graphene with excellent electrical, mechanical and thermal properties.

Recent work has been conducted to investigate the process of using exfoliated 2D materials to produce low-cost and scalable functional inks which can be inkjet printed onto a variety of substrates. This concept was first introduced in 2012 by Torrisi *et al.* [4] who produced a liquid phase exfoliated graphene ink to create transparent thin film transistors. Since then, research has been conducted on inks using different 2D materials and solvents including GO using drop-on-demand (DoD) inkjet printing for printed electronics. Since GO is a hydrophilic material, it can be used to create a uniform ink dispersion that can be inkjet printed onto a substrate with high controllability. The thin film can then be altered using a laser to heat and remove functional groups and improve electrical conductivity or by using a more powerful pulsed laser certain areas of the thin film can be ablated to create microstructures. Using these processes, microelectronics such as transistors and interdigitated capacitors can be fabricated onto flexible substrates.

1.1 The Research Problem

The combination of functional graphene/GO inks and laser processing has been demonstrated for a range of applications in electronics including interdigitated capacitors [5], strain sensors [6], rapid heating chips [7], and electrodes [8]. By using a laser, conductive channels can be created on the deposited thin film with the conductivity being adjustable based on the exposure time and temperature of the film. A pulsed laser can also be used to micromachine desired areas to reduce the dimensional size of certain features or remove excess substrate. The desired patterning and annealing are sensitive to laser parameters such as wavelength, fluence, pulse frequency and scan speed and must be finetuned to obtain the desired results and ensure the underlying substrate is not damaged during laser processing. As of yet, a comprehensive study of the laser parameters on annealing and material removal efficiency for graphene thin films has not been conducted in previous literature. In physical experiments conducting a parametric study is impractical due to the high cost of equipment required to test the many parameters as well as the long preparation times and high costs required to produce the printed samples. Therefore, a numerical model can be employed to perform and analyze parametric studies on laser

processed printed graphene offering an inexpensive and efficient method of determining ideal laser parameters compared to physical experiments.

1.2 Applications to Laser Annealing and Ablation

Annealing is a heat treatment process that has been practiced for hundreds of years in which a material is heated above its recrystallization temperature and held at that temperature before being cooled. Laser annealing was first demonstrated in the 1980's on Si and Ge to recrystallize ion-implanted semiconductors [9]. During annealing, defects in the crystal lattice decrease resulting in a more ductile material. For the case of GO, heating the material to temperatures above 600° C causes evaporation of interlayer H₂O and removal of oxygen functional groups which produces rGO with properties approaching graphene [10]. Laser annealing of GO has been employed to produce rGO from amorphous carbon [11], convert p-type rGO to n-type rGO [12], and produce rGO from insulating polymers [13].

Laser micromachining is a process where photon energy from an incident laser beam is converted to thermal energy in a material to exceed a temperature threshold and remove material. The first laser cutting machine was demonstrated in 1965 to drill into diamond before commercial laser cutting applications became popular in the 1990's. In the case of graphene, laser micromachining has been used to produce microelectrodes for sensors from PLA-graphene, multilayer graphene films, and laser-induced forward transfer GO.

1.3 Research Motivation and Objectives

Although studies have been performed on laser annealing and micromachining of graphite and its derivatives, there has not been an extensive study on how laser parameters affect the annealing and ablation volume and their efficiency. There are also currently no numerical models concerning the ultrashort laser ablation of graphite or GO. It is believed that a numerical model would be a useful tool to determine the ablation outcome of graphite derivatives without the need for expensive and time-consuming physical experiments. It is also evident that a need exists for flexible and degradable electronics where graphene and rGO can prove to be useful and efficient laser processing parameters should be determined.

This research aims to develop numerical models for the annealing and ablation of highly oriented pyrolytic graphite (HOPG), reduced graphene oxide (rGO), and single-layer graphene (SLG) to analyze the effect of varying laser parameters on annealing and ablation quality. HOPG was first selected to validate the model with an experiment using a carbon-based material with well-known material properties. SLG was then modelled to serve as a single-layer derivative of HOPG and determine if a TTM would achieve sufficient results. Finally, printed rGO was modelled and validated by experiment to simulate micromachining and annealing. The laser parameters are optimized through the model to determine efficient annealing and ablation of printed carbon-based thin films.

1.4 Overview of the Thesis

This thesis is composed of six chapters, that discuss the developed numerical models with comparison to experimental results, as well as parametric studies that identify efficient laser parameters for annealing and ablation of HOPG and rGO thin films. Chapter 2 presents a literature review explaining the underlying concepts relating to laser material interaction as well as a state-of-the-art review in graphene properties, ablation experiments, annealing experiments, and mathematical models. Chapter 3 discusses the finite element model, their respective equations and assumptions, and the simulated results for HOPG with a comparison to published experiments. Chapter 4 applies the finite element model to printed rGO and extends the model for SLG with comments on the simulated results. Chapter 5 discusses the parametric simulations for various laser parameters and how these results relate to overall annealing and ablation processes. Efficient laser parameters are identified and the results for typical physical experiments are discussed. Finally, Chapter 6 presents conclusions of the thesis and summarizes critical future work to improve and build upon the ideas presented in the thesis.

Chapter 2 Literature Review of Laser-Material Interaction and Graphene Properties

The following literature review is intended to give the reader a basic understanding of the underlying physics and supporting equations in laser-matter interaction in order to interpret the results and conclusions presented in this thesis. A state-of-the-art review is provided concerning the properties of graphite and its derivatives, graphene synthesis, ablation and annealing experiments, and mathematical models.

2.1 The Heat Equation

The heat equation is a partial differential equation that governs heat transfer in a material without a phase change. The equation can be solved with appropriate parameters and conditions to determine the temperature distribution in space and time. The heat equation in one dimension (1D), assuming no radiation or convection, is given by

$$\rho C_p \frac{\delta T(z, t)}{\delta t} - \nabla \cdot k \nabla T(z, t) = Q' \quad (2.1)$$

where ρ is density (kg/m^3), C_p is the specific heat capacity ($\text{J}/\text{kg} \cdot \text{K}$), k is the thermal conductivity ($\text{W}/\text{m} \cdot \text{K}$), z is position, t is time, and Q' is the 1D heat source (W/m). The specific heat capacity represents the change in energy density U when the temperature changes by 1°K ,

$$C_p = \frac{dU}{dT} \quad (2.2)$$

Thermal conductivity is the measure of a materials ability to conduct heat and relates the heat flux per unit area, q , to the temperature gradient $q = -k\nabla T$. Using a boundary condition and an initial condition, the temperature distribution of the 1D system can be solved. For the case of laser irradiation at normal incidence to the material, the heat source, Q in W/m^3 , can be determined by

$$Q = \frac{2(1 - R)\alpha E_p}{\tau_p \pi \omega_0^2} \exp(-\alpha z) f_H\left(\frac{t}{t_p}\right) \exp\left(\frac{-2r^2}{w_0^2}\right) \quad (2.3)$$

where R is the reflection coefficient, α is the absorption coefficient (1/m), E_p is pulse energy (J), τ_p is pulse width (s), ω_0 is beam spot radius (m), f_H is a Heaviside step function, and r is the radial coordinate (m). The first term of the equation represents the total power absorbed by the material, the second term represents the exponential decay due to absorption corresponding to the Beer-Lambert law, the third term is a Heaviside step function representing the amplitude of the laser pulse in time, and the fourth term represents the laser distribution in space corresponding to a Gaussian distribution. The heat equation is applicable for short laser pulses, but for ultrashort pulses (< 10 ps) a separate set of equations must be used to account for the different temperatures of the lattice and electrons which is discussed in Section 3.4.

2.2 Optical Absorption and Laser Micromachining

Conventional machining operations like drilling, sawing, milling and welding have proven useful in the manufacturing of a variety of products and industries for many years, and although they are well established and sufficient to produce high throughput operations at a relatively low cost, they can have several limitations. Some of these limitations include tool wear that can lead to poor tolerances or unsafe procedures and can require tools to be replaced periodically. They also come up short when it comes to machining complex patterns and fine features and can be impossible to machine certain materials such as low melting or brittle materials. Laser micromachining offers a solution to these problems through the use of light-matter interaction. Lasers can enable a non-contact machining operation with high precision, excellent repeatability, no tool wear, and large variability in material applications.

Laser-matter interaction works on the basis of photons from the laser being absorbed by the material to promote electrons to a higher energy level. Since materials have unique sets of energy levels, the incident photon must be of that energy level to promote an electron dictated by the frequency of light. This results in different wavelengths of light from a laser

being favourable or unfavourable for absorption. Laser radiation can be absorbed by exciting free electrons or inducing transitions in atoms, molecules or ions. Although laser intensity at the surface in theory is the same as that from the laser output, the material causes a decay of laser intensity within the depth of the material. This phenomenon is characterized by the linear absorption coefficient, α , which depends on both the temperature of the material and wavelength of light. The optical penetration depth, l_p , is the inverse of α and represents the depth at which the light intensity becomes $1/e$ of its initial value, where e is Euler's constant. At constant α , the decay of laser intensity can be given by the Beer-Lambert Law

$$I(z) = I_0 e^{-\alpha z} \quad (2.4)$$

where I_0 is the incident laser intensity in W/m^2 accounting for reflection losses and z is the material depth in m. The linear absorption coefficient is a measure of how easily a material is penetrated by light and can be given by

$$\alpha = \frac{4\pi k}{\lambda} \quad (2.5)$$

where k is the extinction coefficient and λ is the laser light wavelength in m. The fraction of light absorbed by a material also depends on the fraction of light reflected and transmitted according to Equation (2.6) and is dependent on the material itself and surface roughness.

$$A = 1 - R - T \quad (2.6)$$

where A is absorptivity, the fraction of incident light absorbed by the material, R is reflectivity, the fraction of incident light reflected from the material, and T is transmissivity, the fraction of incident light transmitted by the material.

The reflectivity of a material can be calculated using Equation (2.7) under the conditions of an ambient atmosphere or vacuum.

$$R = \frac{(n - 1)^2 + k^2}{(n + 1)^2 + k^2} \quad (2.7)$$

where n is the refractive index. The reflectivity can be affected by a number of factors including the temperature and phase of the material, the roughness profile of the material,

and the polarization of incident light. Although the general principle for light absorption is common among all materials, the mechanisms change based on whether the material is a metal, semiconductor, dielectric or is optically transparent [14].

For the case of metallic materials, light absorption occurs due to electronic excitations that can be either intra- or interband transitions. For intraband transitions a conduction-band electron is excited and for interband transitions a valence electron is excited in which a specific energy value must be met relating to the energy of separation between the valence and conduction bands. For metals, the optical absorption occurs primarily due to intraband transitions where the excited free electrons then transfer their energy to phonons through electron-phonon collision, where a phonon is a quantized lattice vibration wave that carries thermal energy in a material. The plasma frequency of a metal relates the electron density of the metal to its dielectric function where at frequencies that are lower than the plasma frequency, the free electrons serve as the absorption mechanism, but at frequencies higher than the plasma frequency (typically the *UV* regime), the electrons cannot screen the electric field causing the absorption and reflection to decrease making the metal transparent. Metals typically contain a high absorption coefficient causing a small absorption depth referred to as the “skin depth”.

Unlike metals, insulators and semiconductors require both electronic and ionic contributions for absorption. Electronic conduction does not take place in insulators and semiconductors due to these materials containing few free carriers in the conduction band which are required for conduction. Therefore, under laser irradiation electrons must be promoted to the conduction band creating electron-hole pairs. The energy required for an electron in the highest valence state to be excited to the lowest level in the conduction band is called the bulk bandgap energy, E_g . Photons from incident laser light must have an energy greater than the material band gap for the photons to be absorbed by electrons, referred to as single-photon interband transitions. At photon energies less than the band gap, intraband electron transitions dictate the optical properties as well as the excitations of the phonons in the lattice. Impurities and defects in the material can also influence the optical properties by improving the coupling of insulators with laser radiation. Under ultrashort laser radiation, the dynamics between incident light and the material are different in which several stages of excitation and relaxation occur. These four stages are carrier

excitation, thermalization, carrier removal, and thermal and structural effects shown in Figure 2.1 along with their corresponding timescales.

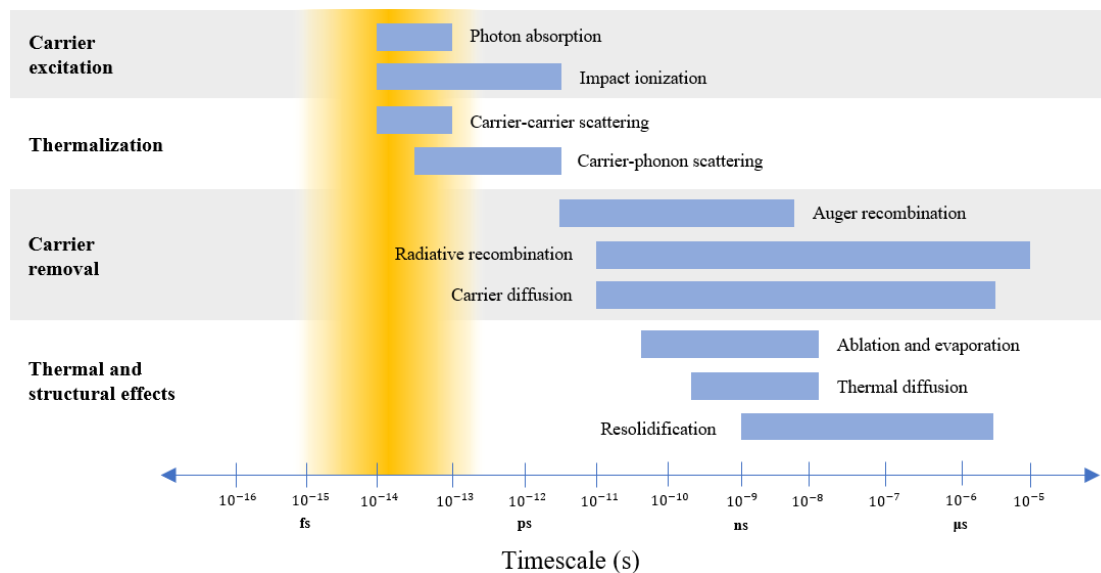


Figure 2.1 Timescales of processes in ultrashort laser irradiation [15].

Carrier excitations cover the excitation of electrons and holes in solids from incident light. Interband single photon absorption is the process of electron excitation and thus hole formation due to a single photon being absorbed that has an energy higher than the smallest direct bandgap (linear). Multiphoton absorption occurs when the bandgap is greater than the photon energy or if states are already filled in the conduction band. This process requires multiple photons to be absorbed and becomes more common at high laser intensities (nonlinear). After carriers have been excited to the conduction band, they are also able to absorb photons to move to even higher energy states. This is the dominant process that occurs in metals, since all charge carriers are found in the conduction band. Figure 2.2 shows the photon absorption process for single and multiphoton absorption.

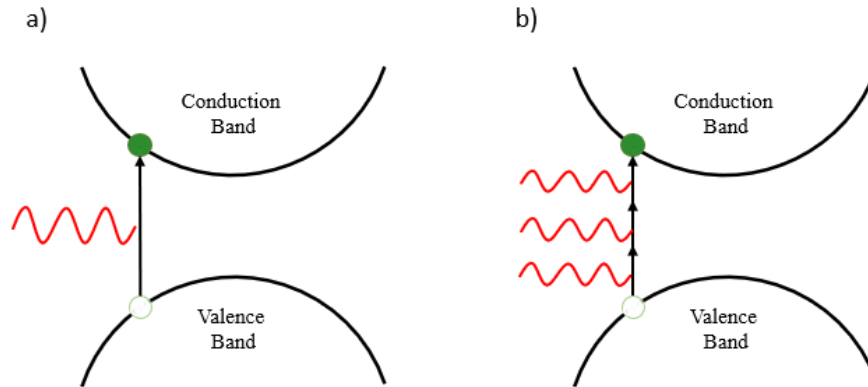


Figure 2.2 Single-photon absorption (a) and multiphoton absorption (b).

Absorption is more complicated in transparent materials in which laser induced breakdown is needed for excitation to take place. In this process, nonlinear processes like avalanche ionization and multiphoton ionization cause this optical breakdown. In a transparent material, laser light is not absorbed at low intensities because the bandgap or ionization potential is greater than the photon energy. But in reality, transparent materials contain some free electrons due to impurities or ionization of shallow energy levels and can be considered seed electrons for avalanche ionization. When the seed electrons oscillate in the electric field of the laser, and if the kinetic energy is larger than the ionization potential and enough energy is transferred, an ionization event will occur resulting in two free electrons with low kinetic energies, referred to as an impact ionization. This process is illustrated in Figure 2.3. The consequent energy released from this process increases the total number of free carriers but not the total energy and through repeated impact ionization events, the free electron density can grow exponentially, referred to as avalanche ionization. Once a critical electron density is achieved, optical breakdown has taken place in the transparent material and absorption is enabled where the critical density depends on the wavelength of laser used [15]. Impact ionization does not require photons to occur and thus can take place after a laser pulse has been deposited to the material. This process can have a major impact on plasma generation and optical breakdown in transparent materials. An illustration of the impact ionization process is shown in Figure 2.3. The absorption processes that occur in metals are free carrier absorption and impact ionization which

generate an electron plasma. At longer pulse widths, avalanche ionization is the primary mechanism for optical breakdown as multiphoton ionization is considered negligible.

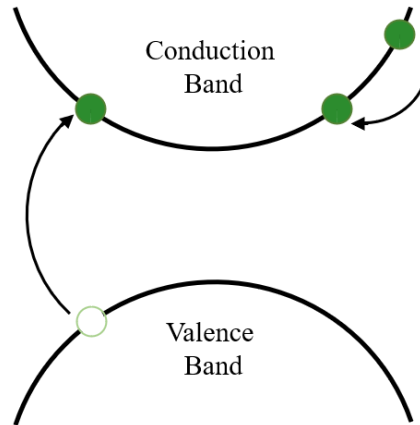


Figure 2.3 Schematic drawing showing the impact ionization process.

Carrier-carrier scattering is the process of energy and momenta of carriers changing due to collisions between two carriers by electrostatic Coulomb forces. When a monochromatic laser interacts with a semiconductor, the only electrons that are promoted to the conduction band are those that require the same energy to be promoted as the incident laser pulse, and thus free electrons and holes are only created at specific points in the band structure. Through carrier-carrier scattering, electrons and holes are dispersed through the conduction and valence bands, approaching the Fermi-Dirac distribution. The process of carrier-phonon scattering involves free carriers gaining or losing energy and momentum by absorption or emission of a phonon or lattice vibration. In semiconductors, carrier-phonon scattering can occur in either the conduction band minimum or valence band maximum known as intravalley scattering, or scattering can occur across the boundaries known as intervalley scattering.

In metals however, there is no bandgap and these become the same process. The physical mechanisms responsible for carrier-phonon scattering are called the deformation potential and polar scattering potential. Deformation potential is the most common in which the phonons that perturb the lattice exert a force on the carriers. Polar scattering, on the

other hand, occurs in polar materials with local dipole moments between groups of atoms where phonons perturb these dipole moments and exerts a force on free carriers through an electric field. Overall, the rate of scattering is linear for the most part, depending on the number of carriers and phonons up to a certain limit. A schematic diagram of carrier-carrier and carrier-phonon scattering is shown in Figure 2.4.

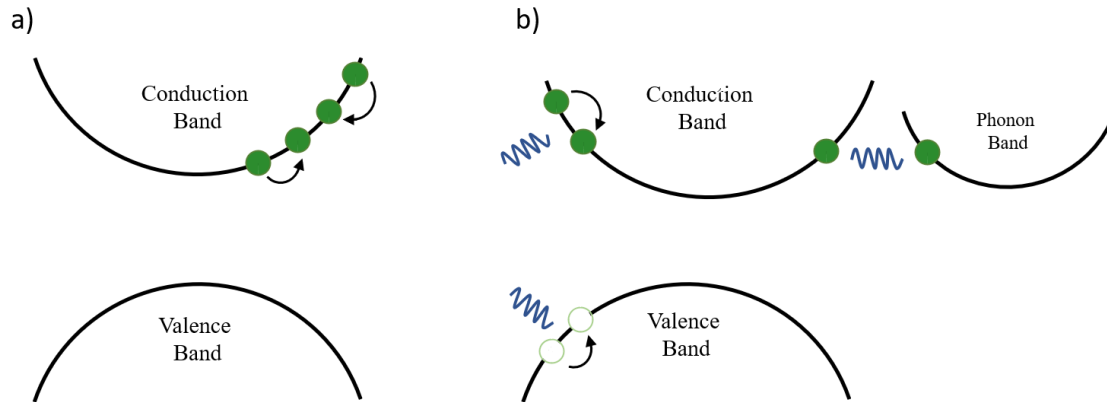


Figure 2.4 Carrier-carrier scattering (a) and carrier-phonon scattering showing intervalley and intravalley scattering (b).

Once carrier-lattice thermalization has occurred, the free carriers and lattice are at the same temperature. For a metal, the state is the same as if one were to heat the metal slowly to the same temperature. A Fermi-Dirac distribution is created around the Fermi level in metals, but for semiconductors, the electrons and holes form a Fermi-Dirac distributions over multiple Fermi levels. In this case, the carriers and lattice are at the same temperature, but thermal equilibrium does not exist due to an excess of free carriers remaining. These carriers can be removed by recombination of electrons and holes or diffusion of carriers from the photoexcited area. Recombination can still be a prominent mechanism in metals because carrier recombination can occur faster than thermalization with the lattice. During recombination, excess energy must be removed.

The most common mechanisms for energy removal are photon emission, carrier generation and defects or surface states. Photon emission can be referred to as a radiative recombination while the latter are considered non-radiative processes. Radiative

recombination can be thought of as the opposite of optical excitation processes, where carriers recombine and release energy through a photon. In this case, the density and total energy of free carriers decreases. In the case of non-radiative recombination, Auger recombination is a process where an electron and hole recombine, with the excess energy either exciting an electron to a higher energy state in the conduction band or a hole to a lower energy state in the valence band. In Auger recombination, the carrier density decreases but the energy of the system stays the same. Under defect- and surface-mediated recombination, recombination releases energy to a defect or surface state. This process results in a decrease of free carrier density and total system energy. Another form of energy removal is carrier diffusion. In this process the number of free carriers does not change, but instead the free carriers are removed from the area of excitation by diffusing through the material from a region of higher carrier density to lower carrier density [16]. These three carrier recombination processes are illustrated in Figure 2.5.

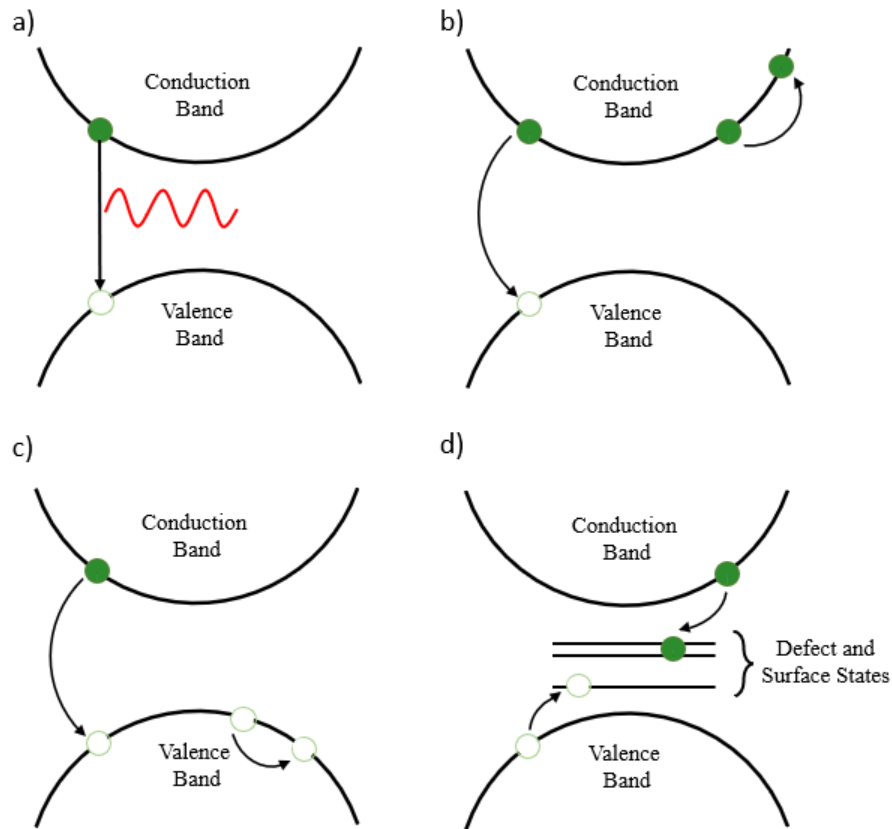


Figure 2.5 Carrier recombination mechanisms. (a) radiative recombination (b) Auger recombination (with electron) (c) Auger recombination (with hole) (d) defect and surface recombination

Laser ablation is a process that exploits the absorption of photons in a material to remove matter under intense laser irradiation. A threshold fluence must be met in order for ablation to occur. The value of the threshold fluence depends on many factors including the absorption mechanism itself, material properties, microstructure, surface roughness, number of defects, and on laser parameters including the wavelength, pulse width, and pulse shape. The threshold fluence, F_{th} (J/cm^2), is defined as the fluence at which there is a 50% probability that material breakdown will occur. Threshold values depend on the type of material and are usually 1 to 10 J/cm^2 for metals, 0.5 to 2 J/cm^2 for inorganic insulators and 0.1 to 1 J/cm^2 for organic materials [14]. For the case of optically transparent materials, at longer pulse widths ($\gtrsim 10$ ps), avalanche ionization is the main breakdown mechanism and a large statistical deviation of breakdown/ablation threshold can occur.

This causes some pulses above the threshold to not breakdown the material and some pulses below the threshold to breakdown the material. However, under ultrashort pulses it has been found that there is a strict fluence threshold with very little statistical variation. This is due to the different physical mechanisms in place. For relatively longer pulse widths, the variation in fluence threshold is caused by the statistical variation in seed electron density that can be significantly different at different points in the material. For ultrashort pulses the physical mechanism is multiphoton ionization which doesn't depend on seed electrons, causing the fluence threshold to be much more predictable and is another advantage of ultrashort pulsed laser ablation.

Threshold fluence values can also change based on the number of pulses used for ablation, known as the incubation effect, where a higher number of pulses causes the threshold fluence to decrease. This relation can be characterized by

$$F_{th}(N) = F_{th}(1)N^{\zeta-1} \quad (2.8)$$

where $F_{th}(1)$ is the single pulse fluence threshold, N is the number of pulses, $F_{th}(N)$ is the multiple pulse fluence threshold, and ζ is the incubation coefficient. ζ can be determined in an experiment as the slope of the plot of $\log[NF_{th}(N)]$ and $\log N$. The presence of defects and impurities can also have a large influence on incubation.

There are different laser ablation mechanisms which depend on processing parameters including the wavelength, fluence, and pulse width. At lower fluences, photothermal mechanisms are responsible for ablation where evaporation and sublimation occur. At higher laser fluences nucleation of vapour bubbles occurs locally in the material causing boiling. At even higher fluences, when the laser heating is too quick for the material to reach its critical temperature then explosive boiling can occur due to homogeneous nucleation and expansion of vapour. If the excitation time from laser irradiation is shorter than the thermalization time of the material, then non-thermal photochemical ablation can take place. Under high laser intensities, a plasma plume is produced as a by-product of material removal due to the laser electric field causing optical breakdown in the material. Under ultrashort pulses, the particles leaving the material create an equilibrium velocity distribution just above the material surface called the Knudsen layer. Above this layer the

plasma plume creates a shockwave front due to rapid compression of ambient gas from plume expansion [14].

The extent of energy transfer, and thus heating, is dependent on the pulse width and energy coupling coefficient of the material. Energy can also diffuse outside the laser focus spot due to the thermal gradient in the material. In relatively long pulses, the electron-ion coupling can be strong, and electrons and ions may be in thermal equilibrium or quasi-equilibrium where significant heat diffusion can be present with the peak temperature of the material being relatively low. As the pulse width decreases, the laser field becomes stronger causing electrons and ions to be driven out of equilibrium in which electrons may reach temperatures of thousands of kelvins while the ions remain cold. Energy transfer then occurs until a thermal equilibrium is eventually achieved. In this case, temperatures sufficient to perform ablation can be achieved while thermal conduction can be relatively insignificant. Upon laser irradiation, incident energy can only penetrate to a depth defined by the penetration depth $l_p = \frac{1}{\alpha}$. The other depth parameter is the diffusion length $l_d = \sqrt{D\tau_p}$ where D is the heat diffusion coefficient and τ_p is the pulse width. Under relatively longer pulses, $l_d > l_p$, where the material heating is dependent on the diffusion length and thus $F_{th} \propto \sqrt{\tau_p}$. However, when the pulse width reaches a critical value to where $l_d < l_p$, then the material heating is dependent on the penetration depth and the fluence threshold becomes independent of the pulse width.

Under longer pulses, when the diffusion length is larger than the penetration depth, expulsion of the melt material causes ablation due to recoil of the vapour pressure. This process is very unstable and generally undesirable for cutting and drilling applications since the melted material can resolidify after ablation and result in imperfect craters. Under ultrashort pulses, heat diffusion is insignificant with penetration depth dictating the energy deposition. The material is heated directly to a vapour with high kinetic energy, bypassing the liquid phase, resulting in a much cleaner ablation surface due to the small amount of material being melted and the large amount of heated material removed by vaporization causing fast cooling [15].

Under ns-pulsed laser ablation, material removal takes place by way of nanoparticles due to photothermal processes. The energy deposition occurs over a relatively long amount

of time, therefore the energy interacts with both the electrons and phonons of the material. At low laser fluences, the laser energy is absorbed within the penetration depth where thermal evaporation occurs. At fluences just above the ablation threshold, ionization of the plasma plume takes place due to heating of the material but at fluences higher than the gas ionization threshold, ionization occurs due to optical breakdown. At very high laser fluences where the surface temperature reaches the critical temperature, the material undergoes phase explosion where matter transforms from a superheated liquid to a vapour liquid mixture resulting in a plasma of high temperature and pressure ejecting the droplets at sonic velocity. The material that is ejected then resolidifies creating material deposits around the crater which can be undesirable for machining purposes.

Pulse widths of less than 10 ps define the upper limit of ultrashort pulses. Under ultrashort laser ablation material removal is usually the result of a mechanism called critical point phase separation (CPPS). With this mechanism, a significant change of density in the material does not occur until the critical temperature of the material has been reached. At this point the density starts to decrease and the material that has entered the unstable zone will be ablated while the rest will condense onto the material surface. On the surface of the material, the material transforms from the solid phase directly to the vapour or plasma phase while material that is further beneath the surface reaches the liquid phase. The energy coupling of ultrashort ablation follows the two-temperature model [14].

Femtosecond laser pulses are defined as laser pulses shorter than 1 ps. Recent advances have enabled extremely high intensity laser pulses that require relatively small overall energy due to the nature of the short pulse. For example, a 100 fs (10^{-13} s) pulse with an energy of 1 mJ, and beam diameter of 20 μm will produce a peak intensity of 3×10^{15} W/cm². A 10 ns pulse would require about 100 J to produce the same peak intensity. An ultrashort laser pulse also eliminates the fluid dynamics in the ablation process with ablation occurring directly from the solid to vapour state while also causing minimal heat diffusion and thus a small heat affected zone (HAZ). The HAZ is the area of material whose properties and microstructure are altered due to heat from the incident laser light. Typically, it is desirable to minimize the HAZ to avoid thermally induced cracks and droplet formation that can compromise the performance of the material. Figure 2.6 shows a comparison of HAZs for long pulse and femtosecond pulse lasers.

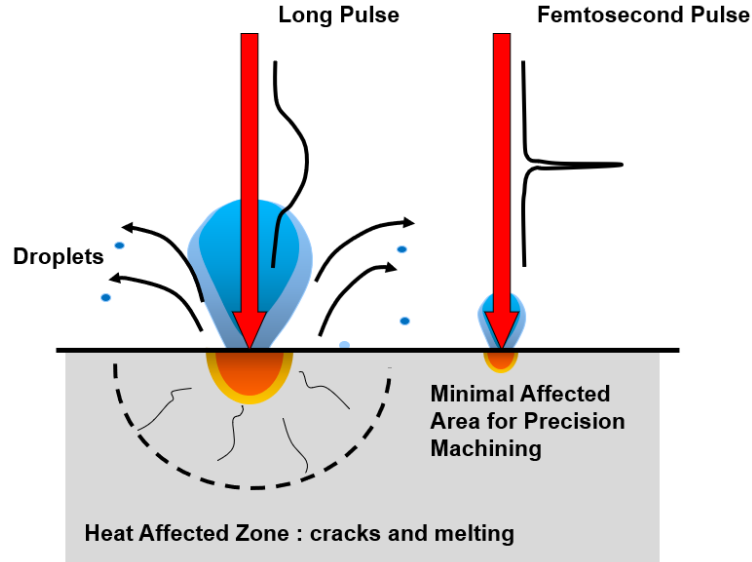


Figure 2.6 A comparison of HAZs for long pulse and femtosecond pulse lasers.

For fs laser irradiation, the energy exchange between the electrons and lattice depends on the electron-phonon coupling parameter inherent to the material being irradiated. The larger the electron-phonon coupling indicates a higher rate of heat transfer from the electrons to the lattice. The unique ablation characteristics of fs laser irradiation is due to the deposition time of energy being much shorter than the mechanical relaxation time of the material $\tau_m = \frac{l_p + l_e}{C_m}$, where l_e is the electron energy transfer depth and C_m is the speed of rarefaction wave in the material. If the pulse width is shorter than the mechanical relaxation time, the time it takes to initiate a collective motion of atoms within the absorbed volume, then ultrafast heating takes place resulting in direct solid to vapour material phase change and no heat diffusion outside the beam spot diameter [14].

It has been found that two ablation regimes exist for ultrashort laser irradiation. At lower laser fluences, the ablation depth per pulse, L , is determined from

$$L = \alpha^{-1} \ln\left(\frac{F}{F_{th}}\right) \quad (2.9)$$

where F is the laser fluence and F_{th} is the ablation threshold fluence. At higher fluences a second relation is given for ablation depth in

$$L = l_{p2} \ln \left(\frac{F}{F_{th2}} \right) \quad (2.10)$$

where l_{p2} is the higher energy heat diffusion depth and F_{th2} is the higher ablation threshold fluence. Another effect of high laser fluence in ultrashort laser ablation is the formation of plasma. It has been shown that plasma can influence ablation quality at lower and moderate fluences producing a shielding effect in which the plasma absorbs some laser light, but at high laser fluences the plasma may become transparent to the light.

Several different ablation mechanisms exist for ultrashort laser irradiation, being spallation, melting, phase explosion and critical point phase separation. By first using simulations, it was found that laser irradiation can cause expansion and change internal pressure of a solid material near the threshold fluence. The laser irradiation induces a tensile stress in the material that is larger than the material tensile strength limit resulting in defects that lead to fractures and ultimately ejection of layers of material. This process is known as spallation [17].

At even higher fluences, higher temperatures and pressures within the material cause complex thermodynamic processes leading to phase explosion. Phase explosion occurs when the material approaches the thermodynamic critical point temperature causing large homogeneous nucleation to take place. The liquid can reach a temperature above the boiling temperature to a superheated state. At the highest fluence rates a process called critical point phase separation occurs. When the critical point temperature of the material is exceeded, expansion of material leads to a pressure reduction to a thermodynamically unstable region resulting in material decomposition [18].

2.3 Overview of Graphite, Graphene and Graphene Derivatives

Graphene is a two-dimensional sp^2 hybridized allotrope of carbon consisting of a single atomic layer in a hexagonal structure. It can be rolled into tubes to create carbon nanotubes or into a sphere to create buckminsterfullerene. Its bulk counterpart, highly oriented pyrolytic graphite (HOPG), consists of many graphene layers stacked upon each other bonded by weak van der Waals forces and is generally defined as being more than 10

graphene layers. Bilayer graphene (BLG) consists of two graphene layers, trilayer graphene (TLG) consists of three graphene layers, and multilayer graphene (MLG) consists of four to ten layers. Graphite is considered to be an anisotropic material, meaning its properties parallel to the graphene sheets, the ab-plane, are different than those in the perpendicular direction, the c-axis. Graphite is shown to have a high inter-layer cohesion due to covalent bonding but low intra-layer cohesion due to the weak van der Waals bonding.

Although being investigated theoretically for many years, graphene was first successfully isolated through mechanical exfoliation of HOPG using sticky tape in 2004 by researchers A. Geim and K. Novosolev [3]. It was reported to have exceptional properties much different than bulk graphite including the highest known room temperature electrical conductivity, a very high Young's modulus of 1 TPa [19], very high thermal conductivity of $\sim 5000 \text{ W/m}\cdot\text{K}$ [20], a high strength-to-weight ratio and optical transmittance of $\sim 97.7\%$. Graphene has also been found to have unique electronic properties such as possessing Dirac fermions, exhibiting the quantum hall effect, having massless low energy excitations, and exhibiting a high Seebeck coefficient making it easier to convert electrical current to thermal energy. Since its physical discovery, graphene has been a heavily researched material due to its outstanding material properties boasting potential for a wide variety of applications including photovoltaic cells, transparent and flexible electronics, power storage, and sensors. Its synthesis, however, has proven to be difficult and costly, and extensive research is still being conducted to solve this issue.

2.3.1 Graphene Oxide

One derivative of graphite that poses an inexpensive route to producing graphene is through graphite oxide which is a compound of carbon, oxygen and hydrogen, and similar to graphite, it can be reduced through exfoliation to its single layer counterpart to produce graphene oxide (GO) [21]. Graphene oxide is a hybridized sp^2 2D carbon structure with carboxyl, hydroxyl, and epoxy functional groups attached to both sides, and although being related to graphene, the presence of oxygen functional groups cause its properties to behave much differently such as it being electrically insulating and thermally unstable. A diagram of the GO lattice structure is provided in Figure 2.7. One advantage of graphene oxide is

that it is hydrophilic and can be easily dispersed in an aqueous solution due to water molecules being able to intercalate between layers. This allows for the formulation of graphene oxide inks that can be printed on to a variety of substrates for electronic device applications [22].

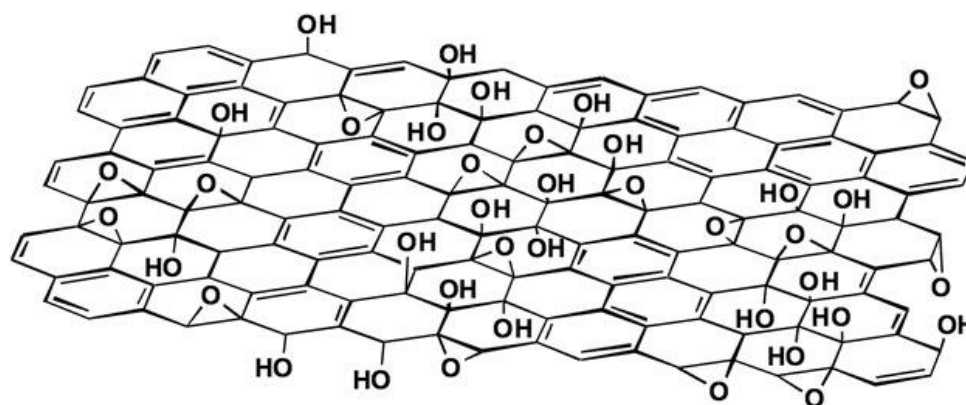


Figure 2.7 Molecular structure of graphene oxide [23].

Although GO has properties that can be less favourable than graphene, it can be used to obtain almost graphene-like behaviour through reduction to produce rGO by removing most of the residual oxygen and structural defects thereby restoring the sp^2 structure found in graphene. This can be done using chemical [24], thermal [25], or photo-thermal techniques [26]. Chemical reduction often uses inorganic agents such as phenyl hydrazine hydrate or hydroxylamine but this has a disadvantage in terms of environmental impact due to its highly toxic nature while achieving less reduction compared to thermal methods. Thermal reduction on the other hand uses an inert or reducing atmosphere at temperatures between 300°C to 2000°C to break the oxygen functional group bonds and produce rGO. This can also be accomplished using a laser to achieve precise and highly controllable reduction. Reduction of GO to rGO has been proven to increase overall surface area, mechanical strength, Young's modulus, and electrical conductivity.

2.3.2 Thermal Properties of Graphene

It is understood that since graphene has a relatively low carrier density in its undoped state, the electronic contribution in heat transfer is negligible and it is assumed that thermal conductivity and heat capacity are dominated by phonons, with diffusive conduction at high temperatures and ballistic conduction at low temperatures [27] [28]. With graphite being an anisotropic material, its thermal properties are different along different directions, such as its room temperature thermal conductivity being $39 \text{ W/m}\cdot\text{K}$ in the ab-plane and $2.2 \text{ W/m}\cdot\text{K}$ [29] in the c-axis, however it can also be shown that thermal properties are different based on the number of layers. In general, thermal conductivity for thin film semiconductors decreases with decreasing thickness, but in graphene the opposite effect is observed. Based on theoretical calculations by Alofi *et al.* [30] Figure 2.8 shows the cross-plane, k_{AB} , and in-plane, k_C , thermal conductivity for different layers of graphene as a function of temperature. It is seen that graphene has a much higher k_{AB} value at low temperatures before reaching a peak at $\sim 200 \text{ K}$ before decreasing. k_C shows a higher dependency on layer thickness compared to k_{AB} , but due to weak van der Waals forces the thermal conductivity is much lower. It can be seen that k_C is much higher for bulk graphite compared to layered graphene, with the thermal conductivity being almost three orders of magnitude larger at 100 K .

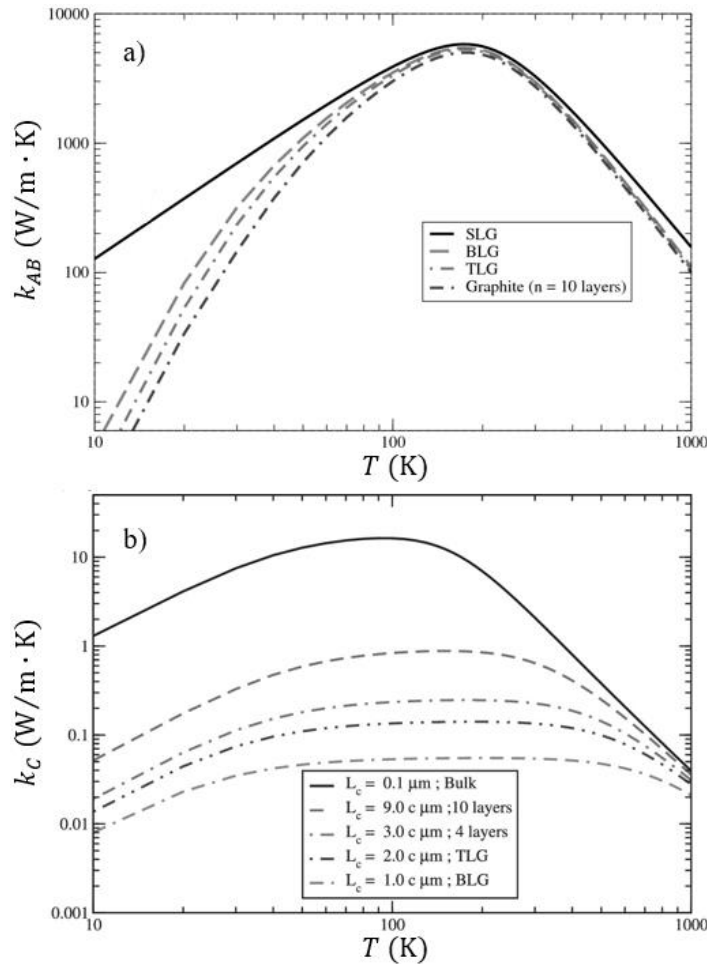


Figure 2.8 (a) In-plane thermal conductivity for multilayer graphene sheets (b) c-axis thermal conductivity for multilayer graphene sheets (Reprinted with permission from Appl. Phys. Lett. 104, 031903 (2014), Copyright 2014 AIP).

Furthermore, from the calculations by Alofi *et al.* at room temperature k_{AB} shows a large decrease from $\sim 3275 \text{ W/m}\cdot\text{K}$ for SLG to $\sim 2975 \text{ W/m}\cdot\text{K}$ for BLG and decreases with smaller increments before reaching $\sim 2740 \text{ W/m}\cdot\text{K}$ for 10 layer graphene. On the other hand, k_C shows a linear increase in thermal conductivity with layer thickness from $\sim 0.05 \text{ W/m}\cdot\text{K}$ for 2 layers to $\sim 0.65 \text{ W/m}\cdot\text{K}$ for 10-layer graphene. Although these theoretical thermal conductivity values agree well with experiment, values in experiments for suspended graphene show a large range from 2000 – 4000 K. The upper limit is achieved when graphene is isotopically purified with large grain sizes and the lower limit with isotopically mixed and small grain sizes, however any disorder due to impurities

lowers the thermal conductivity from this range [31]. Graphene on a substrate also presents much lower thermal conductivity due to the sensitivity of the phonon propagation to surface or edge perturbations. It has been reported that graphene deposited on SiO_2 has a thermal conductivity of $600 \text{ W/m} \cdot \text{K}$ [32] and graphene encased in SiO_2 has a thermal conductivity of $160 \text{ W/m} \cdot \text{K}$ [33] which is still much higher than that of copper. The reason for this reduction when layered on a substrate is thought to be caused by phonons diffusing across the graphene-substrate interface and strong scattering of flexural modes with the substrate. In terms of electronic thermal conductivity, it has been shown that graphene does not follow Fermi liquid theory corresponding to most metals and instead expresses the properties of a Dirac fluid in which the Wiedemann-Franz law is not valid in determining electronic thermal conductivity [34]. However, Kim *et al.* have shown through first-principles that the Wiedemann-Franz law is broadly satisfied in doped graphene with the largest deviations being 20 – 50% at room temperature [35].

Along with the thermal conductivity, the specific heat also shows a dependency on the number of graphene layers. Figure 2.9 shows the specific heat for different number of layers for graphene as a function of temperature. It is shown that SLG possesses much higher specific heat at low temperatures but converges close to the same value at room temperature.

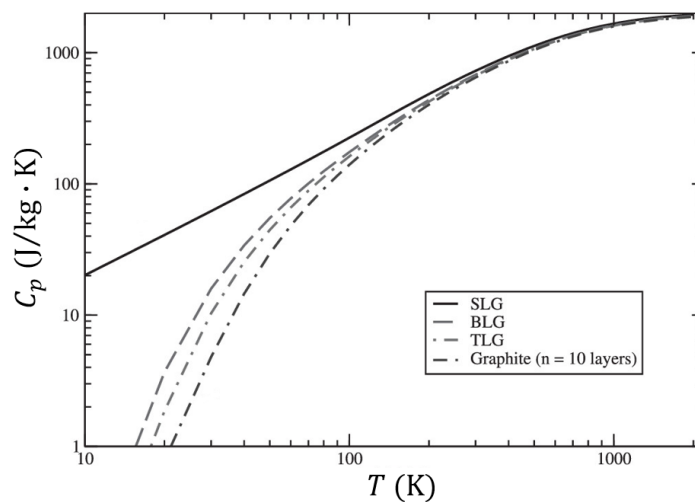


Figure 2.9 Specific heat capacity for graphene layer number with temperature (Reprinted with permission from Appl. Phys. Lett. 104, 031903 (2014), Copyright 2014 AIP).

Figure 2.9 also shows that near the Debye temperature ($\theta = 2100$ K), which is the temperature associated with the highest phonon vibration mode in a solid, the heat capacity becomes nearly constant at 2100 J/kg·K represented by the Dulong-Petit limit ($C_p = 3N_A k_B$) where N_A is Avagadro's number and k_B is the Boltzmann constant. At room temperature the specific heat is approximately one-third of this theoretical limit at 700 J/kg·K. Similar to thermal conductivity, it is believed that the heat capacity will be reduced when in contact with a substrate [30].

2.3.3 Optical Properties of Graphene

Along with graphene's exceptional mechanical, electrical and thermal properties, it also has unique optical properties. A single layer of graphene is found to be optically transparent in a vacuum absorbing only $\sim 2.3\%$ of incident light from visible to infrared with transparency decreasing linearly with each added layer [36]. This unique property raises an opportunity for devices such as flexible and transparent electronics but can also lead to problems with laser micromachining where the substrate can become damaged due to most of the light passing through. Another unique optical property is that absorption becomes saturated when above a certain threshold [37]. This is referred to as saturable absorption with the threshold fluence value leading to saturable absorption being called the saturation fluence. This effect becomes apparent during laser micromachining where the ablation depth per pulse reaches a maximum value even when the pulse energy is increased and puts a limit on how fast laser micromachining operations can be performed. This unique property, however, gives graphene the ability to be used in applications such as ultrafast photonics where the optical response can be tuned electrically.

Based on the complex refractive index values determined by Song *et al.* and Schmiedova *et al.* [38][39], the reflectivity spectrum and optical penetration depth were determined for HOPG and rGO using Equations 2.5 and 2.7. The computational results from these equations are shown in Figures 2.10 and 2.11, respectively.

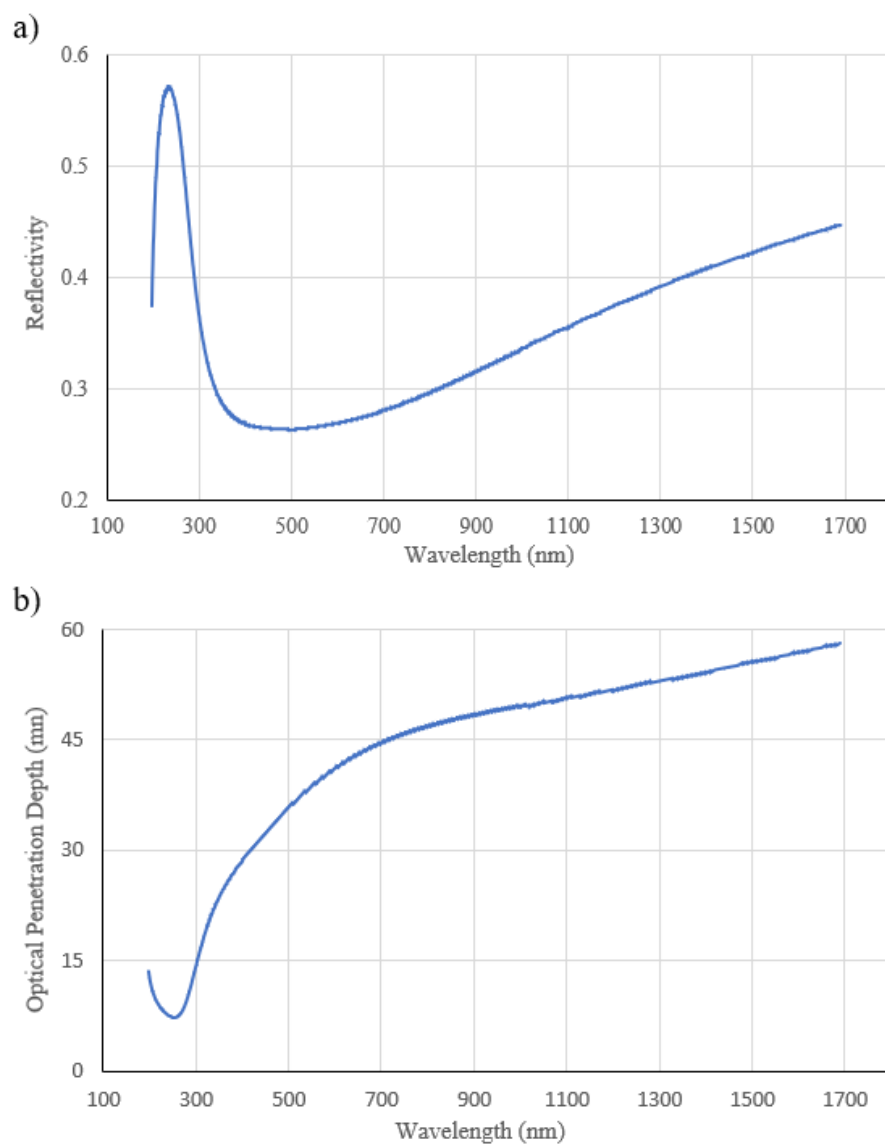


Figure 2.10 Reflectivity spectrum of HOPG (a) and optical penetration depth of HOPG (b).

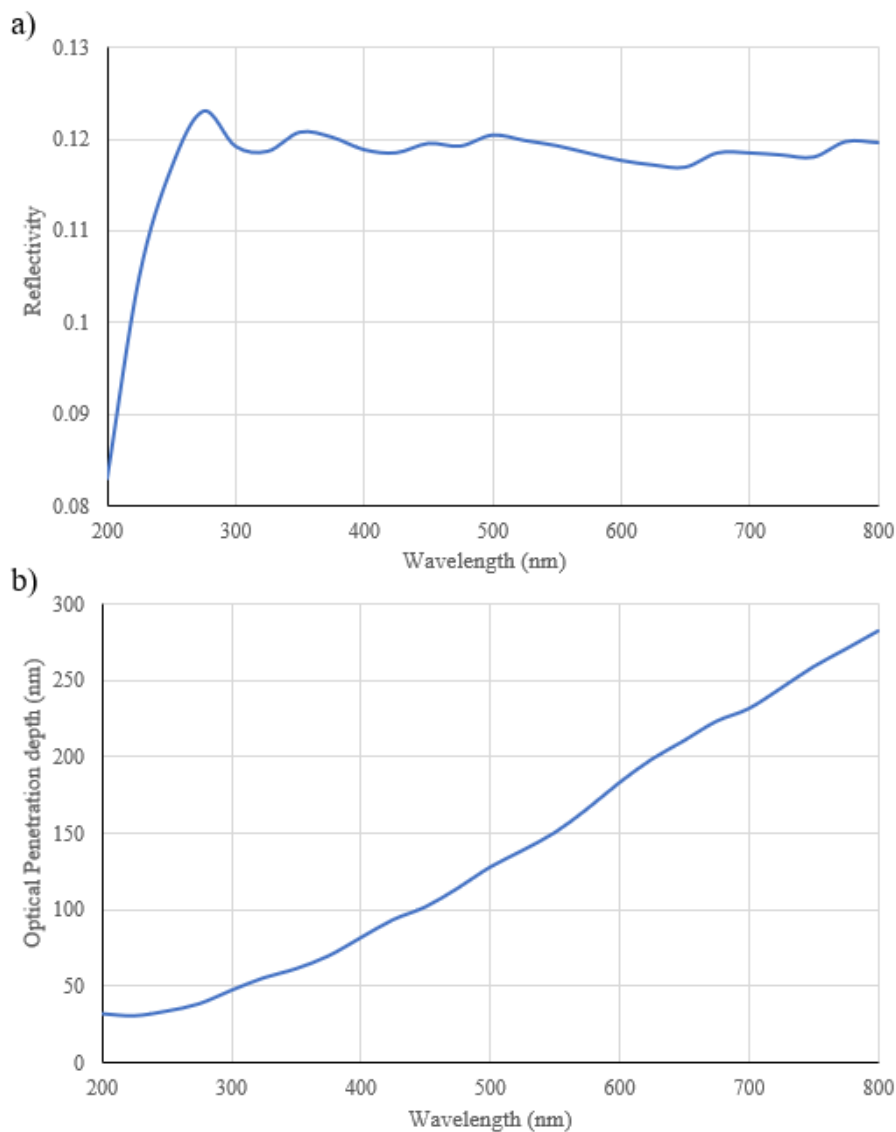


Figure 2.11 Reflectivity spectrum of printed rGO and (a) and optical penetration depth of printed rGO (b).

From Figure 2.10a, it is seen that the reflectivity reaches a maximum of 0.57 at 230 nm wavelength and a minimum of 0.26 at 500 nm wavelength. The reflectivity value of 0.26 indicates maximum absorption and thus efficient energy coupling at this wavelength. From Figure 2.10b the optical penetration depth reaches a minimum of 7 nm at 240 nm wavelength and a maximum of 58 nm at 1690 nm wavelength indicating a large HAZ. For printed rGO in Figure 2.11a, the reflectivity shows much lower values than HOPG with

a minimum as low as 0.083 at 200 nm wavelength and maximum of 0.124 at 280 nm wavelength, indicating higher absorption at all wavelengths for printed rGO. From Figure 2.11b the optical penetration depth is also much lower than HOPG with a minimum of 32.5 nm at 200 nm wavelength and a maximum of 283 nm at 800 nm wavelength indicating a smaller HAZ for printed rGO at all wavelengths.

2.4 Graphene Synthesis

One of the biggest challenges in implementing graphene into real life applications involves material synthesis. There are four common methods for synthesizing graphene which are chemical vapour deposition (CVD), micromechanical exfoliation, exfoliation of graphite in solvents, and other methods. CVD is the most popular due to its capability of producing large area graphene at a relatively low cost. The process works by pumping hydrocarbon precursor gasses into a heated reactor where they decompose into carbon radicals and bond to a metallic substrate. The substrate then acts as a catalyst to lower the energy barrier of the reaction. The thickness of the graphene layer formed on the substrate can be controlled through the amount of hydrocarbon gas fed into the reactor and by the total reaction time. Common metal catalysts used during CVD are copper and nickel due to nickel's high carbon solubility at high temperatures where carbon diffuses from nickel as it is cooled, and copper because of its ability to form a single layer of graphene. After CVD is performed the synthesized graphene can be transferred to another substrate by coating the graphene layer with a thin layer of polymethyl methacrylate (PMMA), chemically etching the metal catalyst, moving the PMMA/graphene onto the desired substrate and finally removing the PMMA with acetone [40].

Micromechanical cleavage is another method to synthesize pristine graphene and was the method used to first isolate graphene [3]. This method works using scotch tape to 'peel' a layer of graphite from HOPG and is commonly used to study graphene transport physics and other properties. One downside of this method is its inability to scale to larger areas with graphene production typically being on the order of tens to hundreds of microns.

A third method to synthesize graphene is by the exfoliation of graphite in various solvents. This is usually done by mixing powdered graphite with organic solvents like

dimethylformamide or N-methylpyrrolidone and applying a high intensity ultrasound to produce graphene dispersions. The dispersion can then produce useful graphene flakes in applications by spray coating, vacuum filtration or dop casting. Although this method is able to produce pristine graphene, the overall yield is relatively low.

GO is commonly prepared by the Hummer's method, in which graphite powder is mixed and stirred into an acid solution. Potassium permanganate is then added to the solution where it is stirred for several hours. Additional reactants are then added before the mixture is centrifuged to isolate the GO. The final solution is processed and dried in an oven to produce graphene oxide powder [41].

2.5 Graphite Ablation Experiments

Although graphene and graphite ultrashort laser ablation has not been simulated through FEA, many physical experiments have been performed attempting to understand their properties and ablation characteristics. In 1984, Venkatesan *et al.* [42] performed laser irradiation experiments on HOPG with a 30 ns, 695 nm wavelength laser and by using Rutherford-backscattering spectrometry and a melting model found HOPG to have a fluence damage threshold of 0.6 J/cm^2 which causes melting, and a melting temperature of 4300 K. Their study also suggests that the damaged area recrystallizes after melting to form a polycrystalline graphite. Ultrafast melting characteristics of graphite were also studied by Dallas *et al.* [43] in 1994 using a 620 nm, 90 fs single pulse laser. The researchers found that at fluences $> 0.82 \text{ J/cm}^2$, the rapid annealing process takes place from re-solidified melt to form a nanocrystalline graphite at the surface.

Sokolowski *et al.* [44] studied the dynamics of fs laser ablation of graphite using both experiments and a theoretical model. The researchers discovered the existence of two different ablation regimes for graphite by using time resolved microscopy to measure the reflectivity of the irradiated surface after a 100 fs single laser pulse. Using an ablation model, they determined that the material removal was the result of hydrodynamic expansion from a highly pressurized fluid layer. Following the hydrodynamic expansion, it was found that μm -sized fragments are ablated from the surface suggesting that the formation and ejection of these fragments are responsible due to solidification of the liquid

graphite before transforming into gas. At fluences higher than 250 mJ/cm^2 , neither the interference pattern or fragments are observed suggesting that the graphite melt skips the liquid-gas coexistence regime and exceeds the critical point of the phase-diagram causing the material to be permanently removed from the surface without forming fragments.

Shirk *et al.* [45] later performed ultrashort laser ablation experiments on HOPG using an 825 nm wavelength Ti:Sapphire laser and used stylus profilometry, SEM, AFM and Raman spectroscopy to characterize ablation depth, fluence threshold, and provide crater images. It was found that the average ablation depth per pulse increases with laser fluence until reaching a saturation point shown in Figure 2.12. It was also found that the depth per pulse increases with decreasing pulse width. The fluence threshold for ablation was determined to be 0.25 J/cm^2 for a 120 fs pulse and suggests that reducing the pulse width dramatically reduces the ablation threshold based on other experimental work on graphite laser ablation. Using SEM and AFM images, the researchers found for many pulses (> 100) a significant amount of debris surrounding the ablated crater existed for pulse widths in the ps regime compared to fs. They also found that for high fluences ($\sim 10.6 \text{ J/cm}^2$) in the fs regime that the crater becomes cracked due to the highly energized plasma escaping the crater. Based on Raman spectra analysis it was found that a thinner layer of amorphous carbon exists after fs pulse ablation compared to ps pulses. Ultimately the researchers concluded that the optimum laser parameters for HOPG pulsed laser ablation when considering efficiency, accuracy and minimum thermal damage are 2 J/cm^2 fluence, 1 kHz repetition rate and 120 fs pulse width.

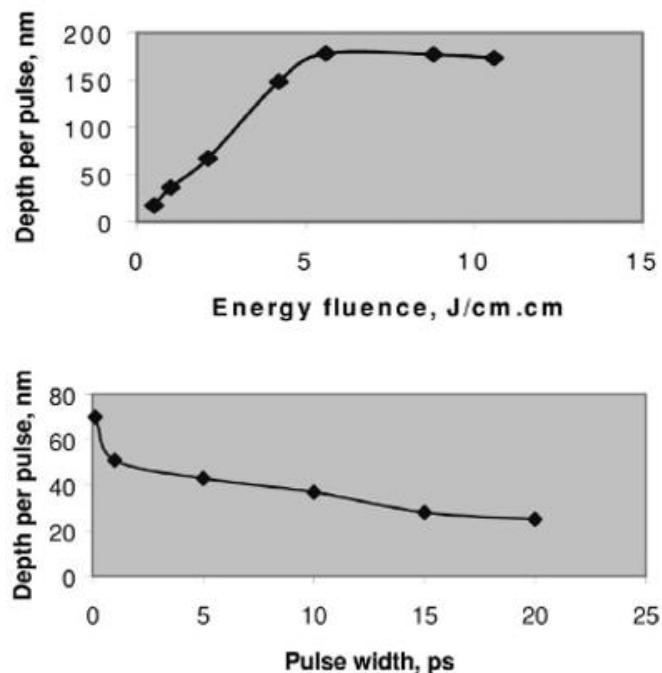


Figure 2.12 Single pulse ablation depth on HOPG as a function of energy fluence and pulse width (Reprinted with permission from [45], Copyright 2001 Elsevier).

Lenner *et al.* [46] performed single shot 120 fs laser pulses at 800 nm wavelength on HOPG to study nanoscopic Coulomb explosion of carbon ions in graphite. Using time of flight spectrometry, it was found that the nonthermal ablation of only a few graphite monolayers can occur at fluences just above the damage threshold due to the charge localization on the graphite surface [47]. Another experiment by Lenner *et al.* in 2009 studied the ablation characteristics of single shot femtosecond regime irradiation on HOPG using different characterization techniques to further study nanoscopic Coulomb explosion in graphite. Through surface analysis they found that the graphite nanoparticles generated from Coulomb explosion can be redeposited to the surface in a thin layer due to attractive van der Waals forces with the layer thickness dependent on laser fluence. Above the damage threshold, a reduction in ablated ions can occur due to the change in material optical properties causing reduced absorption.

Ionin *et al.* [48] used time-resolved optical reflection microscopy to determine threshold fluences for melting, spallation and fragmentation as well as the sound velocity under these respective mechanisms. The experiment used an 800 nm wavelength, 110 fs

pulse Ti:Sapphire laser on HOPG finding the melting threshold to be $\sim 0.15 \text{ J/cm}^2$, the spallation threshold to be $\sim 0.21 \text{ J/cm}^2$ and the fragmentation threshold to be $\sim 0.3 \text{ J/cm}^2$.

2.6 Graphene Phonon Properties

In terms of material classification for absorption properties, graphene can be considered a zero-bandgap semiconductor due to the conduction band and valence band meeting at a location in momentum space called the Dirac point. This unique electronic characteristic gives graphene many of its unique properties as well as unique electron-phonon scattering mechanisms that have been studied to understand the light matter interaction of graphene for laser processing and Raman spectroscopy.

Sun *et al.* [49] used ultrafast optical differential transmission spectroscopy to understand graphene's ultrafast relaxation dynamics. They determined that in multilayer epitaxial graphene, electron cooling is enabled by electron-acoustic phonon scattering on a timescale of 1 ps in highly doped layers and 4 – 11 ps in undoped layers.

Wang *et al.* [50] used ultrafast optical pump-probe spectroscopy to study the relaxation dynamics of optical phonons in few-layer and multilayer graphene synthesised by epitaxy on silicon carbide substrates and CVD on nickel substrates. They found that energy from hot carriers is lost to generate optical phonons in the first few hundred femtoseconds and that this represents the main bottleneck for cooling. They also learned that this optical phonon cooling is independent of the graphene synthesis method, number of layers and type of substrate.

Vallabhaneni *et al.* [51] confirmed through predictive simulations that phonon polarizations of SLG are in strong nonequilibrium which has significant implications to thermal conductivity measurements using Raman spectroscopy where the thermal conductivity can be underestimated by a factor of 1.35 to 2.6 at room temperature. These nonequilibrium phonon polarizations also require the temperature of each phonon mode to be considered separately rather than assuming the phonon modes to be in equilibrium in a typical TTM. This has been realized in the form of a multitemperature model to properly simulate the laser irradiation of SLG and is discussed further in Section 4.2.1. Figure 2.13

shows a diagram of the electron and phonon scattering distributions with different phonon branches.

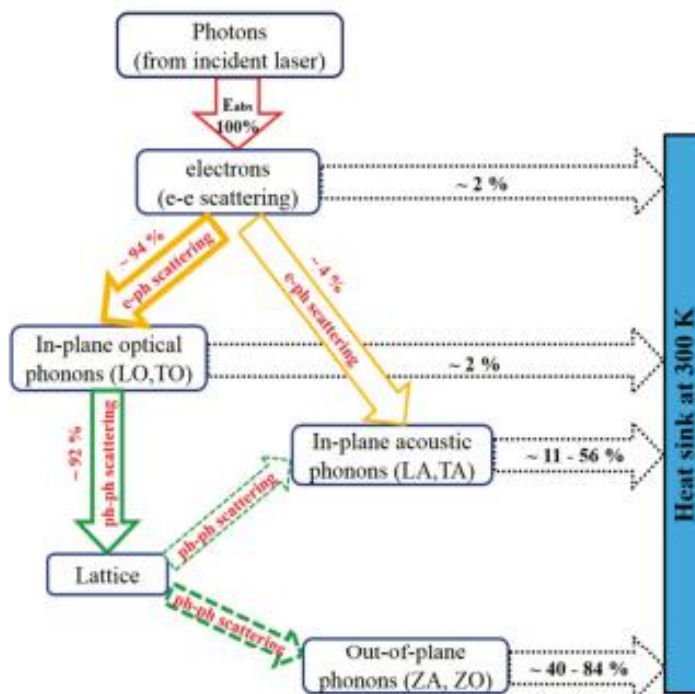


Figure 2.13 Calculated percentage of energy flow for carriers in laser irradiated graphene (Reprinted with permission from [51], Copyright 2016 American Physical Society).

2.7 Graphene Ablation Experiments

Many ultrafast laser irradiation experiments have been performed on graphene to understand its ablation characteristics and process the material for electronic applications. In 2011, Roberts *et al.* [52] performed ultrafast laser irradiation of SLG to establish the single shot damage threshold for clean ablation. They used CVD SLG grown on copper and transferred it to a glass substrate where a 790 nm wavelength Ti:sapphire laser was used to irradiate the graphene with a spot size of 20 – 30 μm and Raman spectroscopy was used to characterize the damage. They found the single shot energy fluence threshold to be 200 mJ/cm^2 at pulse widths of 100 – 1600 fs which is very close to the theoretical value of 250 mJ/cm^2 determined in previous work. However, at 50 fs the intensity threshold

(2.7×10^{12} W/cm²) is much higher compared to continuous wave (CW) (1×10^6 W/cm²). They also found that defect formation of nano-crystallites occurs at single shot exposures below the damage threshold. Figure 2.14 shows the fluence and intensity thresholds of SLG with respect to pulse duration.

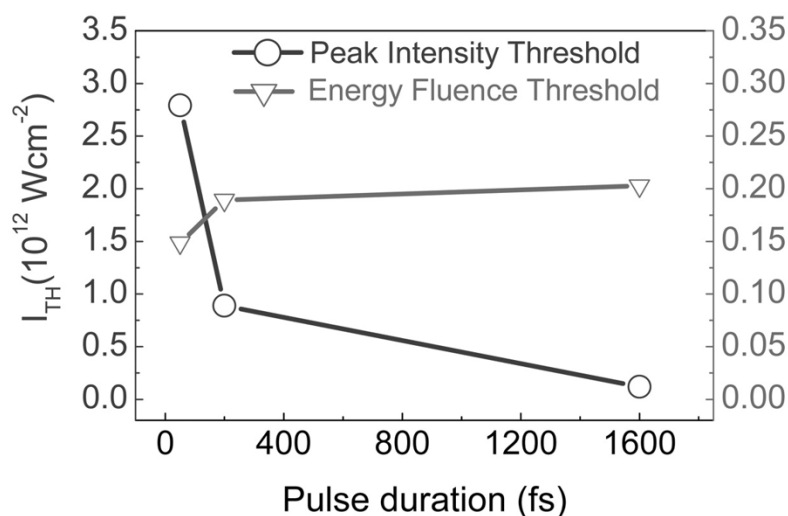


Figure 2.14 Peak intensity and fluence threshold on SLG as a function of pulse duration (Reprinted with permission from [52], Copyright 2018 AIP).

Sahin *et al.* [53] used a 343 nm wavelength, 550 fs pulse width Bessel beam to produce nm scale patterns in SLG on Si/SiO₂ substrate. It was determined that although SiO₂ and Si have higher absorptivity and lower damage thresholds than SLG at the 343 nm wavelength, that at an optimal energy (120 nJ/pulse) and scanning speed (300 μ m/s) graphene can be ablated without damage to the substrate due to nonlinear absorption shielding of graphene.

Lin *et al.* [54] demonstrated the ability to control the removal of graphene layers from multi-layered graphene using ps laser irradiation. The experiment used a 1064 nm laser with a spot size of 30 μ m and fluences ranging from 0.4 – 1.1 J/cm² depending on the number of layers to be removed. The repetition rate was 2 MHz at a scanning speed of 100 mm/s. The researchers believe that although the photon energy at 1064 nm is less than the C-C bond energy required to break bonding and sublimate graphene, there exists

much weaker bonding on grain boundaries that the photons are able to break before peeling off the graphene layer. The grain sizes of the graphene were found to be about 1 μm , and it is thought that the threshold fluence will increase with increasing grain size.

Dong *et al.* [55] conducted laser micropatterning of SLG on SiO_2 using a 1030 nm wavelength, 280 fs pulse width laser. They were able to achieve microchannels in graphene of 1.6 μm without damage to the underlying substrate and found the ablation threshold to be 66 – 120 mJ/cm^2 depending on the number of pulses, scanning rate and repetition rate, which is lower than that of Si at the same wavelength (340 mJ/cm^2). There was, however, some swelling of the Si substrate due to thermal expansion. The lower ablation threshold of multiple pulses compared to a single pulse was accounted for by the incubation effect and found to be in good agreement with previous work.

Bobrinetskiy *et al.* [56] studied the impact of defects in graphene on the ultrafast laser micromachining quality using a 515 nm wavelength laser in the fs and ps regime. They found that at fluences just under the threshold value that the presence of wrinkles and bilayer islands in the beam path leads to local cracks that can be undesirable in electronic device applications. They also found that for both 20 ps and 280 fs pulses at relatively high energies and low pulse overlaps that numerous folds and cracks are produced, but for 280 fs pulses at relatively low energies and a high number of pulse overlaps that very clean patterns with straight edges are produced.

Gil-Villalba *et al.* [57] studied the effect of laser spot diameter on ablation of SLG for single shot 130 fs pulses at 800 nm wavelength with a Bessel beam distribution. They found that the probability of ablation decreases significantly for small spot diameters even when the ablation threshold is exceeded. It was also determined that large fluence gradients due to focusing results in explosive folding of graphene and that the probability of ablation is much higher in the vicinity of wrinkles than for islands at relatively low fluences. This is thought to be due to wrinkles and defects in graphene acting as barriers for energy diffusion leading to higher ablation probabilities.

2.7.1 Printed Graphene-Oxide (GO) Ablation Experiments

The use of laser micromachining to create graphene-based printed electronic devices has been studied for different end-use applications. In 2014, Sinar *et al.* synthesised a GO ink from graphite powder for DoD printing onto a flexible substrate where it was then thermally annealed by laser writing to improve conductivity and laser micromachined where ideal processing parameters were determined. It was found that an efficient reduction was achieved under a surface temperature of 300° C with the surface temperature being directly proportional to the laser power. Several observations were made relating the precise control of parameters to annealing quality. The researchers noted that higher laser powers are required for shorter annealing times and that feed rate must be controlled where a feed rate that is too fast will cause gaps in annealing but a feed rate that is too slow will cause damage to the film. For best conductivity the film was laser annealed over multiple passes. For laser micromachining, the researchers were able to produce feature sizes of 2 – 3 µm and achieved single pass ablation with a 775 nm wavelength laser with a pulswidth of 120 fs, average power of 0.15 mW and feed rate of 25 mm/min [58].

Chang *et al.* [8] used a 14 W, 28 ns pulse width, 355 nm wavelength laser to micromachine a printed graphene film on a glass substrate. Single line ablation was achieved using a fluence of 16.3 J/cm², a pulse frequency of 100 kHz, and at a feed rate of 250 mm/s for 75 pulses. A line width of 30 µm was achieved. It was noted that cracks were present after laser micromachining due to the residual stress difference between irradiated and non-irradiated areas and that high pulse energies melted the film layer and damaged the underlying substrate. A lower fluence of 0.32 J/cm² prevented cracks but produced graphene flake structures on the substrate.

Tseng *et al.* [7] studied the laser patterning of GO films to create a multichannel electrode structure for rapid heating chips. They determined the ideal processing parameters to be a fluence of 4.72 J/cm², frequency of 300 kHz, scan speed of 1500 mm/s with line spacing of 1 µm using a picosecond laser. An ablation depth of 14.2 µm was achieved with a pulse overlap of 94%.

Tseng *et al.* [59] extended their studies in 2021 to produce a strain electrode for sensing glass deformation with screen-printed graphene. The optimal parameters for graphene

removal were determined to be an areal fluence of 31.9 J/cm^2 , pulse frequency of 300 kHz, and scan speed of 500 mm/s. The researchers found that increasing the areal fluence causes an increase in surface roughness for small fluences but at larger fluences causes a decrease in surface roughness. It was reported that the ablated areas resulted in clean edges with no residual debris.

2.7.2 Graphene-Oxide (GO) Annealing Experiments

In 2008, Jung *et al.* [25] were able to control the amount of thermal reduction in graphene oxide sheets in order to tune the electrical conductivity. The single layer graphene oxide sheets were fabricated and connected with metal leads where electrical conductivity was measured through the 4-point probe technique. Heating was performed using an underlying hot plate and temperatures were recorded using a thermometer. The thermal loading was conducted in phases of heating and cooling at $1^\circ\text{C}/\text{min}$ where it was found that the electrical resistance of graphene oxide decreases with increasing temperature shown in Figure 2.15.

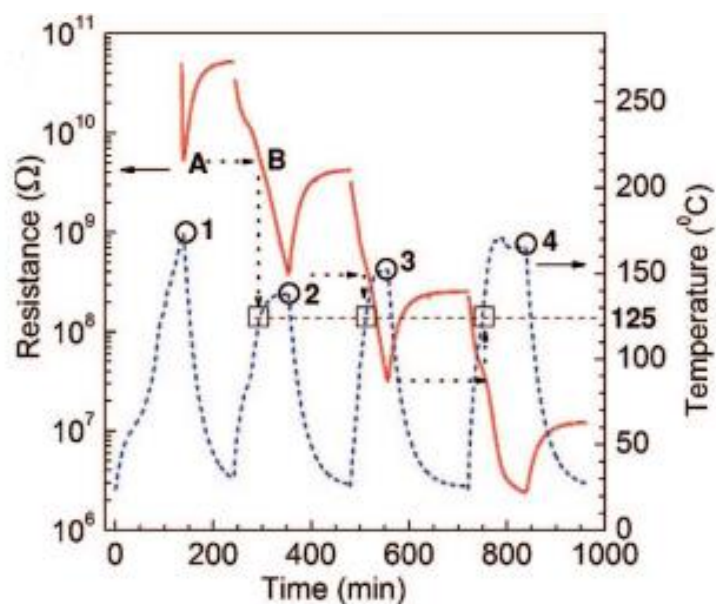


Figure 2.15 Change in graphene oxide electrical resistance and temperature with time (Reprinted with permission from [25] Copyright 2008 American Chemical Society).

Huh *et al.* [10] used several techniques to characterize the temperature-dependent reduction of GO films ranging from room temperature to 2000° C. The GO was prepared by the Hummers method and spin-coated onto a Pt substrate to give a film thickness of 300 to 500 nm. Five critical temperature ranges were identified as thresholds for reduction and shown in Figure 2.16. From R.T.–130° C mild vaporization of intercalated H₂O molecules occur causing lattice contraction. This reduction is increased much further from 140° C – 180° C. In the range of 180° C – 600° C residual carboxyl and partial hydroxyl groups are removed. At 800° C – 1000° C epoxide groups are removed resulting in many defects and in-plane C bond cracking. Finally, from 1000° C – 2000° C defects are decreased due to layer stacking and crystal growth.

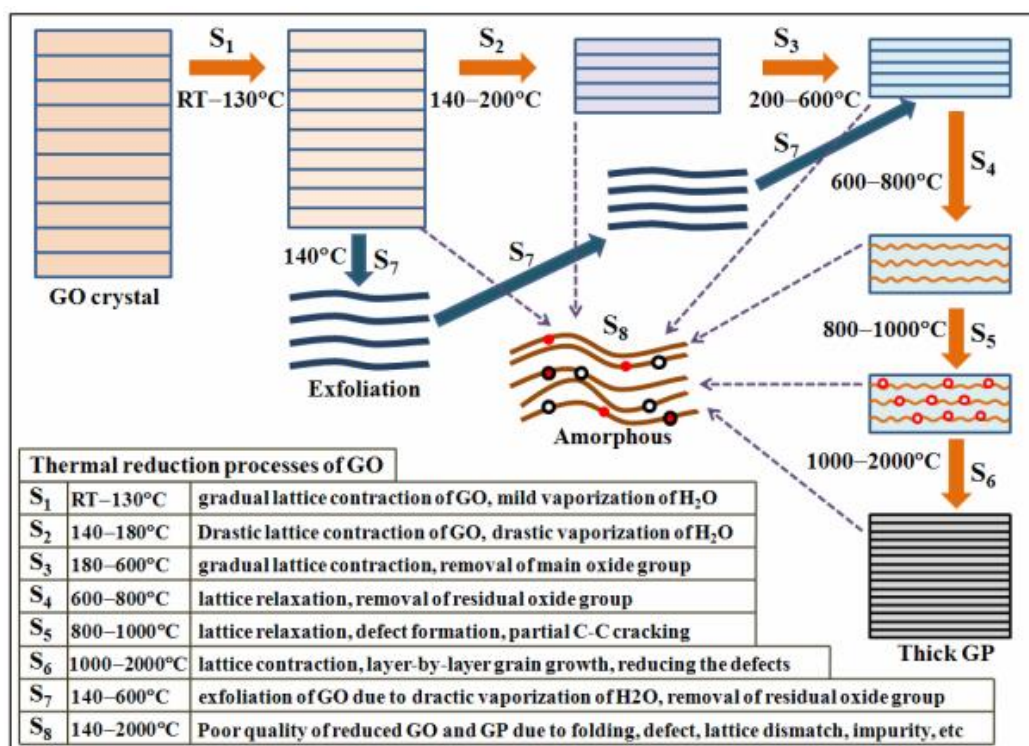


Figure 2.16 Temperature ranges and processes for thermal reduction of GO © 2011, Seung Hun Huh. Originally published in [10] under Creative Commons Attribution-NonCommercial-ShareAlike-3.0 license. Available from: 10.5772/14156

Strong *et al.* [26] performed laser scribing of graphene oxide films to make circuits directly patterned onto flexible substrates without the need for complex post-processing techniques. The researchers used a 5 mW, 788 nm laser from a commercial device that creates grayscale images on certain CDs/DVDs by adjusting a lens and focuses or defocuses the laser irradiation on a dye matrix where a computer program controls the level of grayscale. The device was altered to instead apply the pulsed laser irradiation to a graphite oxide layer to be reduced. From Figure 2.17 it is seen that the change in sheet resistance is based on the number of reductions and level of grayscale and it was determined that graphene oxide conductivity could be improved from 20 M Ω /sq to 80 Ω /sq. From this technology, the researchers were able to construct flexible interdigitated electrodes for use in an NO₂ gas sensor.

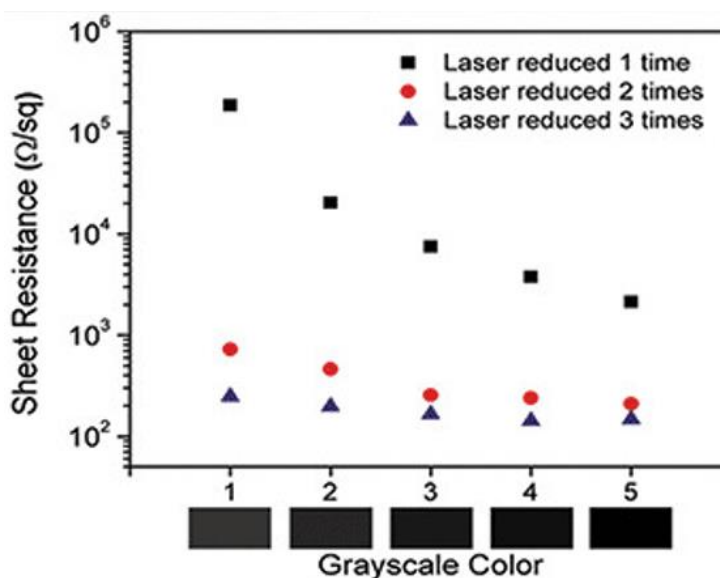


Figure 2.17 Sheet resistance of rGO as a function of laser intensity corresponding to grayscale color from laser program (Reprinted with permission from [26], Copyright 2012 American Chemical Society).

Sinar *et al.* [60] used ultrashort pulsed laser irradiation to anneal inkjet printed GO electrode traces and improve electrical conductivity. A 775 nm, 120 fs laser was used for heating where the degree of electrical resistivity reduction was a function of the laser

power, feed rate, and number of passes. Experiments were conducted with a laser spot size of $220\ \mu\text{m}$ with average powers ranging from $18 - 29\ \text{mW}$, feed rates ranging from $1000 - 2000\ \text{mm/min}$, and number of passes ranging from $6 - 20$. Figure 2.18 shows the results of the experiments where the optimal parameters for GO reduction appear to be $20 - 21\ \text{mW}$ and $1200\ \text{mm/min}$.

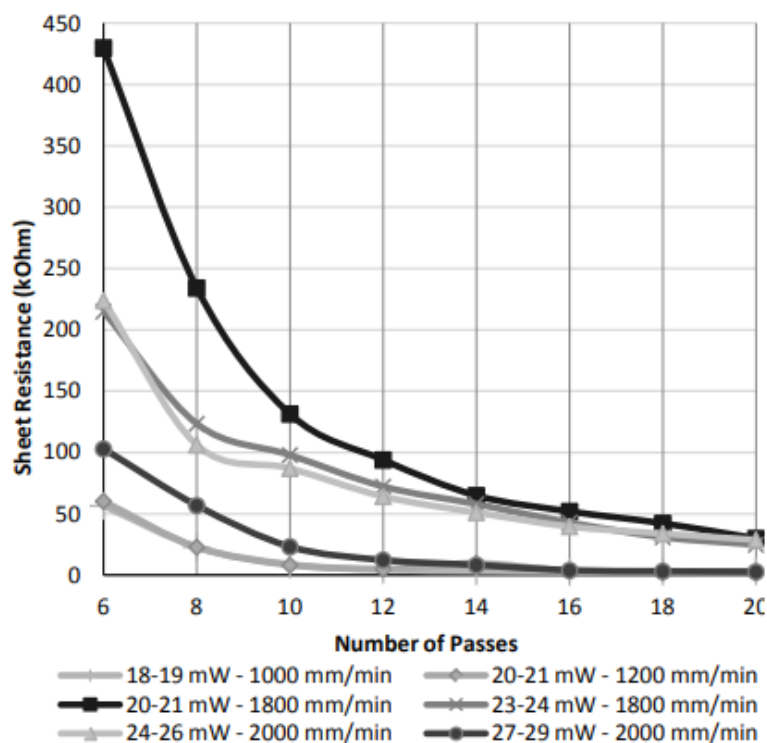


Figure 7. Sheet resistance values for rGO traces printed on glass. In general, higher NP produces smaller R_s values.

Figure 2.18 Sheet resistance of rGO as a function of number of laser passes, laser power and scan speed © [2014] IEEE. Reprinted, with permission, from [Sinar *et al.*, Laser assisted reduction of printed GO films and traces]

2.8 Mathematical Models for Laser Ablation

Although ultrashort laser irradiation and ablation models have been applied extensively to metals, there has been limited studies concerning the numerical modelling and simulation for ultrashort laser irradiation of graphite and graphene. In 2017, Ren *et al.* [61] used FEA

to study nanosecond pulsed laser ablation of copper, silver, silicon and few-layer graphene. Since the pulse width is in the nanosecond regime, the ablation mechanism was assumed to be normal boiling and the material removal velocity followed by

$$V_n = \frac{q_a}{\rho} \cdot L_s \quad (2.11)$$

where V_n is the material removal velocity (m/s), q_a is the ablative heat flux (W/m^2), ρ is density and L_s is the latent heat of sublimation (J/kg). After modelling, it was found that copper and silver undergo similar ablation depths with silicon being significantly less and graphene experiencing no ablation. This is likely due to graphene having a very high thermal conductivity that allows thermal energy to dissipate throughout the material and due to its high boiling point, which wasn't reached in the simulations.

Sinha [62] performed a simulation using the finite difference methods for ns laser ablation of graphite. The model accounted for the attenuation of laser light from the vapour plume using fitting parameters. The model simulates laser ablation from a 10 Hz, 5 ns, 532 nm laser due to normal boiling and compares it to experiment. The model predicts the transition from normal boiling to explosive boiling which occurs at $\sim 25 \text{ J}/\text{cm}^2$ when the critical temperature is reached, and simulated results were found to agree well with the experiments up to the explosive boiling fluence threshold. Differences between experiment and simulation were attributed to degradation of the material due to melting, ablation, and removal of surface layers.

Wang *et al.* [63] conducted a two temperature model (TTM) simulation to investigate the picosecond laser ablation of stainless steel. Phase explosion was simulated where the material removal is modelled by the deformed geometry module in COMSOL Multiphysics. Once 90% of the critical temperature was reached in the simulation, material is removed at the sonic speed in stainless steel. The simulation is compared to experiment where a 10 ps, 532 nm laser is used with $16 \mu\text{m}$ spot size and fluences ranging from $5.97 - 18.41 \text{ J}/\text{cm}^2$. The simulated single pulse ablation depth and diameter were found to be larger than that in the experiment but the overall trend with fluence was the same.

2.9 Concluding Remarks

This chapter was an introduction to the fundamental concepts of laser-material interaction and laser micromachining, as well as an overview of the key material properties for graphite, graphene, and graphene oxide. A state-of-the-art review was provided for the known thermal, optical and phonon properties of graphene and graphite. A review of laser experiments was also given for HOPG, rGO and SLG providing the reader with insight into how these materials react to ultrashort laser irradiation and the necessary laser parameters to anneal or ablate the material. Section 2.8 described the numerical models for different materials that will be built upon in Chapters 3 and 4 for simulating the laser material processes used to micromachine HOPG, SLG, and rGO thin films.

Chapter 3 Finite Element Analysis of Ultrashort Laser Pulses Irradiating Graphitic Materials

3.1 Introduction

Computer simulations using finite element analysis (FEA) have been extensively used by both engineers and researchers to understand and solve physics problems in fields such as structural engineering, fluid dynamics, heat transfer and electromagnetism. FEA has been employed in the study of laser irradiation to determine ideal processing parameters for device fabrication without the need to run physical experiments which can be time consuming and costly.

The following chapter outlines the 1D and 2D variations of a model developed using COMSOL Multiphysics that studies the temperature distribution and resultant material removal due to ultrashort laser pulses irradiated onto graphitic materials. A brief introduction on COMSOL Multiphysics will be provided, followed by a description of the two-temperature model to be implemented, as well as the equations, material properties, mesh and solver selection, and assumptions made focusing on the case for ultrashort laser ablation of highly oriented pyrolytic graphite (HOPG). Chapter 4 will apply the model for printed rGO and then extend the model into the multitemperature model (MTM) for SLG where it will be compared with the TTM. Chapter 5 covers parametric simulations for different laser parameters and substrate materials and discusses the influence of these parameters on ablation and annealing.

3.2 Finite Element Modelling (FEM)

Finite element modelling (FEM) is a numerical method that obtains an approximate solution to a differential equation by dividing a domain into a set of smaller domains with corresponding equations. These are then approximated over the entire domain creating an unknown equation that can be solved through calculus of variations. FEA is the process of

studying a physics problem using FEM and is used in engineering to analyze problems including structural mechanics, heat transfer, fluid mechanics and electromagnetism.

The division of a domain into smaller elements is known as discretization and the entire set of elements is called the mesh. Elements are connected in the mesh by nodes which lie on the boundaries of elements where the unknown variable to be solved for is assigned to each node. A set of approximation functions are defined for each element that express the variation of the unknown variable within the element. Due to the ease of integration and differentiation, polynomials are commonly used as approximation functions, but the degree of the polynomial is dependent on continuity between elements, the number of unknowns to be solved for and the number of nodes in each element. Solutions for each element are solved using a mathematical method called the Galerkin method that aims to minimize the approximation error before assembling the equations into a system of equations to represent the entire domain. In order to solve the system of equations boundary conditions must be applied, which are known values of the variable to be solved for at some positions in space or time. After the physics problem is solved using FEM, additional variables can be solved for, such as heat flux or mass removal rate from temperature [64].

FEA can be divided into three types of problems being time-independent, time-dependent and eigenvalue. Time-independent problems are considered to be in equilibrium such as solving for pressure, velocity, temperature, or density distributions in steady state fluid mechanics. Time-dependent problems account for changes in a variable over time such as how long a heated material takes to reach thermal equilibrium. Eigenvalue problems relate to steady state conditions where natural frequencies or vibrational modes must be determined.

3.3 COMSOL Multiphysics

COMSOL Multiphysics is an FEA simulation software that is able to perform multiphysics simulations where multiple types of physics can be simulated and solved for a system simultaneously. The software has pre- and post-processing capabilities inside an integrated development environment. Before any simulations are performed, COMSOL provides tools for geometries to be created or imported for use as the modelling domain. Next the

physics interfaces are selected with COMSOL containing a variety of predefined Multiphysics problems that include suggested settings for the solver, discretization, visualization and postprocessing. These settings and physics interfaces are fully customizable for any type of problem and the user can input their own differential equation to be modelled. For meshing, many types of mesh shapes and patterns are available that can be tailored for accuracy or simulation time depending on the physics problem. Parametric sweeps can be performed allowing for a series of simulations to be run with each having different parameters for the geometry, material, equation inputs or settings. COMSOL also provides many post-processing tools for 1D, 2D or 3D plots as well as numerical tools for evaluating expressions such as max, min, average, integrals, and derivatives.

The experiments presented in this thesis make use of the heat transfer in solids and deformed geometry modules to determine the temperature distribution after laser irradiation and the subsequent material removal due to ablation. Figure 3.1 shows a list of predefined heat transfer interfaces for different heat transfer problems which are compatible in 1D, 2D, 2D axisymmetric, and 3D space for transient and stationary studies.

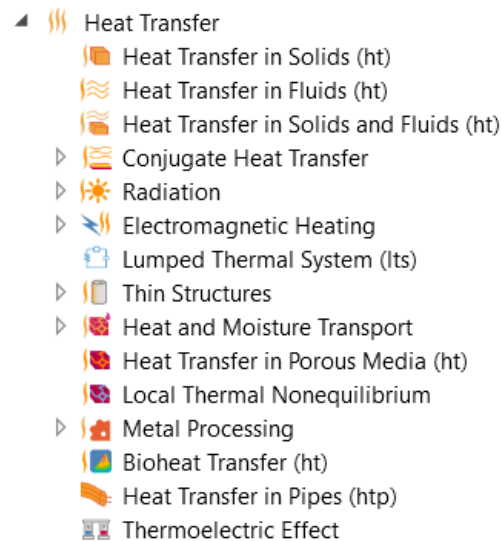


Figure 3.1 Predefined heat transfer modules in COMSOL Multiphysics.

The work in this thesis uses both 1D and 2D models where the 1D temperature distribution and ablation depth can be solved for multiple pulses at relatively fast computation times in 1D and single pulse 2D temperature distribution and ablation profile can be modelled in 2D although taking much longer times to compute.

3.4 Two Temperature Model (TTM)

The two-temperature model (TTM) is an extension of the heat transfer equation that is used for ultrashort laser simulations and is in excellent agreement with experimental results for both metals and semiconductors. When modelling ultrafast laser irradiation, there are three steps that must be considered. The first is the laser radiation absorption by electrons, and since the heat capacity for electrons is very small, the temperature of electrons will increase rapidly to extreme temperatures while the lattice remains cold. The second step is the exchange of energy from the electrons to the lattice which can take place over tens or hundreds of picoseconds depending on the material properties and laser intensity. The final step occurs when thermal equilibrium between the electrons and lattice is reached. The TTM was first introduced by Qiu *et al.* in 1993 [65] by solving the Boltzmann transport equation through quantum mechanical methodology and developing a hyperbolic two-step radiation heating model. The set of equations is shown in Equation 3.1 and 3.2.

$$\rho C_e \frac{\partial T_e}{\partial t} = \nabla(k_e \nabla T_e) - G_{ep}(T_e - T_l) + Q(r, z, t) \quad (3.1)$$

$$\rho C_l \frac{\partial T_l}{\partial t} = \nabla(k_l \nabla T_l) + G_{ep}(T_e - T_l) \quad (3.2)$$

where C_e is the electron specific heat capacity (J/kg · K), T_e is the electron temperature (K), k_e is the electron thermal conductivity (W/m · K), G_{ep} is the electron-phonon coupling constant (W/m³K), T_l is the lattice temperature (K), C_l is the lattice specific heat capacity (J/kg · K), k_l is the lattice thermal conductivity (W/m · K) and $Q(r, z, t)$ is the source term. Under the TTM, electrons are first to absorb laser radiation and will heat very quickly and to very high temperatures compared to the lattice due to the small heat capacity of the free electrons. Following the electron heating, the energy is exchanged between the electrons and the lattice systems by means of the electron-phonon coupling constant. This process

can range from several picoseconds to over a hundred picoseconds depending on the electron-phonon constant of the material and laser fluence. The final process is the thermal equilibrium achieved by the electron and lattice system where the lattice can reach temperatures high enough to cause phase change if the energy exchange from the electrons is large and quick enough.

The total heat capacity and thermal conductivity are the sum of the respective electronic and lattice contributions. Since the electron temperature varies by a large amount during irradiation, temperature dependent parameters for specific heat capacity and thermal conductivity must be used to calculate reasonably accurate temperature distributions. These parameters can be very difficult to determine experimentally but can be approximated by different relations. At temperatures below the Fermi temperature a linear heat capacity can be approximated from the Sommerfield expansion model in

$$C_e = C'_e T_e \quad (3.3)$$

where C'_e is the electron heat capacity constant. At temperatures near and above the Fermi temperature, C_e can be considered constant and calculated from

$$C_e = \frac{3N_e k_B}{2} \quad (3.4)$$

where N_e is the electron density and k_B is the Boltzmann constant (1.38×10^{-23} J/K). For simplicity, the specific heat capacity just below and above the Fermi level can be approximated by calculating the electron temperature in Equation 3.5 at which the specific heat capacity becomes constant, if the electron density is not easily determined

$$T_e = \frac{3T_F}{\pi^2} \quad (3.5)$$

where T_F is the Fermi temperature. The electron thermal conductivity also follows a temperature dependent relation. At temperatures below the Fermi temperature the electron thermal conductivity is expressed by

$$k_e = k_{e0} \frac{BT_e}{AT_e^2 + BT_l} \quad (3.6)$$

where A and B are material constants and k_{e0} is the electron thermal conductivity at ambient temperature. The thermal conductivity becomes underestimated at temperatures much larger than the lattice temperature, and therefore Equation 3.7 must be used which is valid at high temperatures,

$$k_e = C \frac{(\theta_e^2 + 0.16)^{\frac{5}{4}} (\theta_e^2 + 0.44) \theta_e}{(\theta_e^2 + 0.092)^{\frac{1}{2}} (\theta_e^2 + s\theta_l)} \quad (3.7)$$

where $\theta_e = \frac{T_e}{T_F}$ and $\theta_l = \frac{T_l}{T_F}$, and the material constants C and s are determined by matching the low temperature progressions of Equation 3.7 to that of Equation 3.6 [66].

In the case of graphite and graphene it is believed that the electronic contribution to thermal conductivity is very small ($\sim 1\%$) and that other relations must be used to properly determine the temperature dependent thermal conductivity and specific heat capacity compared to metals [35]. The Wiedemann-Franz law can be used to determine the temperature dependent electron thermal conductivity from electrical conductivity where it has been found to be broadly satisfied although deviating by 20 – 50% at temperatures near the room temperature. The Wiedemann-Franz law states that the ratio of the electron thermal conductivity to electrical conductivity is proportional to the temperature shown in

$$k_e = L_0 T_e \sigma \quad (3.8)$$

where L_0 is the Lorenz ratio ($2.44 \times 10^{-8} \text{ V}^2 \text{ K}^{-2}$), and σ is the electrical conductivity (S/m). The electron specific heat capacity can then be determined through the electron thermal conductivity from

$$C_e = \frac{k_e}{v_F \lambda_E} \quad (3.9)$$

where v_F is the Fermi velocity (m/s) and λ_E is the mean free path of charge carriers (nm) [67].

3.5 Laser Ablation of Highly Oriented Pyrolytic Graphite (HOPG)

The model being presented in this section will use an ultrashort laser ablation of HOPG experiment as the example model to be described. For annealing experiments and different materials, the alterations will be explained in their respective sections. The following model aims to simulate the experiment performed by Shirk *et al.* [45] where 120 fs pulses from a Ti:Sapphire laser at a wavelength of 825 nm are shot at a sample of 1.2 μm thick HOPG with fluences ranging from 0.5 to 10 J/cm^2 . The following model simulates the single and multi-pulse ablation depth at different fluences and will be compared to the results obtained from the physical experiment for validation.

3.5.1 Equations Describing Laser Beam Intensity

Since the laser used in the experiment by Shirk *et al.* [45] operates in the fs regime, the TTM must be used for simulation as outlined in Section 3.4 using Equations 3.1 and 3.2. Based on the desired computation time and information to be simulated, the simulation can be performed in either 1D or 2D which changes the source term in Equation 3.1. For a 1D model, only the depth of the material at the centre of the laser spot in the form of a line is simulated resulting in much shorter computation times which allows for many pulses to be simulated. The difference between the equations of a 1D and 2D simulation can be found in the laser intensity term. The source term is represented by

$$Q(z, t) = (1 - R)I(t)\alpha \exp(-\alpha(-z)) \quad (3.10)$$

where $I(t)$ is the laser intensity. The laser intensity for a 1D TTM is represented by

$$I(t) = \frac{2E_p}{\pi\omega_0^2\tau_p} P(t) \quad (3.11)$$

where $P(t)$ is a function representing the pulse magnitude over time. The laser intensity for a 2D TTM is represented by

$$I(r, t) = \frac{2E_p}{\pi\omega_0^2\tau_p} P(t) \exp\left(-2\left(\frac{r}{w_0}\right)^2\right) \quad (3.12)$$

where the additional term represents the Gaussian distribution of the laser spot in the radial direction. The pulse magnitude function $P(t)$ representing 120 fs is shown in Figure 3.2.

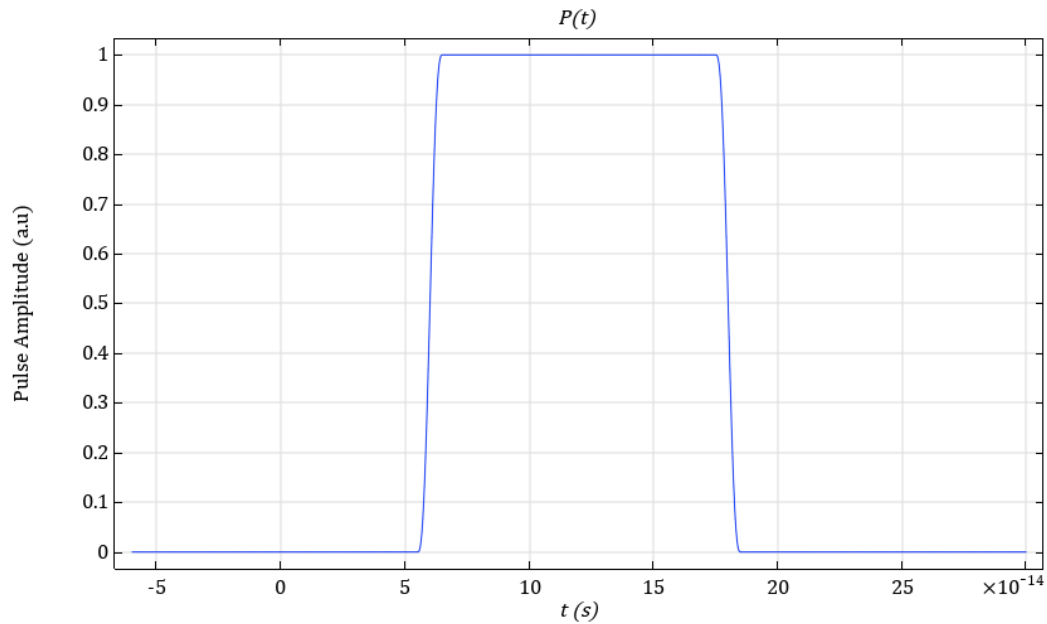


Figure 3.2 Magnitude of the pulse $P(t)$ over time for 120 fs pulse.

3.5.2 HOPG Modelling Domain

The modelling domain used in the simulation varies based on if a 1D or 2D simulation is performed. In a 1D simulation, the domain is a straight line representing the depth of the material at the centre of the laser spot while a 2D axisymmetric domain represents a radial cross-section of the material. Figure 3.3 shows a visualization of the 1D and 2D axisymmetric domain. Since the Gaussian distribution is identical on both sides of the z -axis the axisymmetric domain is used to reduce computation time.

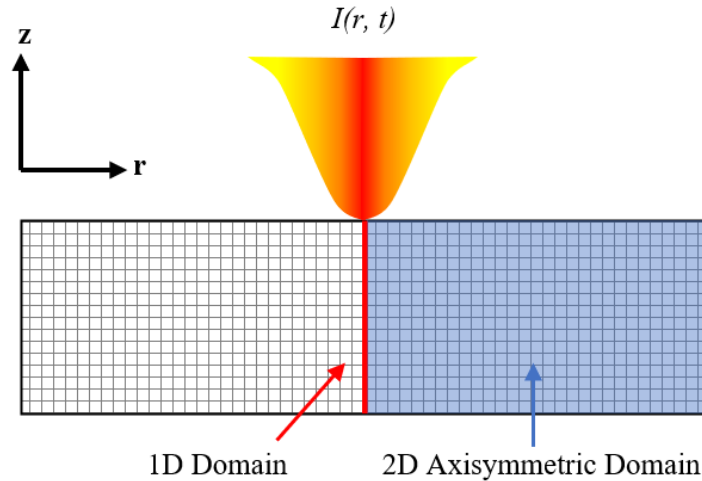


Figure 3.3 Visualization of the domain for 1D and 2D axisymmetric.

The 1D domain as shown in the COMSOL interface is shown in Figure 3.4a and an illustration of the 1D and 2D domains are shown in Figure 3.4b, where node 1 corresponds to a depth of 0 μm at the surface of the substrate and node 2 represents the bottom of the substrate.

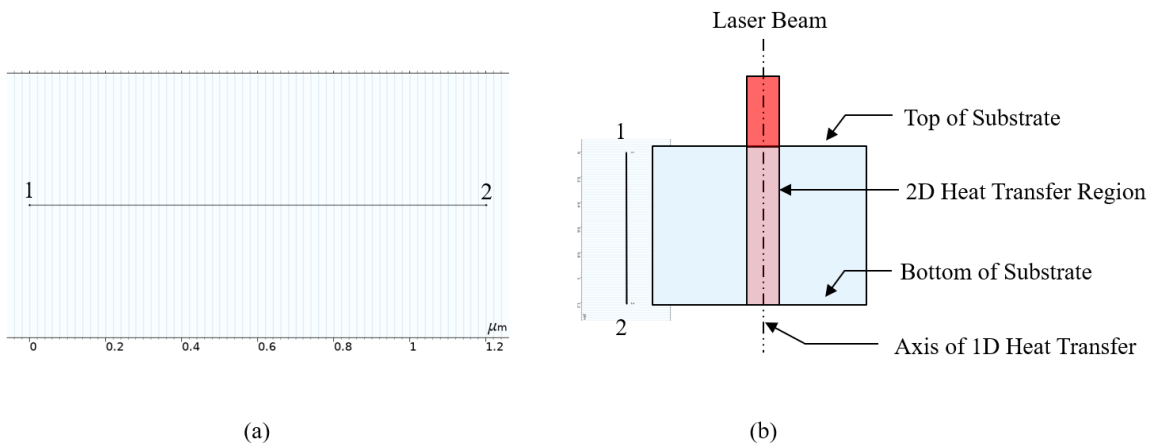


Figure 3.4 (a) 1D domain representing the material depth at the centre of the laser spot. (b) Illustration of 1D and 2D modelling domains. Figure 3.4a is oriented next to the illustration and represents the axis of 1D heat transfer.

The 2D axisymmetric domain as shown in the COMSOL interface is shown in Figure 3.5 and represents one half of the material with the laser pulse being applied at $r = 0$ and $z = 0$.

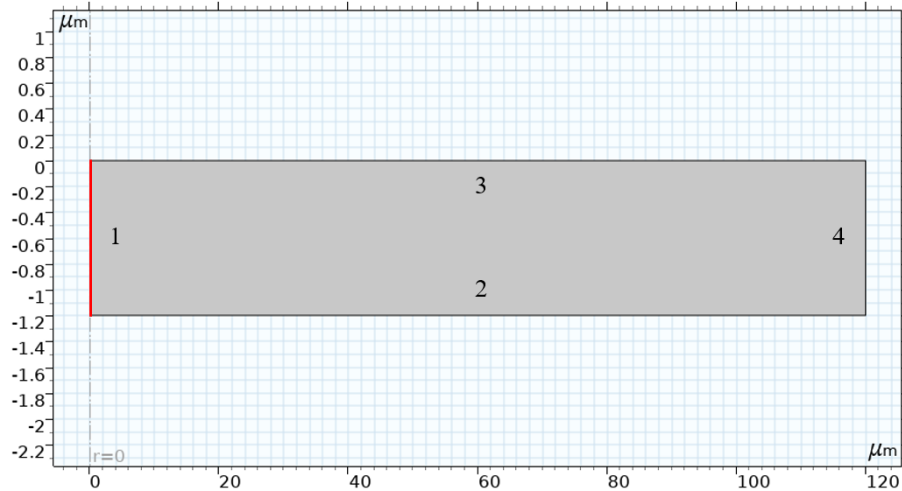


Figure 3.5 2D axisymmetric model domain where the heat source is applied to the surface 3. Red line shows 1D domain.

3.5.3 Material Properties of HOPG Films

Material properties for highly oriented pyrolytic graphite (HOPG) are determined based on some that are given in the experiment by Shirk *et al.* [45] and others from literature. Several assumptions are made for both the material properties and the experimental modelling which are summarized in Section 3.6.4. A complete list of material properties and laser parameters used in this model are outlined in Table 3.1.

3.5.3.1 Surface Reflectivity

As previously stated in Section 2.2 the reflectivity of a material depends on the wavelength of incident light and is determined from the complex refractive index from Equation 2.7. Optical experiments performed by Song *et al.* [38] determined the refractive index and extinction coefficient for HOPG at wavelengths ranging from 31 nm to 1690 nm. At a

wavelength of 825 nm, the refractive index and extinction coefficient were reported to be 2.59 and 1.39 respectively leading to a reflectivity of 0.301.

3.5.3.2 Linear Absorption Coefficient

Also stated in 2.2 Optical Absorption and Laser Micromachining, the linear absorption coefficient depends on the wavelength of incident light determined by the extinction coefficient from Equation 2.5. At 825 nm the linear absorption coefficient was determined to be $2.12 \times 10^7 \text{ m}^{-1}$.

3.5.3.3 Electron Thermal Conductivity

As described in Section 2.6, the electron thermal conductivity can be determined by the Wiedemann-Franz law in Equation 3.8 and depends on the electrical conductivity and electron temperature of the material. Since graphite is an anisotropic material, the thermal conductivity will not be the same along the c-axis and ab-plane and must be accounted for in the model. The electrical resistivity of the HOPG sample used in the experiment by Shirk *et al.* [45] was given for both the c-axis and ab-plane where the electrical conductivity is determined from the reciprocal of the resistivity. The electrical resistivity for the c-axis and ab-plane were reported to be $0.5 \text{ } \Omega \cdot \text{cm}$ and $0.5 \times 10^{-3} \text{ } \Omega \cdot \text{cm}$, respectively. The electron thermal conductivity as a function of electron temperature is plotted for the c-axis in Figure 3.6 and for the ab-plane in Figure 3.7.

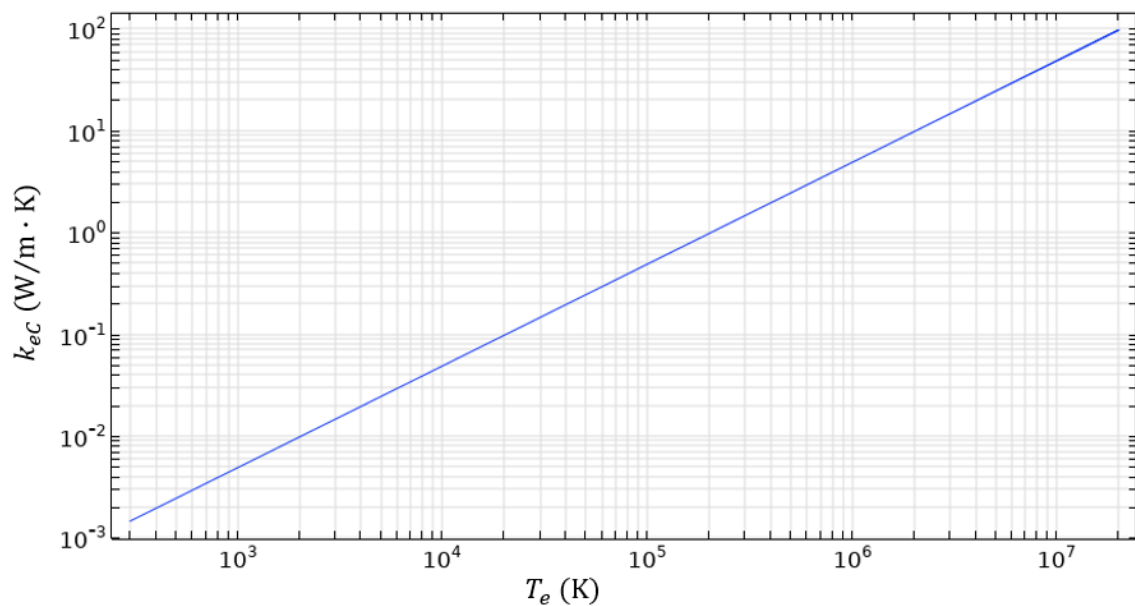


Figure 3.6 Temperature dependent c-axis electron thermal conductivity of HOPG.

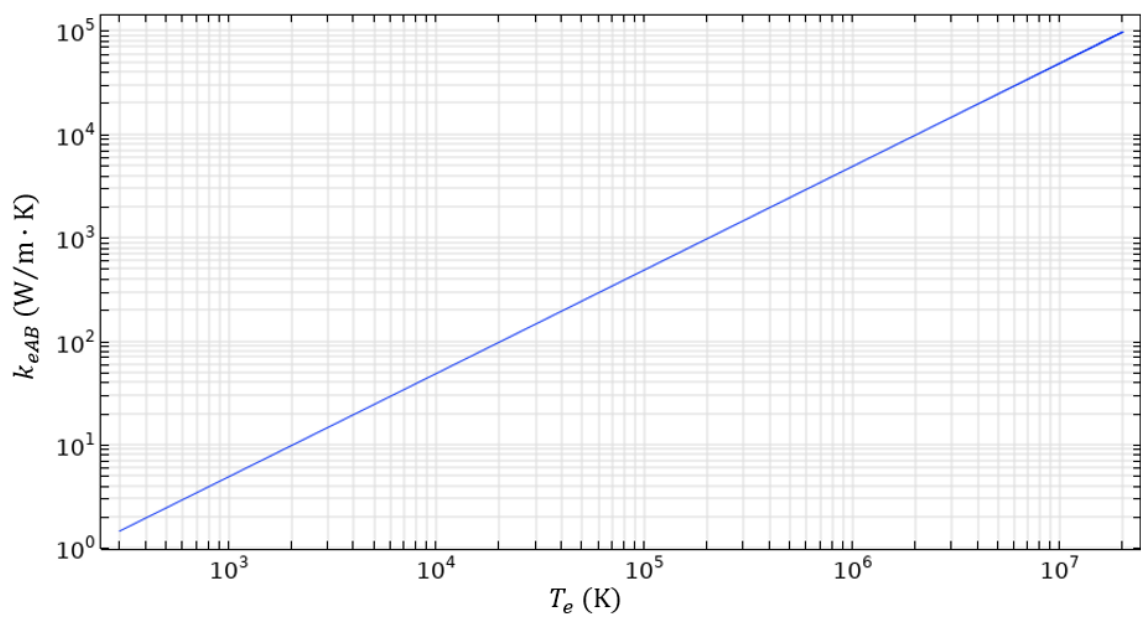


Figure 3.7 Temperature dependent ab-plane electron thermal conductivity HOPG.

3.5.3.4 Electron Specific Heat Capacity

As described in Section 2.6, the electron specific heat can be determined by Equation 3.9 and is a function of the electron thermal conductivity, Fermi velocity and mean free path of charge carriers. The Fermi velocity was determined by Zhou *et al.* [68] to be approximately 0.91×10^6 m/s and mean free path of charge carriers was found to range from 0.4 to 1 nm depending on the electron temperature based on work by Shinotsuka *et al.* [69] so an average value of 0.7 nm was chosen. Since the electron thermal conductivity is larger along the ab-plane, this value is used in Equation 3.9. A plot of the electron specific heat capacity as a function of electron temperature is shown in Figure 3.8.

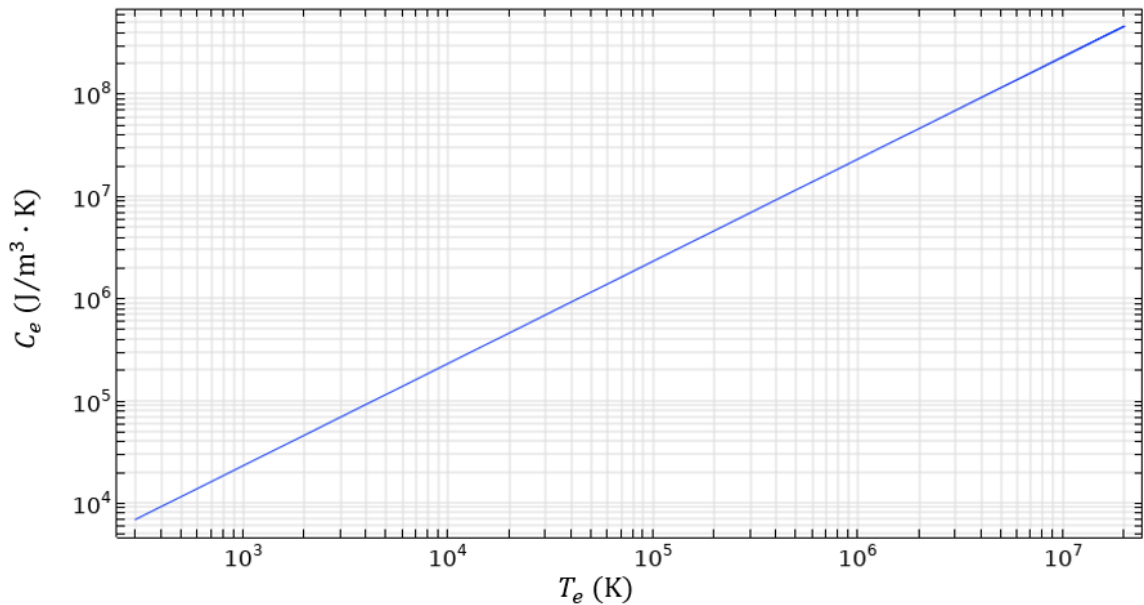


Figure 3.8 Temperature dependent electron specific heat capacity HOPG.

3.5.3.5 Additional Properties of HOPG

Additional properties that are required for the TTM equations include the electron-phonon coupling parameter, lattice heat capacity, lattice thermal conductivity, sonic speed, and critical temperature. These values were not calculated and instead obtained from experimental literature. The electron-phonon coupling constant for graphite was determined by Medvedev *et al.* [70] based on a model that calculates the temperature

dependent electron-phonon coupling constant for many materials. The value for graphite is found to be $6 \times 10^{17} \text{ W/m}^3\text{K}$ at high electron temperatures and is assumed to be constant in this model. The lattice heat capacity of HOPG is found to be $\sim 2 \text{ J/g} \cdot \text{K}$ by averaging the value obtained from temperature dependent experiments by Savvatimskiy *et al.* [71]. The lattice thermal conductivity was provided in the experiment by Shirk *et al.* [45] for both the c-axis and ab-plane and are given as 2 and 400 W/mK respectively. The sonic speed in graphite required for modelling the material removal is determined from Samsonov *et al.* [72] which is calculated as 1470 m/s. The critical temperature of HOPG is determined from calculations by Leider *et al.* [73] to be 6810 K. Table 3.1 shows a full list of HOPG material properties and Table 3.2 shows the laser parameters from the experiment by Shirk *et al.* [45]

3.6 Simulation Study of Irradiating HOPG Films

Since the material properties for HOPG and the modelling equations and domain were presented previously, the following section will present the specifics for the simulations, including the boundary and initial conditions, meshing parameters, solver settings, assumptions and finally the results. Table 3.1 gives a summary of the material properties of HOPG and Table 3.2 gives a summary of the laser parameters to be simulated.

Table 3.1 HOPG material properties.

Parameter (Symbol, Unit)	Value
Reflectivity (R , 1)	0.301 [38]
Linear absorption coefficient (α , 1/m)	2.12×10^7 [38]
C-axis electrical resistivity (R_c , $\Omega \cdot \text{cm}$)	0.5 [45]
AB-axis electrical resistivity (R_{AB} , $\Omega \cdot \text{cm}$)	0.5×10^{-3} [45]
C-axis electron thermal conductivity (k_{eC} , $\text{W/m} \cdot \text{K}$)	Figure 3.6
AB-axis electron thermal conductivity (k_{eAB} , $\text{W/m} \cdot \text{K}$)	Figure 3.7
Fermi velocity (v_F , m/s)	0.91×10^6 [68]
Mean free path of charge carriers (λ_E , nm)	0.7 [69]
Electron specific heat capacity (C_e , $\text{J/m}^3 \cdot \text{K}$)	Figure 3.8
Electron-phonon coupling constant (G_{ep} , $\text{W/m}^3 \cdot \text{K}$)	6×10^{17} [70]
Lattice heat capacity (C_l , $\text{J/g} \cdot \text{K}$)	2 [71]
C-axis lattice thermal conductivity (k_{lC} , $\text{W/m} \cdot \text{K}$)	2 [45]
AB-axis lattice thermal conductivity (k_{lAB} , $\text{W/m} \cdot \text{K}$)	400 [45]
Sonic speed (V , m/s)	1470 [72]
Critical temperature (T_C , K)	6810 [73]

Table 3.2 Laser parameters for experiment by Shirk *et al.* [45].

Parameter (Symbol, Unit)	Value
Pulse width (τ_p , fs)	120
Wavelength (λ , nm)	825
Pulse energy (E , mJ)	0.016 – 0.846
Beam diameter (d , μm)	107

3.6.1 Boundary and Initial Conditions

The following boundary conditions will be applied in the modelling of ultrashort laser irradiation of HOPG. The mention of nodes and boundaries correspond to those of Figure 3.4 and 3.5.

- (i) The initial temperature of the system is at room temperature,

$$T_e(r, z, t = 0) = T_l(r, z, t = 0) = 293.15 \text{ K}$$

- (ii) Thermal insulation for electron temperature is applied to nodes 1 and 2 in the 1D model and boundaries 2, 3, and 4 in the 2D axisymmetric model.

$$-\mathbf{n} \cdot k \nabla T_e = 0$$

- (iii) Thermal insulation for lattice temperature is applied to node 2 in the 1D model and boundaries 2 and 4 in the 2D axisymmetric model

$$-\mathbf{n} \cdot k \nabla T_l = 0$$

- (iv) A heat flux to represent ablation is applied to node 1 in the 1D model and boundary 3 in the 2D axisymmetric model

$$-\mathbf{n} \cdot k \nabla T_l = h(0.9T_c - T_l)$$

where $h = h(T_l)$ is a heat transfer coefficient that is zero when $T_l < 0.9T_c$ and increases linearly when $T_l > 0.9T_c$

- (v) A prescribed normal mesh velocity is applied to node 1 in the 1D model and boundary 3 in the 2D axisymmetric model

$$\frac{dz}{dt} \cdot \mathbf{n} = -V_n f$$

where $f = f(T_l)$ is a step function that equals zero when $T_l < 0.9T_c$ and equals one when $T_l > 0.9T_c$

3.6.2 Meshing Parameters

For the 1D model, edge elements were used to mesh the geometry with a distribution that creates smaller elements near node 1 where temperature gradients are much higher than

node 2. The mesh consists of 50 elements with a predefined distribution that has an element ratio of 10. For the 2D model a mapped mesh is used with a predefined distribution in both the r- and z-direction. The z-direction consists of 50 elements with an element ratio of 20 and the r-direction consists of 150 elements with an element ratio of 5. Figure 3.9 shows the mesh for the 1D model and Figure 3.10 shows the mesh for the 2D axisymmetric model.

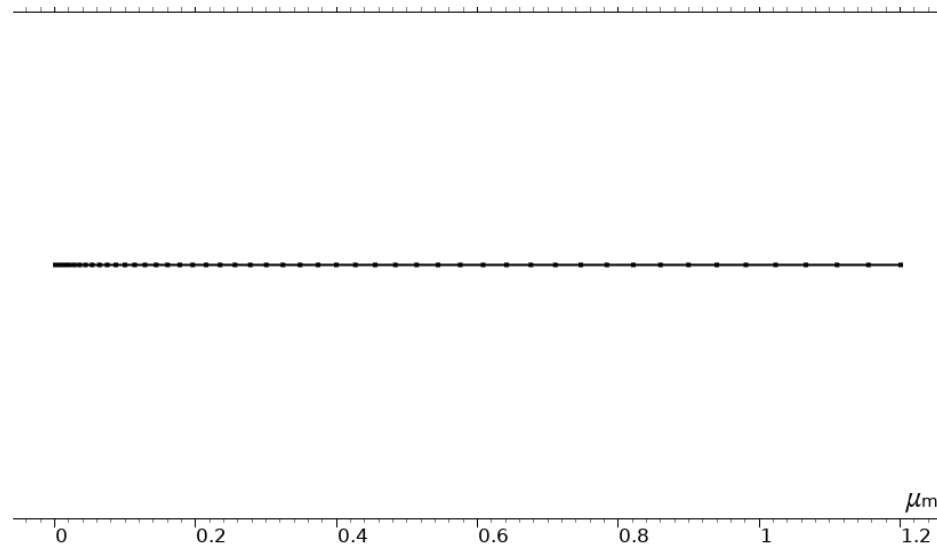


Figure 3.9 50 element mesh for 1D model representing the depth at the center of the laser spot. $0 \mu\text{m}$ represents the material surface where elements are closer together.

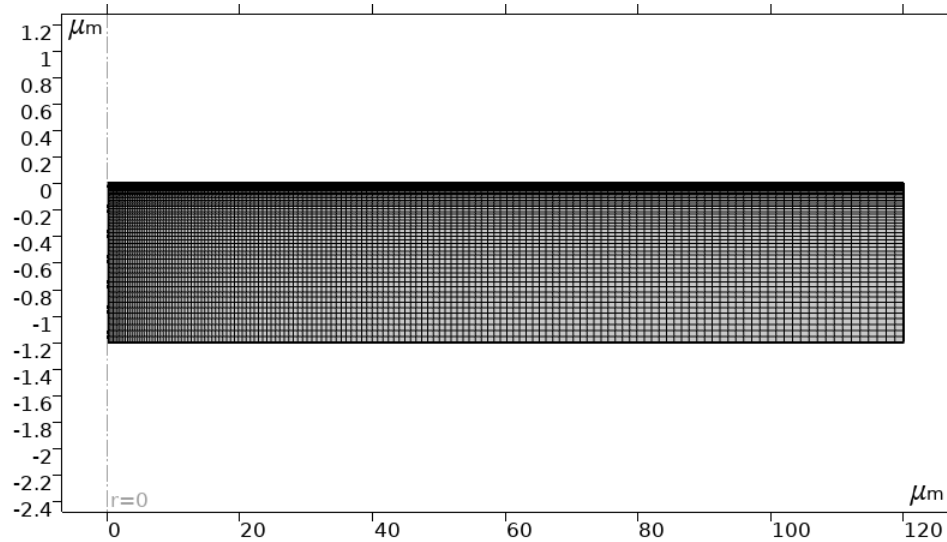


Figure 3.10 Mesh for 2D axisymmetric model representing one half of the irradiated material. A length to depth scale of 1: 20 is used. Center of laser spot is applied at the origin where elements are distributed closer to.

3.6.3 Solver Settings

A time-dependent solver is used with two different timestep ranges. A timestep of 24 fs is used for the first 50 ps followed by a timestep of 600 fs for the remaining 160 ps for each pulse. A relative tolerance of 1×10^{-4} is used. Several changes were made to the default solver settings given by COMSOL to reach convergence in the model and reduce computation times. Free time stepping was given as default but an initial timestep of 5 fs was implemented for the pulse to be resolved and the nonlinear controller was selected which enables more efficient time stepping for nonlinear models. In terms of the type of solver, a segregated approach was employed rather than a fully coupled approach due to the fully coupled approach being unable to converge on a solution. In the segregated approach each type of physics in the model is subdivided into steps that are smaller than those in the fully coupled approach and the segregated steps are solved with a single iteration requiring less memory. Under the segregated approach, it was found that using Anderson acceleration along with a constant nonlinear method and damping factor of 0.75 provides good convergence.

3.6.4 Model Assumptions

A series of reasonable assumptions have been implemented in the model and are as follows

- (i) Since the penetration depth of HOPG is ~ 30 nm and the laser beam diameter is $107 \mu\text{m}$ it is assumed that there is very little heat diffusion in the radial direction and a 1D model can be used.
- (ii) Since the laser pulse width is in the ultrashort regime, there is very little time for radiation and convection to have a significant effect on temperature and are assumed to be negligible.
- (iii) Temperature distribution is the same about the z-axis and a 2D axisymmetric model can be used.
- (iv) Effect of surface roughness is accounted for in the reflectivity measurements and a smooth surface is used in the model.
- (v) Phase explosion is the ablation mechanism since it has been employed in other models (See Section 2.8)
- (vi) Optical properties are constant with temperature since temperature-dependent properties are unavailable

3.6.5 Simulation Results for Laser Ablation of HOPG Thin Film

All the equations, domains, material properties, and boundary conditions from Section 3.3 are used to simulate the experiments by Shirk *et al.* [45] which uses a laser with properties outlined in Table 3.2. The 1D model is used to simulate ablation depth only and can simulate different fluences and multiple pulses relatively quickly. Figure 3.11 shows the electron and lattice temperature on the surface over time for a fluence of 4.2 J/cm^2 . It is seen that the electron temperature sharply increases to a maximum temperature of $9.1 \times 10^6 \text{ K}$ after ~ 180 fs before the pulse is turned off. As the electron temperature rises it transfers energy to the lattice which remains constant near $0.9 \cdot T_c$ at which point material ablation occurs. The extremely large temperatures achieved by the electrons can be attributed to the low electron specific heat capacity and electron thermal conductivity of HOPG. After 100 ps the electrons and lattice reach thermal equilibrium at which point ablation has completed and the lattice begins to cool to room temperature. Simulation results for stainless steel are provided in the Appendix for the same laser parameters. It is

seen that stainless steel reaches a much lower electron temperature due to its higher electron specific heat capacity and electron thermal conductivity.

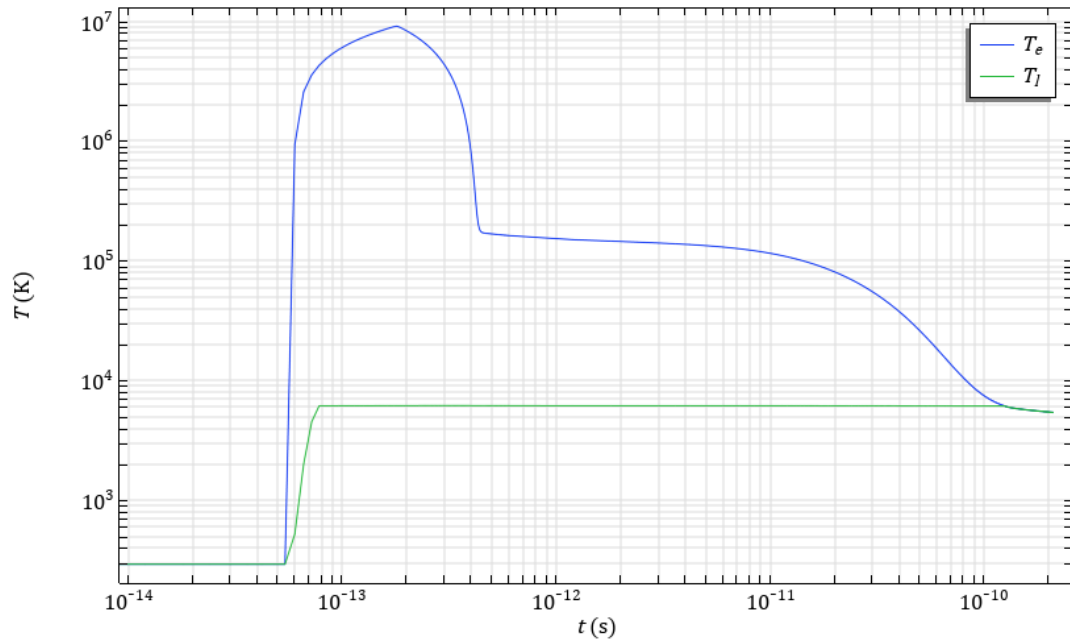


Figure 3.11 Electron and lattice temperatures over time for 4.2 J/cm^2 laser ablation of HOPG.

Another important plot to consider is the temperature distribution over the depth of the material which can be used to determine if an underlying material will be damaged during ablation. Figures 3.12 and 3.13 show the electron and lattice temperature distribution respectively over material depth at various times.

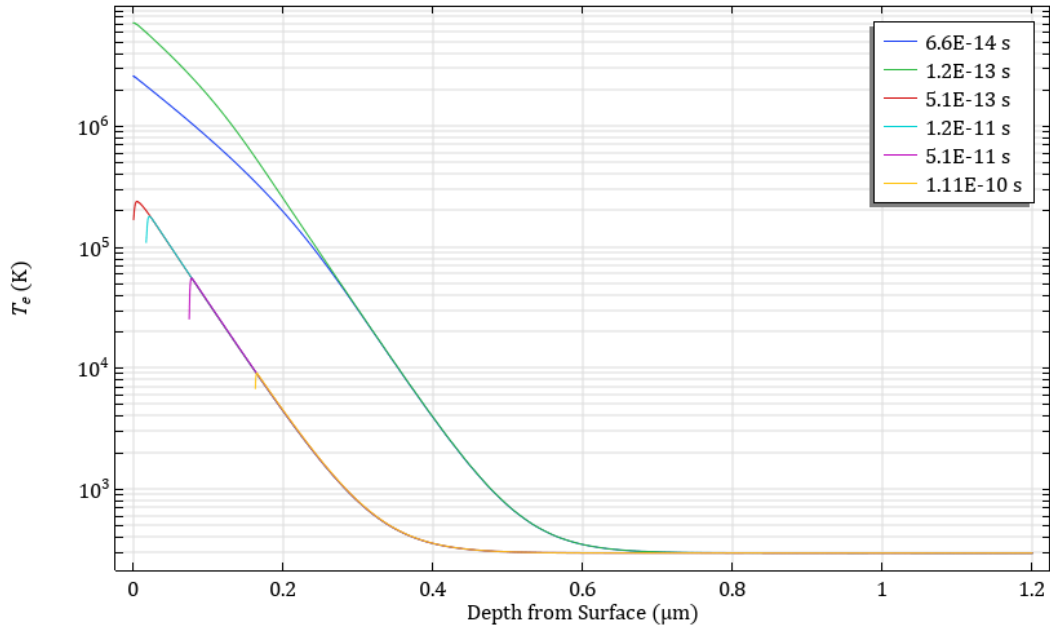


Figure 3.12 Electron temperatures with respect to depth at different times.

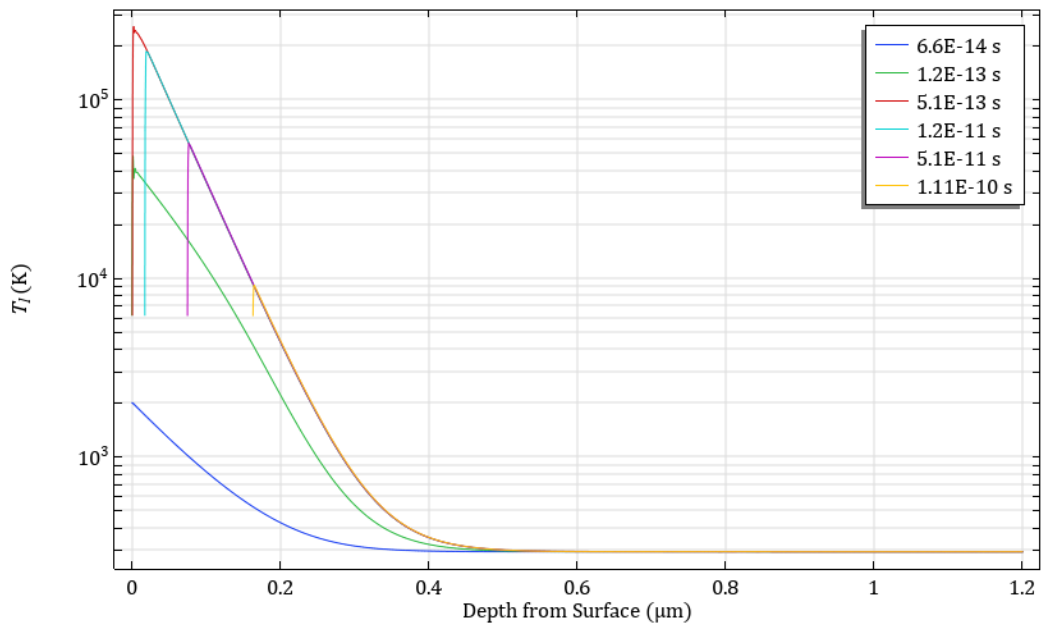


Figure 3.13 Lattice temperatures with respect to depth at different times.

From Figure 3.13, the surface temperature remains at $0.9 \cdot T_c$ required for ablation but just underneath the surface the temperature is much higher. This is due to the imposed heat

flux boundary condition where heat is removed only from the surface to keep it at the necessary ablation temperature. In reality, rather than seeing a peak above the ablation temperature, the plot would be a flat line at the ablation temperature. Although this model characteristic appears to be a mistake, the thermal energy is still conserved while heat is being removed due to ablation. The model matches well with experiment and is in line with similar ultrashort laser TTMs. Figures 3.12 shows that the electron temperature propagates further into the material than the lattice temperature likely due to the extreme peak temperatures causing a large gradient with the cool bottom layers. In Figure 3.13, the lattice temperature does not exceed room temperature past $0.6 \mu\text{m}$ into the material. Figure 3.13 also shows the material removal process as the plot lines recede with increasing times.

Using the described model, the ablation depths can be compared to those from the Shirk experiment at different laser fluences. Figure 3.14 shows a plot of the single pulse ablation depth for fluences of 0.2, 1.0, 2.1, 4.2, 5.3, and 10.6 J/cm^2 in the model and 2.1, 4.2, 5.3 and 10.6 J/cm^2 in the experiment.

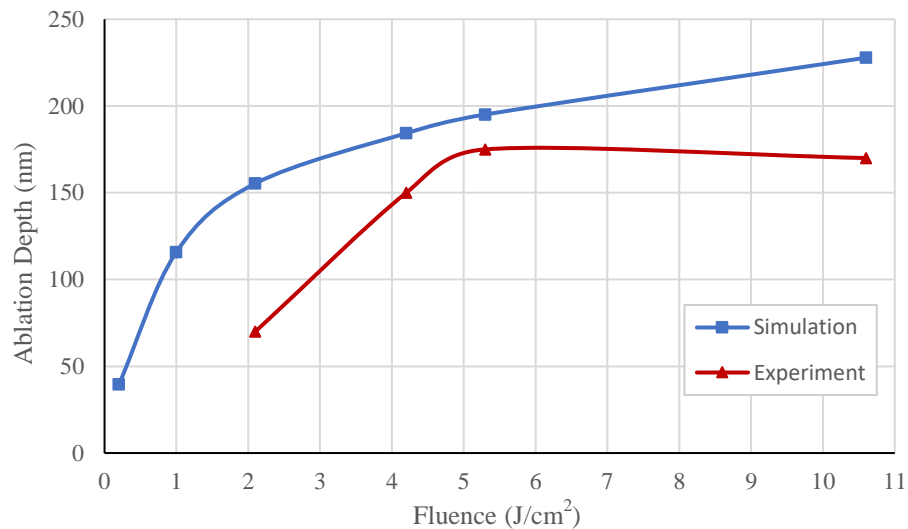


Figure 3.14 Single pulse ablation depth of HOPG for different fluences in simulation and experiment described by Shirk *et al.* [45].

Figure 3.14 shows that the simulation is in good agreement with the experiment at fluences of 4.2 and 5.3 J/cm² although following a slightly different trend line. In the experiment a linear increase is observed before reaching the saturation fluence of 5.3 J/cm² but in the simulation the somewhat linear increase is observed at lower fluences than the experiment before the slope decreases without completely saturating. The difference in trendlines at lower fluence could be attributed to different or competing ablation mechanisms in the experiment rather than just phase explosion in the model. As fluence increases phase explosion could be more pronounced leading to better agreement between the experiment and model. At higher fluences the model doesn't account for saturation fluence due to temperature dependent optical properties not being considered where extreme light intensities may lower absorption in the material.

Another important parameter concerning ultrashort laser ablation is the pulse width, as it has been shown that shorter pulse widths lead to more efficient material removal and that there is less time for heat to conduct further into the material resulting in minimal damage to underlying substrates. Shirk *et al.* [45] have demonstrated this by varying the pulse width on HOPG finding that single pulse ablation depth increases with decreasing pulse width. Figure 3.14 compares the results obtained by Shirk *et al.* [45] to results from the model.

Although the results from experiment show a pronounced increase in ablation depth with decreasing pulse width, the model is unable to simulate this process as different pulse widths lead to seemingly random ablation depths. All the ablation depths are within the same range of about 184 – 191 nm but don't show a defined trend. It is unknown as to what causes this error, but it could be an area for investigation in future work.

Moving on from single pulse ablation, multiple pulse ablation is the most likely method of laser machining to be used for device manufacturing as it enables precise machining depths and can be performed at high speeds. Shirk *et al.* [45] investigated the effect of multiple ultrashort pulses on HOPG for fluences of 2.1, 4.2 and 10.6 J/cm². Using the 1D TTM, 50 pulses were simulated for each fluence and compared to the experiment as shown in Figures 3.15, 3.16 and 3.17.

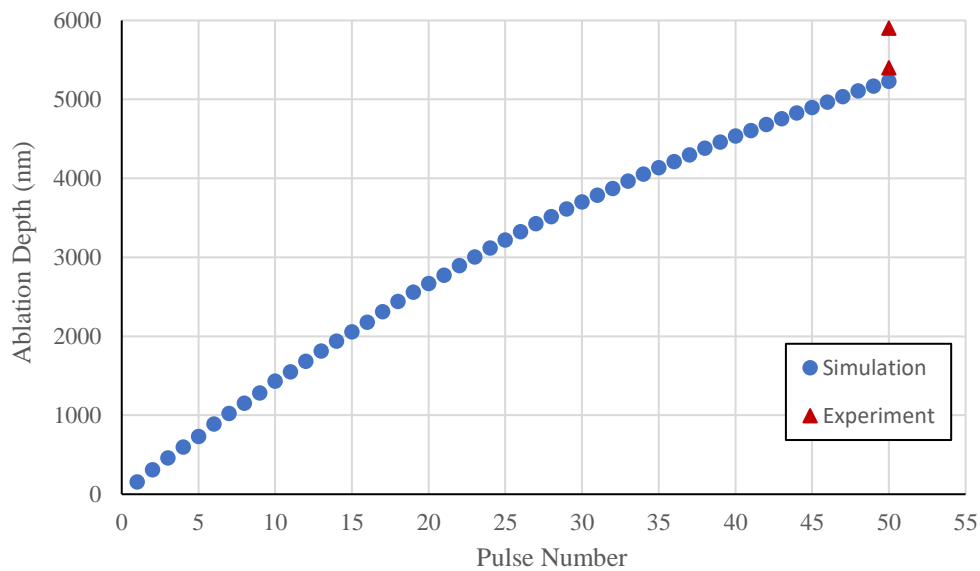


Figure 3.15 Multiple pulse ablation depth of HOPG at $2.1 J/cm^2$ for simulation and experiment.

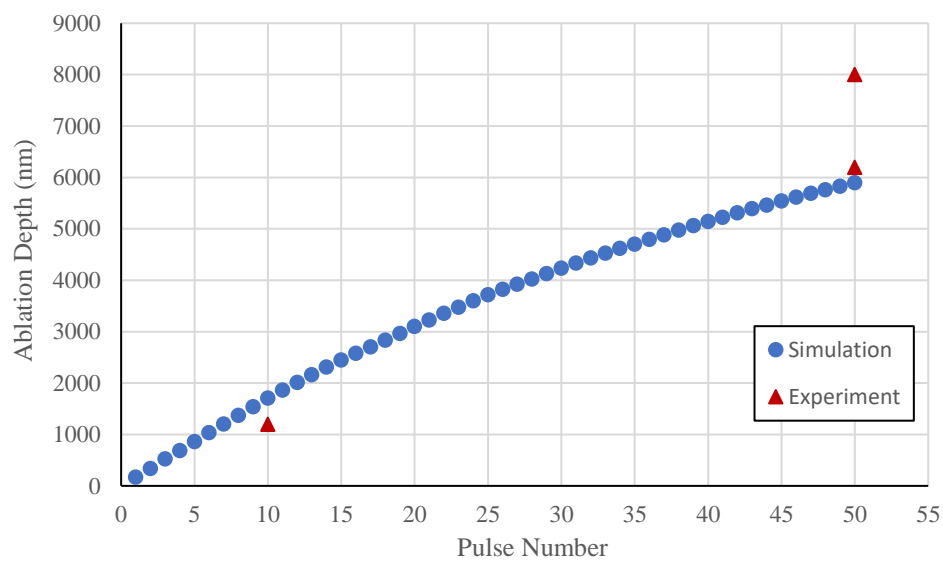


Figure 3.16 Multiple pulse ablation depth of HOPG at $4.2 J/cm^2$ for simulation and experiment.

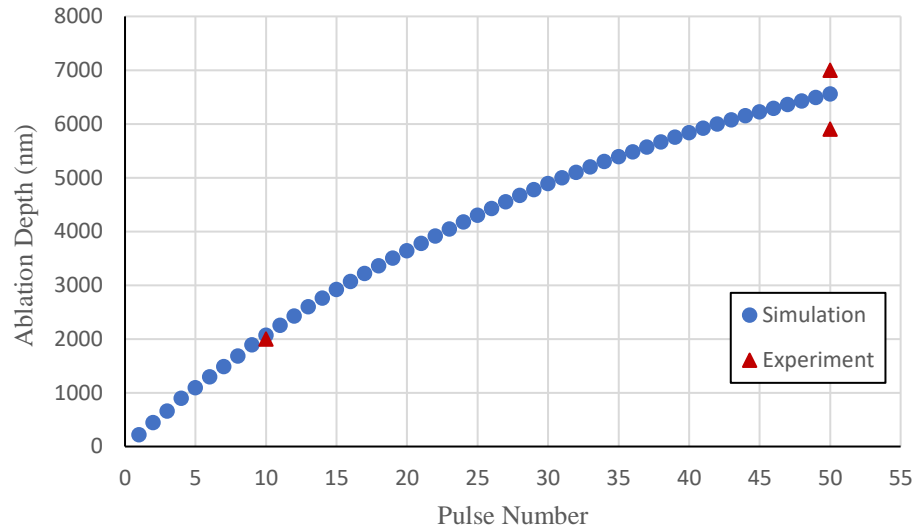


Figure 3.17 Multiple pulse ablation depth of HOPG at 10.6 J/cm^2 for simulation and experiment.

From Figures 3.15-3.17 it can be seen that all multiple pulse ablation simulations are in good agreement with the experiments by Shirk *et al.* [45] for each fluence. The simulated ablation shows that ablation depth per pulse decreases slightly with each successive pulse rather than showing a purely linear increase which would be expected since generally ablation depth tends to be the same for each successive pulse in an experiment. This may be due to the pulse being applied in a spatial reference frame rather than a geometrical reference frame. This causes the pulse energy applied to the material itself to decrease slightly with each successive pulse as material is removed. For fluences 2.1 and 4.2 J/cm^2 , the simulation overestimates the single pulse ablation depth, but from Figure 3.15 and 3.16, the ablation depth agrees well and matches the lower bound of experimental depth over 50 pulses. For 10.6 J/cm^2 , the simulated single pulse ablation depth overestimates the experiment, but over 50 pulses the ablation depth falls into experimental agreement very well. However, if the saturation fluence is not accounted for in the model, the 50 pulse ablation depth would likely be lower than experiment similar to fluences of 2.1 and 4.2 J/cm^2 .

All the simulated results discussed thus far have been modelled using the 1D TTM due to its ability to simulate single and multiple pulse ablation depth very quickly. The 2D TTM can be used to simulate the entire crater profile after a single pulse including the diameter of the ablated crater. Figure 3.18 illustrates the crater profile with the incident laser beam and highlights the 2D axisymmetric domain. Figure 3.19 shows a 2D plot of the ablated crater for a fluence of 4.2 J/cm^2 at the moment thermal equilibrium is achieved between electrons and the lattice signifying complete ablation.

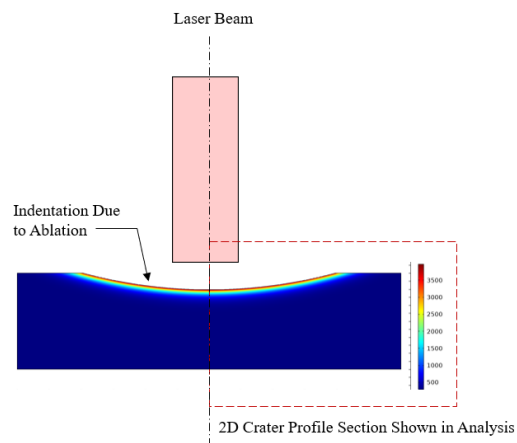


Figure 3.18 Illustration of the full cross-section crater profile with incident laser beam. The 2D axisymmetric domain is highlighted

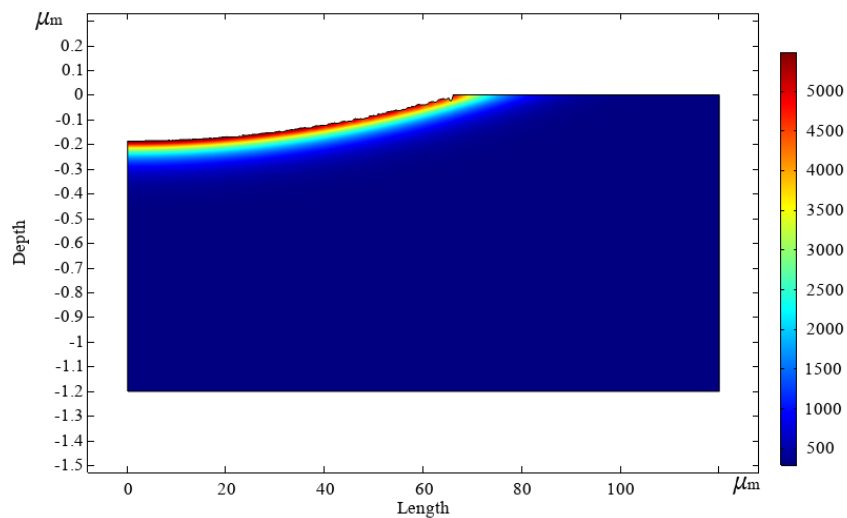


Figure 3.19 2D crater profile of HOPG after single pulse at 4.2 J/cm^2 .

The result from Figure 3.18 took approximately 2.5 hours to simulate which is much longer than the 1D simulations which take only a few minutes. The scale used in Figure 3.18 is 50:1 for length to depth in order to illustrate the depth of the crater. A radius of 80 μm can be seen which exceeds the beam spot radius of $\sim 50 \mu\text{m}$. Unfortunately, the results published in the experiment by Shirk *et al.* [45] do not examine the diameter of the ablated crater after a single pulse and instead show microscopic images of many pulses making it difficult to validate the model accuracy in predicting crater diameter. Figure 3.18 also helps to illustrate the very shallow heat diffusion characteristic of ultrashort laser irradiation as the material does not exceed room temperature after 0.4 μm into the material.

Overall, the FEA model developed in this section has proven to agree well at some fluences with ultrashort laser experiments on HOPG which has not been done in previous literature. The model successfully uses the electric properties of HOPG in the Wiedemann-Franz law to attain electronic thermal properties for a TTM in which energy coupling between the electrons and the lattice leads to material ablation. The model is able to simulate single and multi pulse ablation depths at different fluences and obtain a 2D ablation profile for single pulse laser irradiation.

3.7 Concluding Remarks

Chapter 3 presents the finite element model and simulation for the ultrashort laser ablation of HOPG based on the experiment by Shirk *et al.* [45]. First, the concept of FEM was introduced along with the COMSOL Multiphysics software package. The TTM along with the supporting equations for material properties were then described and combined with the HOPG material properties. Following the specifics relating to the model, the simulated results were presented where the results were found to be in good agreement with the experiment at some fluences for both single and multi pulse ablation with the best experimental agreement being achieved for a fluence of 5.3 J/cm^2 . A 2D plot of the ablated crater was also given for a fluence of 4.2 J/cm^2 . These results validate the TTM with an experiment for HOPG and allow the model to be applied to the ultrashort laser ablation of rGO in the next chapter.

Chapter 4 Finite Element Analysis of Ultrashort Laser Pulses Irradiating Graphene-Derivative Films

4.1 Reduced Graphene Oxide (rGO) Materials

The following section makes use of the TTM from Chapter 3 to study the ultrashort pulsed laser ablation of printed rGO. The simulation results are compared to experiment in order to validate the use of the model for predicting experimental results and identify potential limitations.

4.1.1 Laser Parameters and Reduced Graphene Oxide (rGO) Material Properties

The experiment to be examined was performed by Sinar *et al.* [74] where a 120 fs laser operating at 775 nm wavelength was used to micromachine rGO fabricated from graphite powder. The researchers were able to produce feature sizes of 2 – 3 μm in a single pass with an average laser power of 0.3 mW, beam diameter of $\sim 8 \mu\text{m}$, and feed rate of 100 mm/min without causing any significant damage to the underlying substrate. The developed model is able to simulate laser ablation of rGO for both single and multiple pulses.

Compared to the HOPG model where multiple pulses are irradiated onto the same spot of the material, in the Sinar experiment a scanning process is used to ablate a line across the material. This raises the problem where a 1D model can only simulate pulses in a single spot and a 2D model takes too long to compute several pulses scanned in a line. Therefore, an assumption is made using Equation 4.1 where multiple pulses scanned in a line can be approximated into an effective pulse number at a single point

$$N_{eff} = \sqrt{\frac{\pi}{2} \cdot \frac{f \omega_0}{v}} \quad (4.1)$$

where f is the pulse frequency and v is the scanning speed, allowing the 1D model to be used. Using this relation, either whole or partial pulses are added to the function $P(t)$ from Equation 3.12 with a time in between pulses depending on the pulse frequency. For the

following experiment, successive pulses are irradiated on the material after the system has completely cooled to room temperature. Since the laser power is constant at 0.3 mW, the pulse energy will change with a change in pulse frequency according to Equation 4.2.

$$E = \frac{P_{ave}}{f} \quad (4.2)$$

where E is the pulse energy, P_{ave} is the average laser power, and f is the pulse frequency.

The rGO model uses most of the same features as the HOPG model described in Section 3.3. The modelling equations are the same as those in the HOPG model which are Equations 3.10, 3.11, and 3.12. The modelling domain follows the depth of the sample used in the Sinar experiment with the sample cross-section being shown in Figure 4.1. The dark grey profile represents GO before annealing and the light grey profile represents rGO following the annealing of GO. Due to the significant roughness of the sample, a depth of 0.8 μm is assumed for the modelling domain.

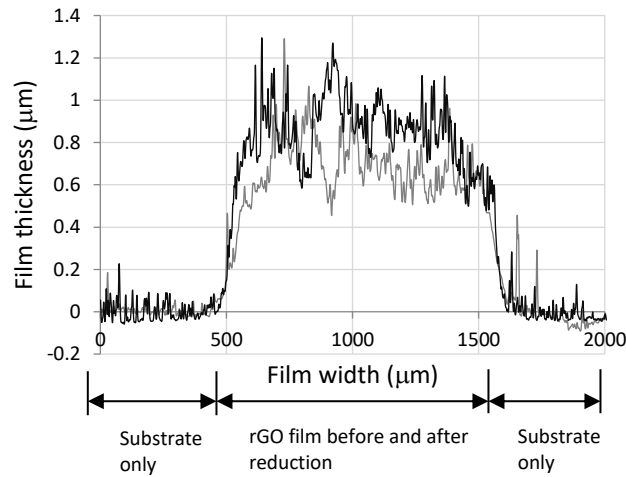


Figure 4.1 Typical surface roughness of printed rGO film [60].

In the Sinar experiment the GO thin films are incident upon a polyimide substrate which must be included in the model. Therefore, an additional domain is included underneath the 1.2 μm GO domain that is also 1.2 μm and uses the thermal properties of polyimide from

the COMSOL material database. Optical properties for polyimide are not considered since the laser light does not penetrate past the rGO domain. Electron thermal properties are also not considered since polyimide is an electrical insulator with an extremely low electrical conductivity and it is assumed that no electron conduction exists past the rGO domain.

The optical properties for rGO are obtained from experiments from Schmiedova *et al.* [39] where the reflectivity and linear absorption coefficient are calculated using Equation 2.5 and 2.7 from the complex refractive index and extinction coefficient for rGO. At 775 nm the refractive index and extinction coefficient were found to be approximately 2.025 and 0.225 respectively giving a reflectivity of 0.12 and linear absorption coefficient of 3.5×10^6 1/m.

The electron specific heat capacity and electron thermal conductivity are obtained from Equations 3.8 and 3.9 using sheet resistance measurements from rGO samples in the experiment by Sinar *et al.* [74]. The sheet resistance values from the experiment are given for the ab-plane but not the c-axis. Thus, the same value is assumed for both directions since c-axis electrical properties for printed rGO could not be found from literature. Although the c-axis sheet resistance would likely be much higher, the assumption is considered valid since the electron thermal properties have little impact on the overall material ablation since the thermal properties of graphene are dominated by the phonons which dictate the ablation temperature. Plots for the electron specific heat capacity and electron thermal conductivity of printed rGO are given in Figures 4.2 and 4.3.

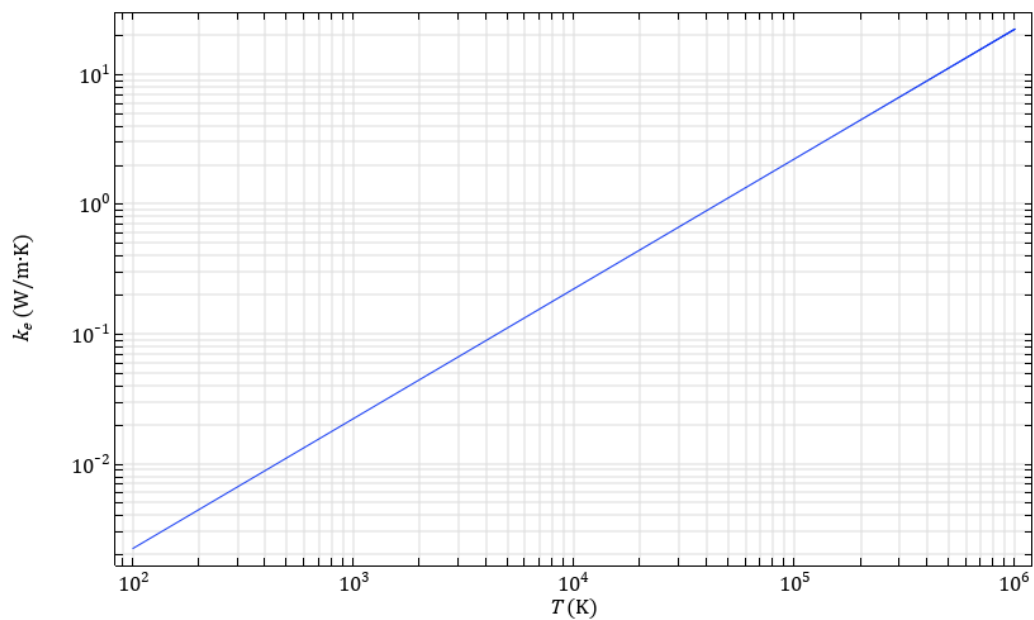


Figure 4.2 Temperature dependent electron thermal conductivity for printed rGO.

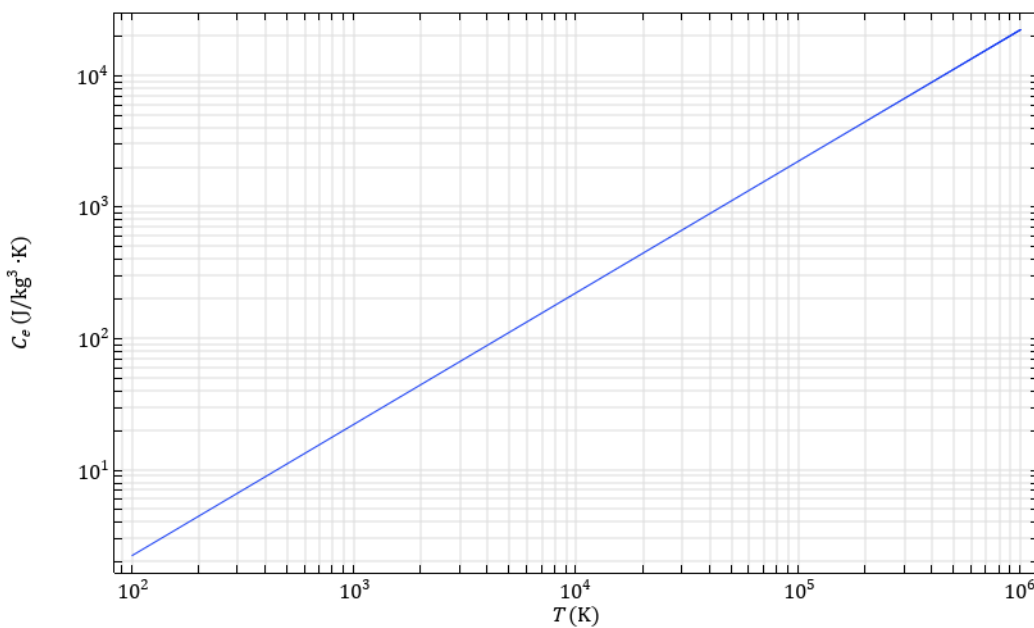


Figure 4.3 Temperature dependent electron specific heat capacity for printed rGO.

The electron-phonon coupling parameter, G_{ep} , is assumed to be the same as HOPG as a limited amount of literature exists concerning the electron-phonon coupling parameter

for rGO under ultrashort laser irradiation. High temperature thermal properties for GO/rGO are also limited in literature so those of graphite are assumed. One major distinction between printed rGO and HOPG lies in the density, where printed rGO has much lower density than that of HOPG due to the disordered stacking of flakes that make up the film, and so a density of 0.85 g/cm^3 is obtained from averaging the density of samples of conductive printed rGO developed by Xie *et al.* [75]. The laser parameters for the experiment by Sinar *et al.* [74] are given in Table 4.1.

Table 4.1 Laser parameters of Sinar experiment [74].

Parameter (Symbol, Unit)	Value
Pulse width (τ_p , fs)	120 [74]
Wavelength (λ , nm)	775 [74]
Pulse energy (E, μJ)	0.3 – 1.2 [74]
Beam diameter (d , μm)	8 [74]

The solver settings and time stepping used in the rGO model are identical to those used in the HOPG model. The 1D mesh also uses the same number and type of elements, but under the 2D model, the radial element numbers are different due to the much smaller beam diameter than the HOPG experiment. For this case, 150 elements are used in the radial direction. The boundary conditions are the same with an added condition that there is no electron thermal conduction in the substrate. The model assumptions are also the same as those from Section 3.6.4 with an added assumption that there is no thermal contact resistance between the substrate and thin film.

4.1.2 rGO Simulation Results

Unlike the Shirk experiment, the Sinar experiment does not specify the ablation depth for each pulse but instead specifies successful ablation as the complete removal of rGO without damage to the underlying substrate. This was achieved with a laser power of 0.3 mW, a scan speed of 100 mm/min and a pulse frequency of 1 kHz or less that was not specifically

stated. Using Equation 4.1 and pulse frequencies of 250, 500, 750 and 1000 Hz, effective pulse numbers of 0.97, 1.37, 1.68, and 1.94 are determined respectively. Since the laser power is constant at 0.3 mW, the pulse energy for each pulse frequency follows Equation 4.2 and the parameters for the simulation are listed in Table 4.2. Figure 4.4 shows the electron and lattice temperature at the surface of the film over time for a pulse energy of 1.2 μJ and effective pulse number of 0.97.

Table 4.2 Derived laser parameters for rGO simulation.

Pulse Frequency (Hz)	Effective Pulse Number	Pulse Energy (μJ)
250	0.97	1.2
500	1.37	0.6
750	1.68	0.4
1000	1.94	0.3

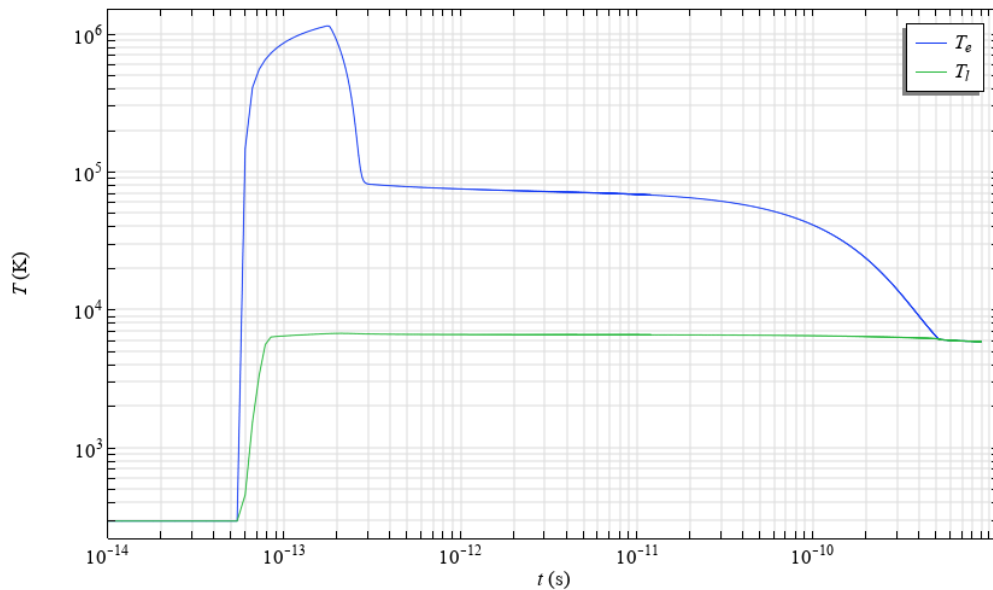


Figure 4.4 Electron and lattice temperatures at surface of printed rGO for 1.2 μJ pulse energy and effective pulse number of 0.97.

The simulations show that the electron temperature peaks at $\sim 1.18 \times 10^6$ K after 180 fs before reaching thermal equilibrium with the lattice after 515 ps which is a very similar trend to the HOPG simulations. One difference compared to HOPG is that thermal equilibrium takes approximately 5 times longer to occur even though the electron-phonon coupling constant is the same. This is likely due to the lower density of the rGO film that lowers the lattice heat capacity leading to a slower energy exchange. The ablation depth predicted by the simulation is $0.75 \mu\text{m}$ which is very close to the assumed film depth of $0.8 \mu\text{m}$ and is considered to be in good agreement with the experiment. Unlike the HOPG simulation, a substrate is used in the Sinar experiment and plots of temperature over material depth can be used to determine substrate damage. Figures 4.5 and 4.6 show plots of the electron temperature and lattice temperature over the material depth respectively.

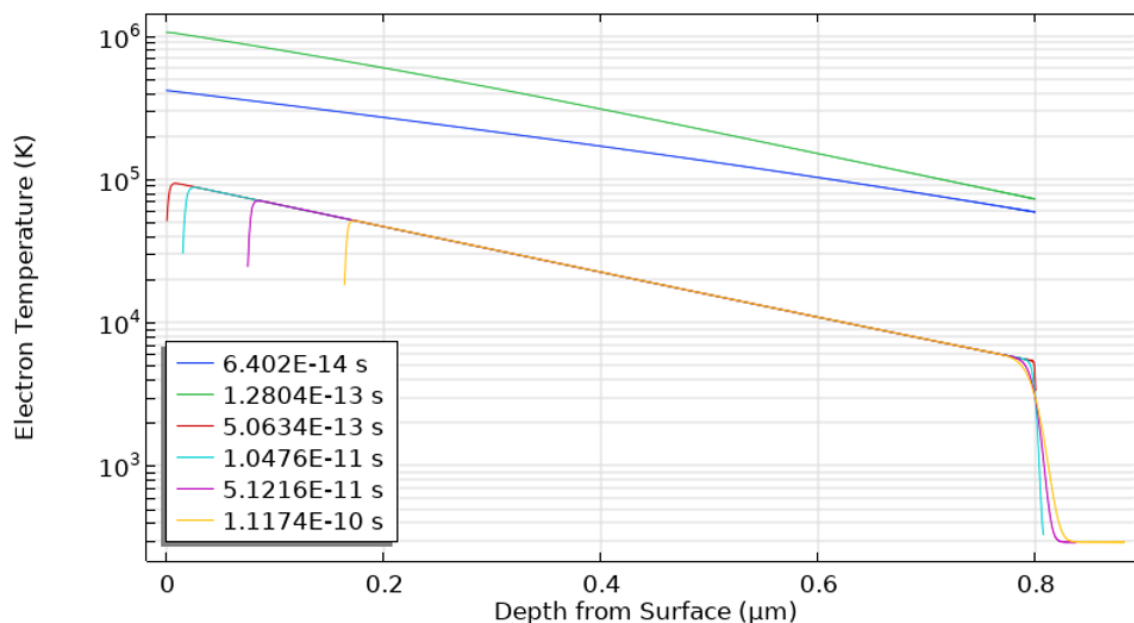


Figure 4.5 Electron temperatures with respect to depth at different times during simulation.

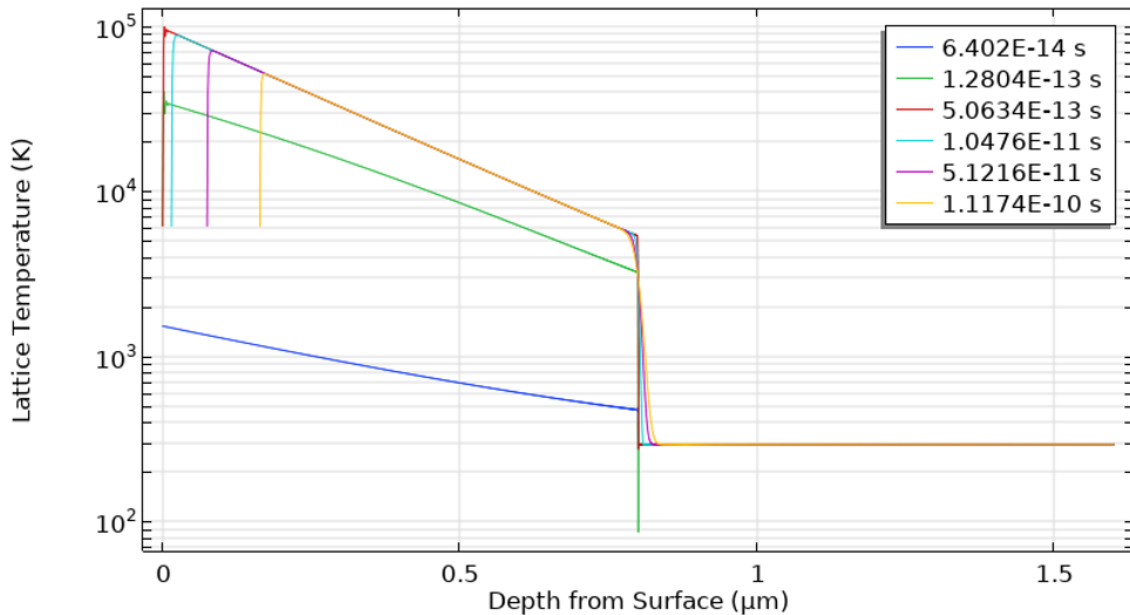


Figure 4.6 Lattice temperatures with respect to depth at different times during simulations.

From Figure 4.5, the electron temperature can be seen reducing drastically at the substrate boundary of $0.8 \mu\text{m}$ though not completely reaching room temperature like it should in theory by having an electron thermal conductivity of zero. This may be due to the model being unable to completely simulate such a large temperature gradient and instead approximates it over a small distance. From Figure 4.6, the material ablation can be seen as the plot lines recede into the material. At the substrate boundary, a similar trend is observed to the electron temperature however this is expected for the lattice temperature since the polyimide substrate has thermal properties that allow heat conduction to cross the substrate boundary. The green plot line representing 128 fs and the near peak electron temperature in Figure 4.5 can be seen decreasing below room temperature at the substrate boundary signifying that the model has trouble simulating such a large temperature gradient and overpredicts the amount of temperature reduction. Although the model demonstrates some error near the substrate boundary and may not accurately predict the temperature or substrate damage, the results can still be used to compare substrate materials by analyzing how far the lattice temperature penetrates unto the substrate.

A 2D plot of the ablated crater profile is shown in Figure 4.7 at the time of thermal equilibrium between the electrons and lattice. A depth to length scale of 6:1 is used to better illustrate the ablation profile. It can be seen that the crater radius does not exceed $4\ \mu\text{m}$ even though the focused beam radius used in the experiment is $4\ \mu\text{m}$. This is due to the Gaussian distribution of the laser intensity profile. At higher fluences the crater diameter will increase.

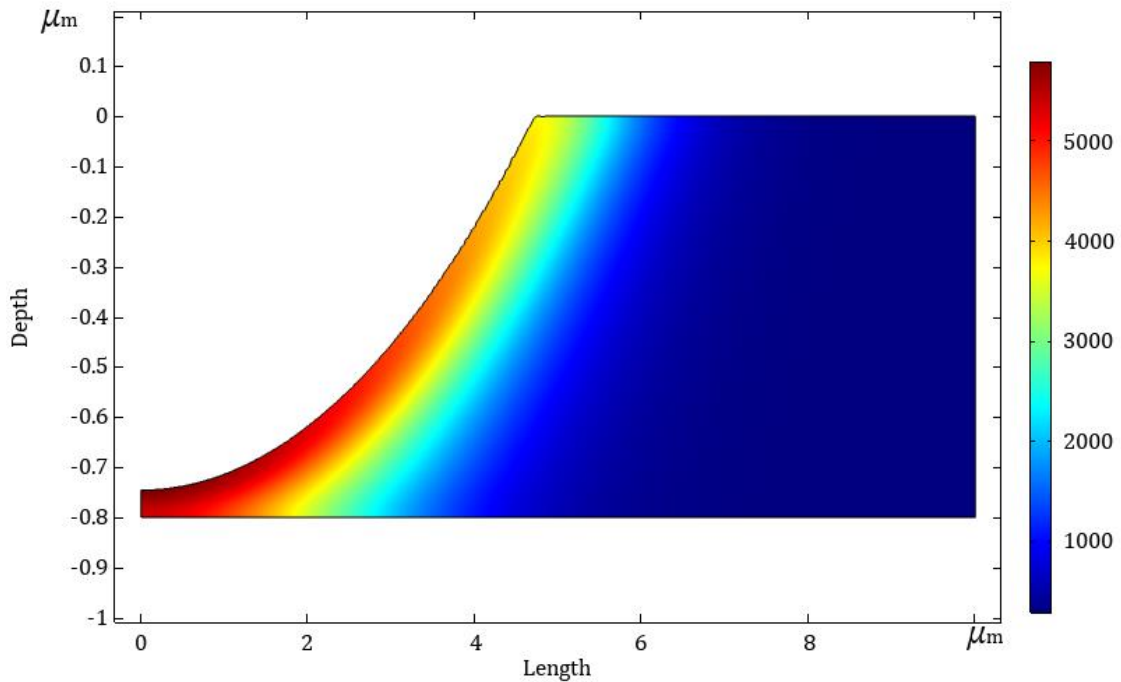


Figure 4.7 Simulated 2D crater profile after laser irradiation. 6:1 depth to length ratio.

The validity of Equation 4.1 can be examined using the parameters outlined in Table 4.2 for changes in pulse frequency and thus pulse energy due to constant laser power. Although the pulses are decimals they can be approximated by multiplying the energy of one of the pulses by the decimal factor instead of changing the length of the pulse. Results for ablation depth with effective pulse number are displayed in Figure 4.8.

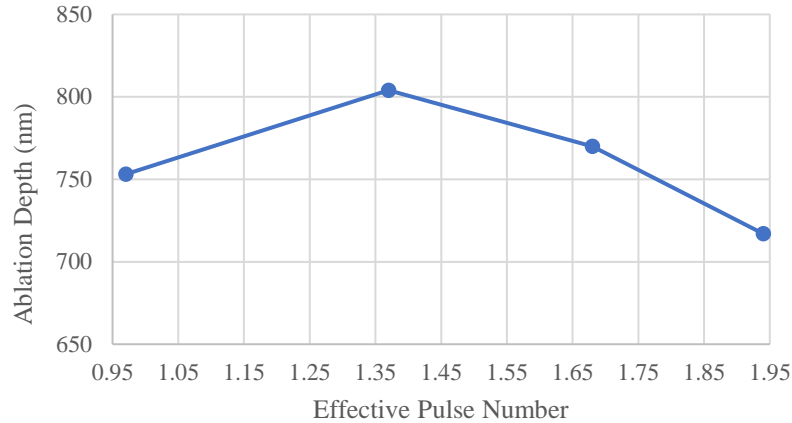


Figure 4.8 Ablation depth with respect to effective pulse number for 250, 500, 750 and 1000 Hz pulse repetition rate.

For effective pulse numbers corresponding to laser frequencies of 250, 500, 750 and 1000 Hz the ablation depth is consistent with a spread of 87 nm between maximum and minimum ablation depths. This proves that Equation 4.1 can be a valid assumption when analyzing the effect of pulse frequency and scan speed on ablation depth using a 1D model.

4.2 Single Layer Graphene (SLG)

The present section investigates the applicability of the TTM to be used on ultrashort pulsed laser irradiation of SLG where SLG represents the upper limit of material properties in which the reduction of GO aims to achieve. A multitemperature model (MTM) is proposed from previous literature and compared to the TTM to determine which is more suitable in predicting ablation. The fluence threshold for SLG using both models are determined.

4.2.1 Multi-temperature Model (MTM)

The TTM has been well-established and widely used to model ultrafast light interactions of metals with sufficient accuracy. However, the TTM assumes that the phonon polarizations are in thermal equilibrium where only a single electron-phonon coupling parameter is used (see Section 2.6). Although this assumption is valid for most materials, Vallabhaneni *et al.* confirmed that the phonon branches of SLG are far enough out of

equilibrium due to selective coupling of phonon branches that a TTM can produce inaccurate results [51]. Lu *et al.* expanded on these results by developing a multi-temperatures model (MTM) that uses a separate electron-phonon coupling parameter and simulates a separate temperature for each phonon branch [76]. They found that a typical TTM can significantly underestimate the electron and lattice temperature of SLG as well as its thermal conductivity and electron relaxation time. The model was tested by simulating a CW laser to achieve steady state and a 50 fs pulsed laser irradiating suspended SLG. However, these studies were restricted to cases with relatively low temperatures that were slightly above room temperature. In the study reported in this thesis, the MTM will be tested by simulating an experiment by Roberts *et al.* [52] where a laser is irradiated on SLG at different pulse widths to determine the fluence threshold required for ablation. Although the properties for each phonon branch provided in the reference paper are room temperature values, the MTM can still be utilized by FEA to understand the ultrafast laser ablation of SLG. Furthermore, it can also be tested on rGO and HOPG.

The MTM proposed by Lu *et al.* follows Equation 4.1 and 4.2

$$C_e \frac{\partial T_e}{\partial t} - \nabla k_e \nabla T_e = Q(r, z, t) - \Sigma G_{ep,i} (T_e - T_{p,i}) \quad (4.1)$$

$$C_{p,i} \frac{\partial T_{p,i}}{\partial t} - \nabla k_{p,i} \nabla T_{p,i} = \Sigma G_{ep,i} (T_e - T_{p,i}) + G_{pp,i} (T_{lat} - T_{p,i}) \quad (4.2)$$

where $G_{ep,i}$ is the electron-phonon coupling parameter for the respective phonon branch, $T_{p,i}$ is the temperature of the respective phonon branch, $C_{p,i}$ is the volumetric heat capacity for the respective phonon branch, and $G_{pp,i}$ is the phonon coupling parameter between the respective phonon branch and a scattering lattice reservoir. In the MTM, the relaxation time approximation (RTA) is used where rather than each phonon branch coupling with each other and being computationally expensive, each phonon branch couples with a common thermal lattice reservoir whose temperature is represented by T_{lat} . An additional equation is needed to solve for T_{lat} and ensure that energy is conserved between phonon branches which is given by

$$\Sigma G_{pp,i} (T_{lat} - T_{p,i}) = 0 \quad (4.3)$$

It can also be noted that the sum of the electron-phonon coupling parameters for each branch equates to the electron-phonon coupling parameter used in the TTM.

$$\Sigma G_{ep,i} = G_{ep} \quad (4.4)$$

4.2.2 SLG Modelling Domain

Since the present experiment concerns the laser irradiation of SLG which is only one atom thick, the modelling domain can be 2D axisymmetric with no mesh distribution in the z-direction since ablation depth won't be simulated for SLG. This allows for the width of the ablated area to be simulated with very low computational cost. The domain length for the Lu model is 5 μm using a laser spot radius of 0.5 μm and the domain length for the Roberts experiment is 30 μm using a laser spot radius of 10 to 15 μm . Both domains have a depth of 0.335 nm to represent the thickness of SLG. The modelling domain for the Roberts experiment is shown in Figure 4.9 with a 2500:1 depth to length scale.

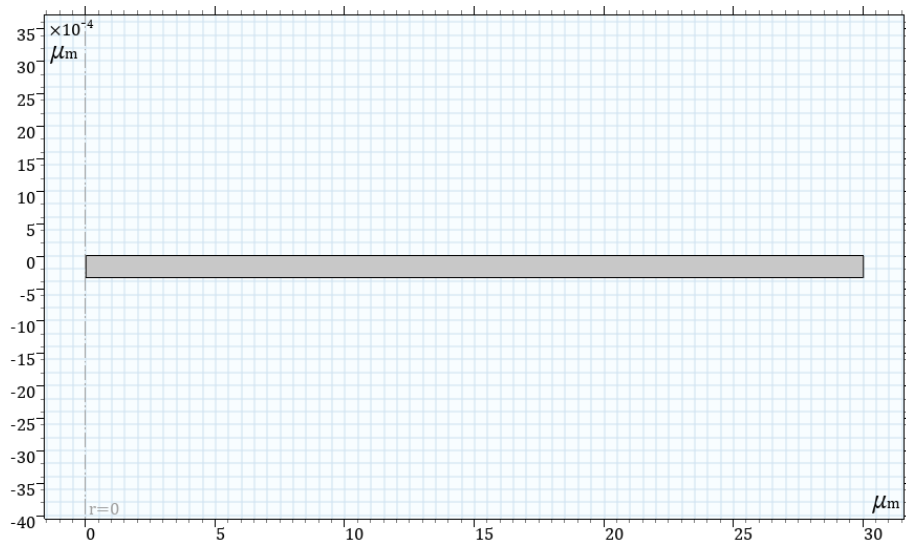


Figure 4.9 Modelling domain for SLG with 2500:1 depth to length ratio.

4.2.3 Material Properties of SLG and Laser Parameters

The room temperature properties for each phonon branch are reported in the paper by Lu *et al.* and are outlined in Table 4.3. The six phonon modes of graphene can be characterized as the longitudinal acoustic (LA), transverse acoustic (TA), out-of-plane acoustic (ZA), longitudinal optical (LO), transverse optical (TO), and out-of-plane optical (ZO).

Table 4.3 Phonon branch properties for SLG [76].

Property (Units)	LA	TA	ZA	LO	TO	ZO
G_{ep} (10^{16} W/m · K)	0.01	0.0001	0	0.06	0.27	0
G_{pp} (10^{16} W/m · K)	0.27	1.30	0.19	0.27	0.14	0.04
C_p (10^6 J/m ³ · K)	0.19	0.32	0.61	0.03	0.02	0.16
k_p (W/m · K)	92.6	237.9	2780.0	10.0	10.0	20.9

For the Lu model, the source equation is provided in the paper which accounts for the pulse energy as well as the reflectivity of SLG. The room temperature electron thermal conductivity was given to be 50 W/m · K and the electron heat capacity was given as 360 J/m³ · K. For the simulation of the Roberts experiment the same properties are used from Table 4.3, but the source equation follows Equation 3.10 and 3.12 where the reflectivity, linear absorption coefficient and laser parameters must be input. The laser parameters and optical properties used in the Roberts model are outlined in Table 4.4.

Table 4.4 Laser parameters from Roberts' experiment [52].

Parameter (Symbol, Unit)	Value
Pulse width (τ_p , fs)	50
Wavelength (λ , nm)	790
Pulse energy (E, μ J)	0.47
Beam diameter (d , μ m)	20
Absorbance (A, 1)	0.023
Absorption Coefficient (α , 1/m)	1.58×10^8

Since graphene is transparent the absorbance is used rather than reflectivity in this case where a single layer of graphene has been determined to absorb approximately 2.3% of incident white light [36]. Due to graphene being a thin film, the absorption coefficient was then calculated using

$$\alpha = \frac{2.303A}{t_s} \quad (4.5)$$

where t_s is the thickness of SLG. In order to compare the MTM to a TTM, the lattice heat capacity and thermal conductivity must be known for SLG. The lattice heat capacity and thermal conductivity were found to be 700 J/kg · K and 1170 W/m · K respectively. The electron-phonon coupling parameter was determined to be 0.34×10^{16} W/m³ · K based on Equation 4.4.

4.2.4 Simulation Study of Irradiating SLG

In the MTM equations described above, the modelling domain and material properties of SLG are combined to simulate the experiment by Roberts *et al.* that determines the fluence threshold for SLG. Using the laser parameters from Roberts *et al.* the lattice temperature and ablation radius are simulated and compared for the MTM and the TTM.

4.2.4.1 Boundary and Initial Conditions

The MTM was implemented into COMSOL using the Coefficient Form PDE interface where the MTM equations were entered manually. Eight dependent variables are solved for which are the electron temperature, T_e , the 6 phonon temperatures, $T_{p,i}$, and the scattering lattice reservoir temperature, T_{lat} . Following the domain diagram of Figure 3.5, the model has a zero flux (thermal insulation) boundary condition on edges 2, 3 and 4, an initial temperature of 293.15 K for all dependent temperature variables, and a heat source applied to the entire domain according to Equation 3.10. Since the model simulates SLG and no ablation depth occurs, the boundary conditions for ablative heat flux and mesh velocity are not included. Instead, the weighted average of the phonon temperatures is plotted where it can be observed if the ablation temperature of $0.9 \cdot T_c$ is exceeded representing ablation. In the paper by Lu *et al.* it is believed that the apparent scattering lattice reservoir temperature does not properly represent the lattice temperature that would be measured in experiment and that the weighted average of the phonon temperatures should be given by

$$T_p = \frac{\sum C_{p,i} T_{p,i}}{\sum C_{p,i}} \quad (4.6)$$

where T_p is the apparent lattice temperature.

4.2.4.2 Meshing Parameters

With the domain being SLG and no ablation being modelled, a mesh only needs to exist in the radial direction to simulate the temperature distribution. A fixed mesh distribution of 150 elements is selected. Figure 4.10 shows the meshed geometry.

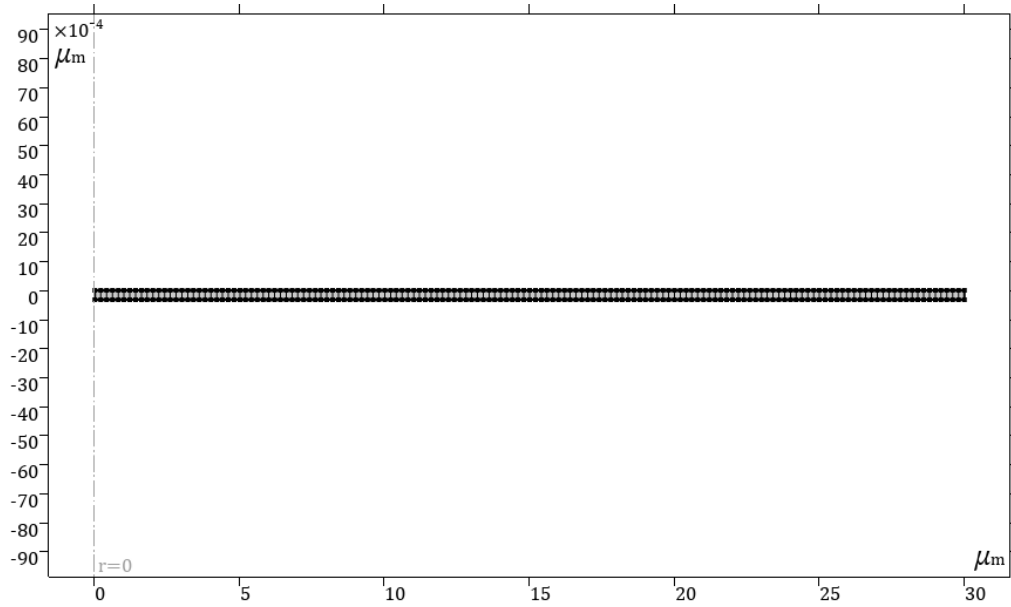


Figure 4.10 Meshing for SLG domain with 50 elements.

4.2.4.3 Solver and Assumptions

Unlike the previous models, the default solver settings are sufficient to converge on a solution with only the initial timestep being changed to 1 fs. For the time-dependent solver, an initial timestep range of 1 ps is chosen with 1 fs timesteps followed by a time step range of 1200 ps with 500 fs timesteps. The assumptions for the model are similar to the previous models with radiation and convection assumed to be negligible, the temperature distribution being symmetric about the z-axis to use a 2D axisymmetric domain, surface roughness assumed to be negligible, and the optical properties to be constant with temperature. An additional assumption is that all phonon, electron, and lattice properties are their values at room temperature since temperature dependent phonon properties are not provided. This likely leads to much different temperatures than would be experienced in experiment, but for the sake of comparison with a TTM the assumption holds.

4.2.4.4 MTM and TTM Simulation Results on SLG

The resultant MTM was simulated using the phonon properties from Table 4.3 and the laser and optical parameters from Table 4.4. A TTM was also used to compare to the MTM by using the averaged lattice properties of SLG and the laser parameters from Table 4.4. Figure

4.11 shows the electron temperature, phonon branch temperatures, and scattering lattice reservoir temperature over time.

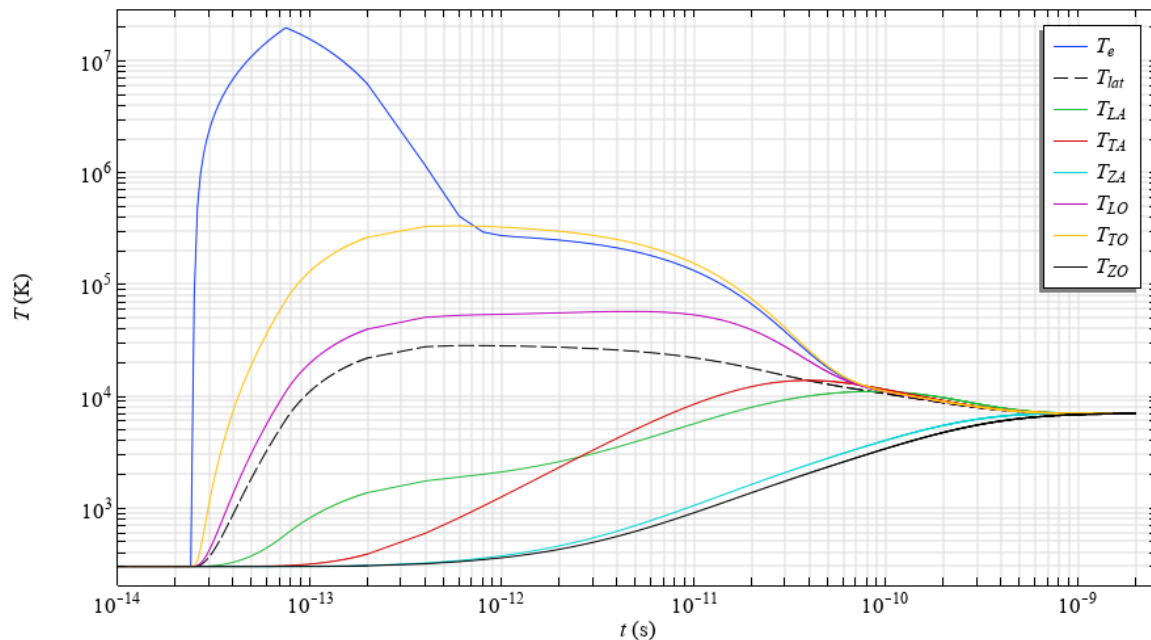


Figure 4.11 Phonon branch resolved temperature plot for laser irradiation of SLG.

It can be seen that the electrons reach a temperature of approximately 1.95×10^7 K and that the phonon branches are considerably out of equilibrium with the highest phonon temperature being several orders of magnitude larger than the smallest before equilibrium is reached. The temperature of the scattering lattice reservoir, T_{lat} , representing the average phonon temperature reaches a maximum of $\sim 28,000$ K before equilibrium is reached at approximately 7000 K. The weighted average of the phonon temperature, T_p , according to Equation 4.6 is plotted as part of Figure 4.12 where it reaches a temperature of ~ 6900 K which is much closer to the critical temperature of graphite. Equilibrium between the electrons and lattice is reached after ~ 1 ns.

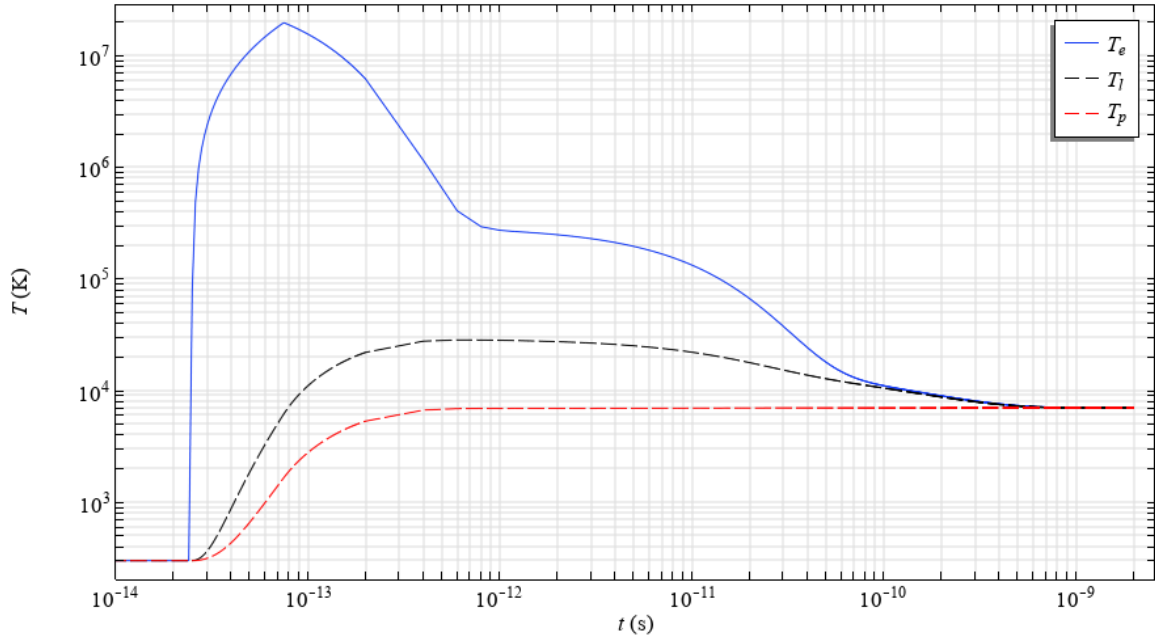


Figure 4.12 Temperature plot comparing the thermal lattice reservoir temperature and weighted average phonon temperature for SLG irradiation.

From Figure 4.12, it can be concluded that the weighted average lattice temperature is in relatively good agreement with the experiment especially considering the use of room temperature parameters where temperature dependent parameters could bring the lattice temperature closer to the critical temperature in accordance with phase explosion as the ablation mechanism. The MTM can be compared to a TTM as mentioned and is shown in Figure 4.13.

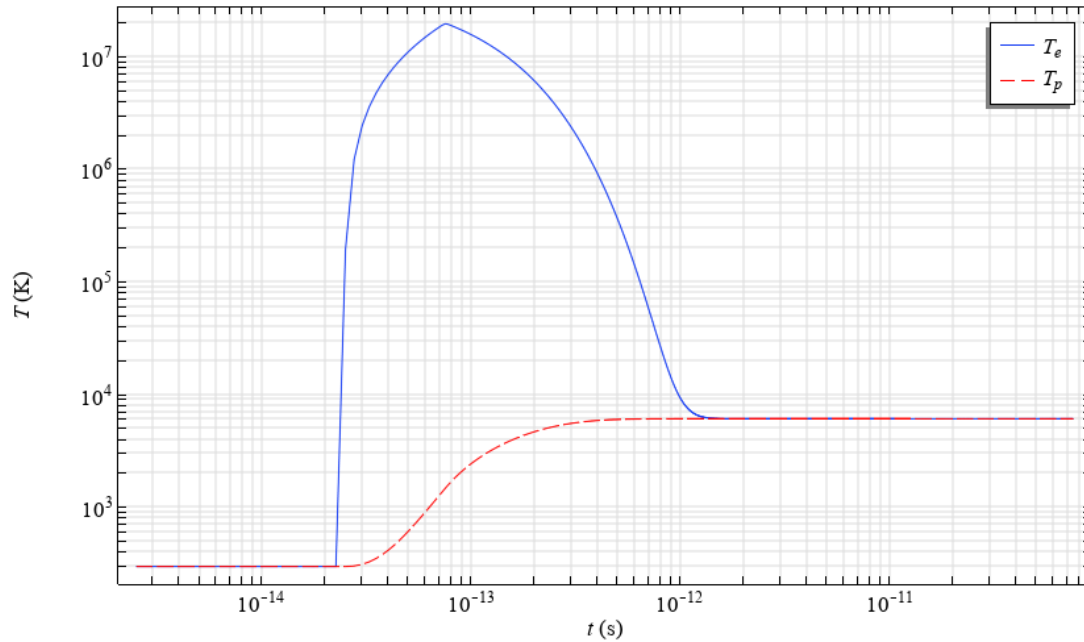


Figure 4.13 Temperature plot for TTM of SLG irradiation.

Comparing the two plots, it is evident that the TTM has a lower peak electron and lattice temperature of 1.14×10^6 K and 7180 K respectively even though the same electron material properties were used. This signifies that the lower electron temperature may be due to the absence of coupling for different phonon branches and instead couples much quicker with the averaged phonons in the TTM. The TTM plot also shows that the electrons and lattice reach equilibrium after 1.5 ps which is much faster than the 1 ns experienced in the MTM. The different lattice properties may also be responsible for the differences experienced in the model where the TTM properties are obtained from an experiment and the MTM properties are calculated through molecular dynamics simulations. When considering the fluence threshold for ablation, the TTM fluence threshold was found to be 0.1 J/cm^2 and the MTM fluence threshold was found to be 0.09 J/cm^2 . Compared to the experimental fluence threshold of 0.15 J/cm^2 , both models predict lower values, but the TTM value is slightly closer.

In the Roberts experiment, images of the ablated SLG were collected and can be compared to the MTM and TTM ablation radius. In Figure 4.14, the 2D temperature profile of the weighted average lattice is plotted for a laser spot diameter of 20 μm after

equilibrium is achieved. It is shown that the SLG completely diffuses to room temperature at a radius of $\sim 20 \mu\text{m}$. Figure 4.15 shows the 2D temperature profile of the lattice in the TTM after equilibrium where it is shown that the lattice is at room temperature at a radius of $\sim 13 \mu\text{m}$. From the Roberts experiment [52], the ablated diameter for a 50 fs pulse was found to be $\sim 15 \mu\text{m}$ which is best agreement with the MTM where the diameter is $\sim 14 \mu\text{m}$ shown in Figure 4.14. The ablation diameter is compared to the experiment by noting the point along the SLG length where a temperature of $0.9 \cdot T_c = 5000 \text{ K}$ is met.

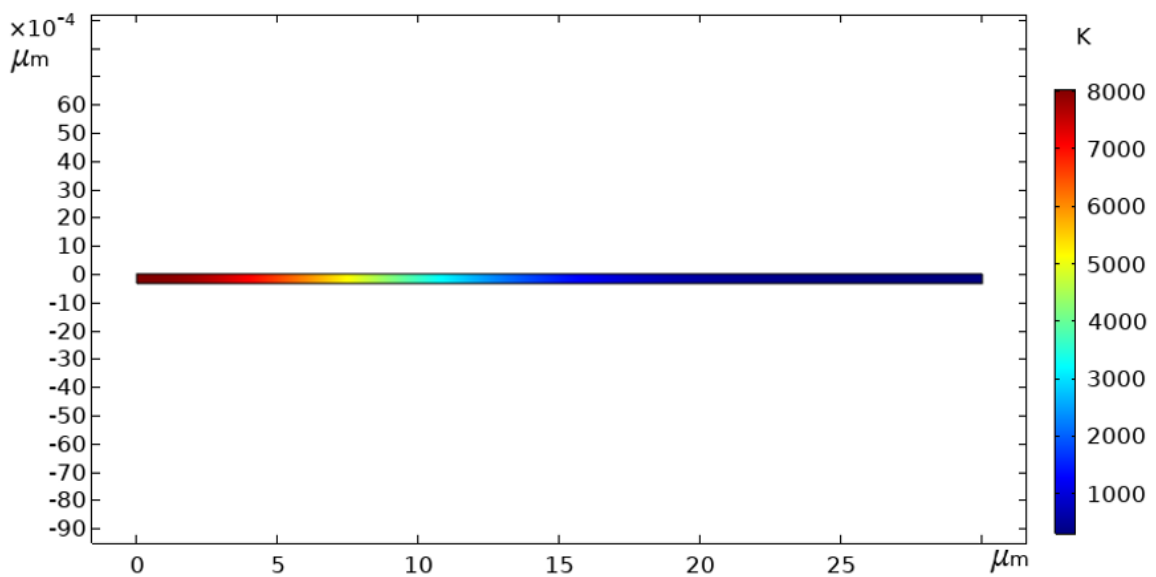


Figure 4.14 MTM weighted phonon average temperature plot at the point of equilibrium.

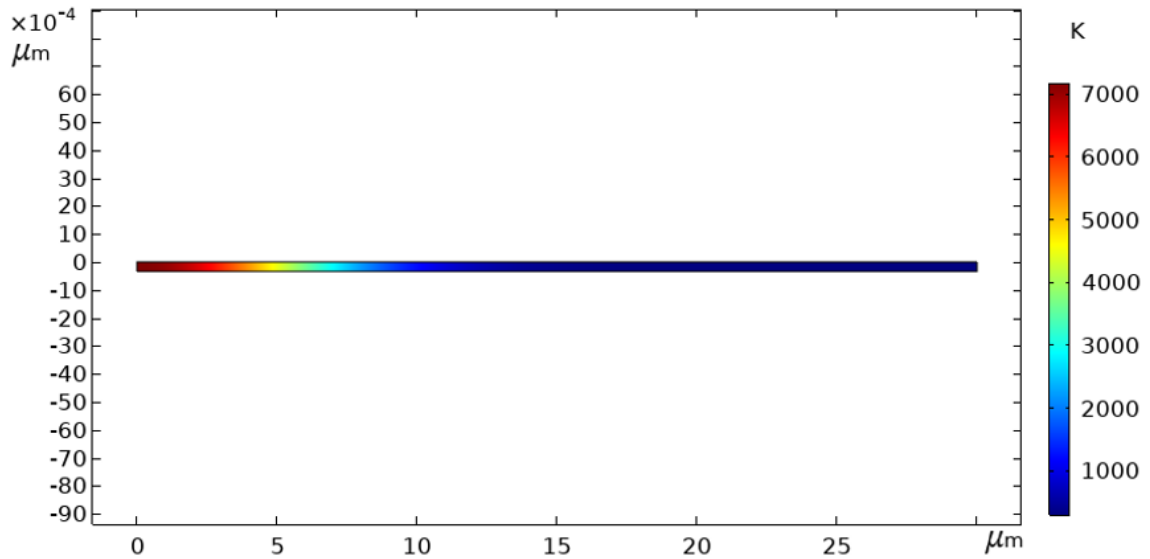


Figure 4.15 TTM lattice temperature at the point of equilibrium.

4.3 Concluding Remarks

Chapter 4 applied the TTM used in Chapter 3 to ultrashort laser ablation of printed rGO and extended the TTM to the MTM to simulate ultrashort laser ablation of SLG. For printed rGO, the simulation approximated multiple scanned pulses from experiment to multiple pulses in a single spot where it was found that the simulation is in good agreement with the experiment. Using the MTM, ablation of SLG was simulated using room temperature properties. Comparing the lattice temperatures from the TTM and MTM for the fluence threshold of SLG, the TTM is found to be in better agreement, but when comparing the ablated diameters, the MTM is found to be in better agreement. It is predicted that the MTM simulations will be in better agreement with experiments once the high temperature phonon properties of SLG are determined, but this is outside the scope of this thesis. At present, neither the MTM nor TTM are able to accurately predict the ablation of SLG proving that the TTM is much better suited for the pulsed laser ablation of HOPG and rGO.

Chapter 5 Impact of Laser Parameters on Annealing, Ablation and Substrate

5.1 Introduction

The previous chapters introduced the developed FEA TTMs for both HOPG and printed rGO films proving that the ablation depth due to ultrashort laser pulses agrees well with experimental results for both single and multi pulse processes. The following chapter extends the developed TTM into parametric studies that investigate the impact of different laser parameters on the annealing and ablation quality of printed rGO films. More specifically, it investigates the effect of the laser wavelength for efficient thermal processing, determines substrate damage for different materials, and provides an optimization study to determine the ideal fluence for efficient annealing and micromachining of printed rGO film.

5.2 Laser Wavelength Analysis

The purpose of this section is to investigate the relationship between the wavelength of incident laser light and fluence to give insight into parameters for the efficient ablation of HOPG and rGO thin films since, at present, there is limited research regarding this relationship.

The most significant parameters influencing ablation depth for HOPG at different wavelengths are the material's reflectivity and optical penetration depth. These parameters have been calculated for HOPG from the complex refractive index given by Song *et al.* [38] and were shown in Figure 2.10. It is understood that lower reflectivity results in more efficient energy transfer from the laser to the material due to higher absorption and that greater ablation depths should be achieved. It is also known that a smaller optical penetration depth produces a smaller HAZ and the fluence threshold for ablation should be lower due to a greater concentration of energy. This suggests that, based off reflectivity, the most efficient range of wavelengths for ablation should be 400 to 600 nm. Based off optical penetration depth, the most efficient wavelength range should be in the infrared

regime due to energy propagating the furthest into the material. Using the material properties of HOPG from Table 3.1, the optical properties from Figure 2.10, and a laser with a fluence of 5.2 J/cm^2 , the ablation depth is simulated for wavelengths ranging from 200 to 1600 nm and is shown in Figure 5.1.

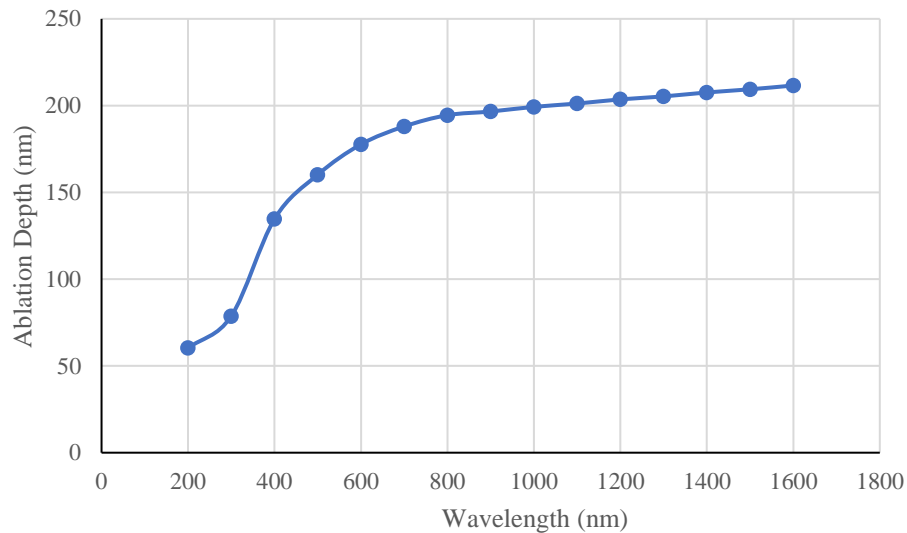


Figure 5.1 Single pulse ablation depth of HOPG at 5.2 J/cm^2 for different wavelengths.

As shown in Figure 5.1, the ablation depth increases with laser wavelength until it reaches a maximum of 211 nm at a wavelength of 1600 nm. This demonstrates that the higher optical penetration depth leads to more ablation despite the reflectivity being slightly higher at longer wavelengths. Above ~ 800 nm the ablation depth increases linearly with wavelength but with a small slope making any of these wavelengths a practical option for laser thermal processing HOPG. Using a Ti:Sapphire laser would be appropriate since it is tunable and can be used for other applications as opposed to using a fixed wavelength laser that operates closer to 1600 nm. There is only a ~ 17 nm difference in ablation depth between wavelengths of 800 nm and 1600 nm making wavelengths above 800 nm suitable for most laser thermal processing applications. Figure 5.2 shows the ablation depth with fluence for different wavelengths. It is seen that at low fluences the thresholds for each wavelength are very similar but as fluence increases the ablation depths diverge. At a

300 nm wavelength the ablation depths are quite low compared to longer wavelengths where they are all quite similar thus confirming the selection of longer wavelengths to be used for larger ablation depths.

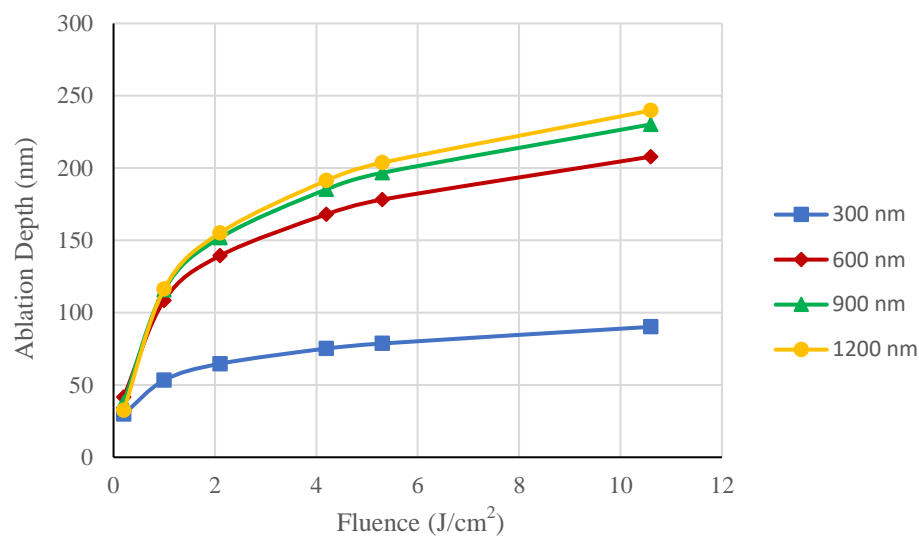


Figure 5.2 Single pulse ablation depth of HOPG with respect to fluence for different wavelengths.

The effect of wavelength on ablation depth can also be studied for rGO thin films using optical data obtained from Schmiedova *et al.* [39] to calculate the optical properties from Figure 2.11, although the optical data was only determined for 200 to 850 nm wavelengths. Figure 5.3 shows the single pulse ablation depth at a fluence of 5.3 J/cm² for wavelengths ranging from 200 to 800 nm.

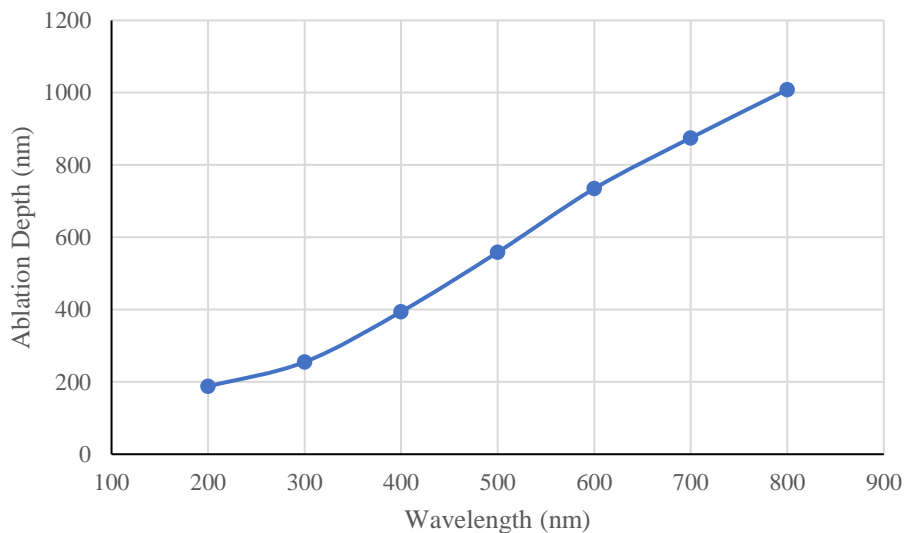


Figure 5.3 Single pulse ablation depth at different fluences for printed rGO.

A maximum ablation depth of 1000 nm is achieved at a laser wavelength of 800 nm and rGO shows a similar trend to that of HOPG where the ablation depth increases at longer wavelengths. Although the optical properties were not determined for longer wavelengths than 800 nm, it can be assumed based on HOPG that larger ablation depths will be achieved past 800 nm though it cannot be said if the slope of the curve is large enough to justify using laser wavelengths past 1000 nm. Plots of ablation depth against fluence for different laser wavelengths on rGO is shown in Figure 5.4.

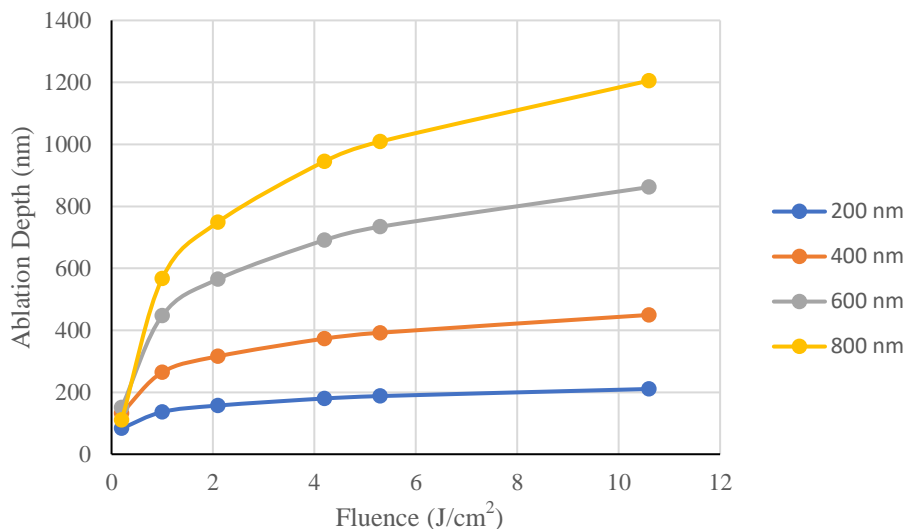


Figure 5.4 Single pulse ablation depth of printed rGO with respect to fluence for different wavelengths.

Similar to that of HOPG, it can be seen that the fluence thresholds are very close for different wavelengths at low fluences before diverging as fluence increases. Unlike HOPG, the difference in ablation depth as the wavelength increases is much larger making it more feasible to use longer wavelengths to achieve larger ablation depths.

5.3 Substrate Damage Analysis

With thin film thicknesses ranging from a monolayer (nm) to several microns, a substrate can be used to deposit and support the thin film and can influence the properties of the device during applications. Several substrate properties are important to consider when designing inkjet printed electronics for different applications. These factors can include the elastic modulus, tensile strength, melting or glass transition temperature, coefficient of thermal expansion (CTE), transparency and biodegradability. An emerging field of electronic devices is flexible thin films in which printed graphene has been extensively researched. Flexible inkjet printed graphene/GO devices have been studied using flexible substrates such as polyimide [77], PDMS [78], and PET [79], [80]. Polyimide is the most common substrate material for flexible electronics with a thickness ranging from 1.5 to

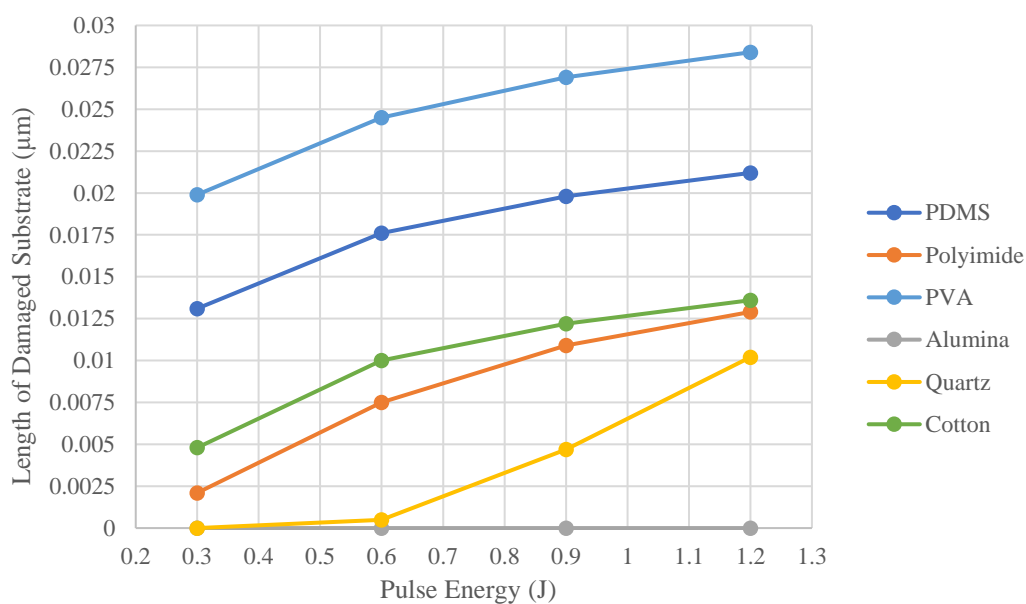
50 μm , a low CTE and high T_g making it an attractive substrate for laser micromachining of inkjet printed graphene. Polyimide is 90% transparent but has an orange hue making other polymers such as PET better options for transparent devices. PDMS, on the other hand, is a stretchable polymer making it useful for wearable electronics however it has a high CTE and may need to be deposited on another material with a lower CTE to prevent expansion. Ecoflex is a commercially available PDMS that is transparent and biodegradable. Other rigid substrates can also be used for inkjet printed graphene devices such as glass [81], [82], and ceramics [83].

Another growing interest in electronic device procurement lies in reducing electronic waste from toxic or long-decomposable materials. Polyvinyl alcohol is a water-soluble and transparent polymer that can act as a degradable substrate for inkjet printed devices. Htwe *et al.* fabricated an inkjet printed strain sensor using graphene/silver nanoparticle conductive ink on a PVA substrate [84]. Wearable electronics as e-textiles have also been proposed as a potential application for thin film electronics due to their comfort and ability to conform to the body. Research has been conducted into woven fabrics and yarns being used as substrate materials for thin film electronics such as Abdelkader *et al.* developing a screen-printed graphene oxide ink supercapacitor on woven cotton [85].

Using the 1D model, the effect of laser micromachining of rGO with various substrates can be examined to determine if substrate damage will occur. This is performed by observing the lattice thermal conduction into the substrate and noting the point where the T_g is met to decide how much substrate material might be damaged. It was found that the ablation depth of rGO is the same for all substrates. In the model, the deformed geometry module is deactivated so that no ablation is produced since the material removal in the model causes the electron thermal energy to propagate into the substrate even though the substrate has an electron thermal conductivity of zero. With the deformed geometry module turned off, the electron temperature in the substrate remains at room temperature and only the lattice thermal energy conducts into the substrate and the temperature vs. depth plot stays the same as if the deformed geometry module was on. Table 5.1 shows the thermal properties of the substrates used in the model and Figure 5.5 shows a plot of the depth of damaged substrate for each material with different pulse energies.

Table 5.1 Thermal properties of common substrates for printed electronics.

Material	Heat Capacity (J/g · K)	Density (kg/m ³)	Thermal Conductivity (W/m · K)	CTE (1/K)	T_g (K)
Polyimide	1100	1300	0.15	4.5×10^{-5}	633
PET	1250	1380	0.24	7.1×10^{-5}	347
PDMS	1460	970	0.16	9×10^{-4}	398
Alumina	900	3900	27	8×10^{-6}	2345
Quartz	730	2210	1.4	5.5×10^{-7}	1055
PVA	1500	1250	0.30	7×10^{-5}	353
Cotton	1340	466	0.046	N/A	519

**Figure 5.5** Length of damaged substrate with respect to pulse energy for different substrates.

From Figure 5.5 the polymers show greater substrate damage compared to quartz and alumina. This is due to the low T_g causing the damage threshold to be met at a lower temperature and a low thermal conductivity causing the temperature to remain near the substrate boundary rather than diffusing. Polyimide is the most favourable polymer for reducing substrate damage due to its high T_g as the thermal conductivity, heat capacity and density are relatively similar for the polymers. For cotton, the thermal conductivity is low causing minimal heat diffusion into the substrate and the temperature remains near the boundary, but the temperature for damage threshold is close to that of polyimide causing less damage than the other polymers. For quartz, the thermal conductivity is several times larger than the polymers causing the heat to diffuse further into the substrate but the T_g is large enough that less damage is observed compared to the polymers. The only material showing no thermal damage is alumina due to its large thermal conductivity and very high temperature for damage threshold which demonstrates why ceramics are commonly used as substrates.

Another important factor to consider during laser micromachining is the thermal expansion of the substrate. Using the coefficient of linear thermal expansion, the temperature difference between the substrate boundary and ambient temperature of the substrate, and the length between the substrate boundary and point of ambient temperature, it is possible to determine the amount of linear expansion using

$$\Delta L = \text{CTE} \cdot \Delta T \cdot L \quad (5.1)$$

In addition, the percentage of expansion can also be determined by $\Delta L/L$. Table 5.2 shows the linear expansion and percentage expansion for several different substrate materials based on the computational simulations.

Table 5.2 Results of substrate damage simulations.

Material	CTE	ΔT (K)	L (μm)	ΔL (μm)	$\Delta L/L$ (%)
Polyimide	4.5×10^{-5}	2247	0.042	0.0067	16.0
PET	7.1×10^{-5}	2087	0.048	0.0071	14.8
PVA	7×10^{-5}	2047	0.051	0.0073	14.3
PDMS	9×10^{-4}	2247	0.044	0.0044	10.1
Alumina	8×10^{-6}	472	0.326	0.0012	0.38
Quartz	5.5×10^{-7}	1557	0.119	0.00010	0.086

Similar to the discussion on substrate damage, where polymers show more pronounced damage, the polymers are also shown to have higher percentages of thermal expansion that is considerably larger than alumina and quartz due to their high CTE values. This can pose problems if the thin film being used has a much larger or smaller CTE compared to the polymer substrate and can lead to a reduction in device performance or complete failure. Alumina is shown to have a very small ΔT which is due to the product of its heat capacity and density being quite larger leading to lower temperatures at the substrate thin-film boundary. Alumina does, however, show considerable heat diffusion into the substrate due to its large thermal conductivity value but since the temperature difference is relatively small and its CTE is small, minimal thermal expansion occurs. Lastly, quartz can be seen as having the smallest amount of thermal expansion due to its very low CTE value. Although alumina and quartz have minimal thermal expansion, this may be a disadvantage if the thin film being used has a high thermal expansion leading to reduced device performance.

5.4 Ablation Efficiency

When conducting physical laser experiments, a complex optical system must be put together and fine tuned to ensure that the material sample is safely irradiated where other

equipment is then required to characterize the material damage. These processes can be expensive and time-consuming when testing a large range of parameters to determine optimal processing efficiency. FEA simulations have the advantage of being inexpensive and relatively fast allowing for many parameters to be considered. The following section outlines and discusses the results of various parametric studies used to determine the optimal ablation efficiency for rGO thin film. The experiment by Sinar *et al.* is used as a reference for comparison and to establish the laser and material properties.

As a first experiment, the single pulse ablation depth curve can be simulated to determine the ablation depth at different fluences. This curve can be used to find the fluence threshold for ablation and maximum ablation depth and be compared to the respective curve for HOPG in Figure 3.14 to understand the differences between simulation and physical experiment. The simulation was performed using the material properties of rGO and laser parameters that are adjusted to match those from the HOPG experiment which are shown in Table 5.3. Figure 5.6 shows the single pulse ablation depth at varying fluences for both rGO and HOPG.

Table 5.3 Adjusted laser parameters for rGO and HOPG comparison.

Parameter (Symbol, Unit)	Value
Pulse width (τ_p , fs)	120
Wavelength (λ , nm)	825
Fluence (F , J/cm ²)	0.2 – 10.6

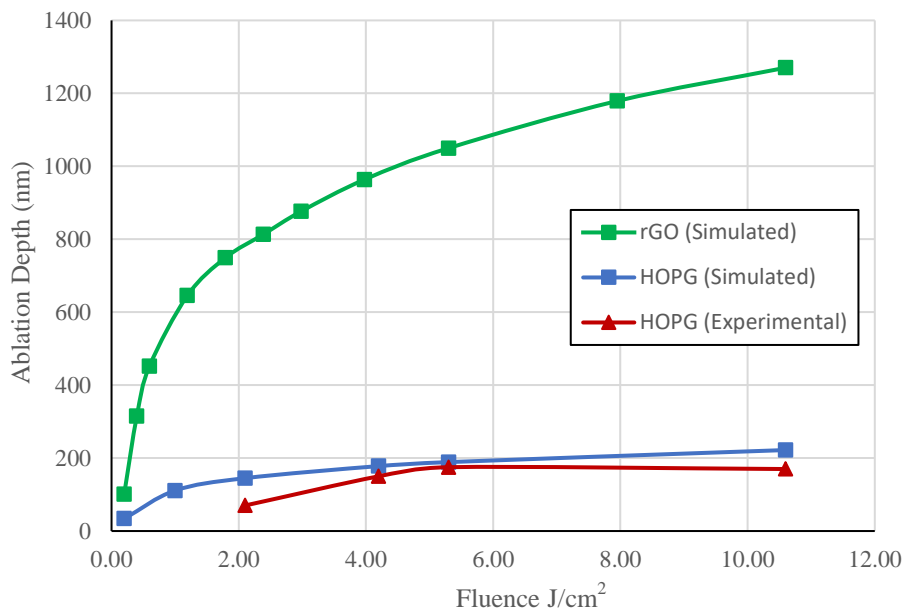


Figure 5.6 Comparison of single pulse ablation depth-fluence curves for simulated rGO and HOPG and experimental HOPG.

It is shown that the ablation depth is much larger for rGO thin film compared to HOPG. At a fluence of 5.3 J/cm² where the simulated and experimental ablation depth of HOPG are closest in agreement, rGO has an ablation depth of 1050 nm compared to 189 nm for HOPG. This large difference in ablation depth is likely due to the lower reflectivity and higher penetration depth of rGO that causes more energy to be absorbed that is also able to penetrate deeper. The lower density of rGO thin film is also responsible for the larger ablation depths since density contributes to the heat capacity where rGO can reach higher temperatures with the same amount of absorbed energy. In terms of the ablation threshold, F_{th} , the simulated values for rGO and HOPG were found to be 0.32 and 0.20 J/cm² respectively while the experimental ablation threshold for HOPG was found to be 0.19 J/cm² at 800 nm wavelength and 130 ps pulse width.

When considering the laser processing of materials, it is not only desirable to ensure a high process quality but also efficiency where the materials can be processed quickly. For a pulsed laser that is scanned in a line, the pulses overlap and is dependent on the pulse frequency and scanning speed. The amount of pulse overlap dictates the consistency of the

trench depth along the line where a low pulse overlap may produce a large variance in depth and a high pulse overlap will produce a low variance. Ensuring the pulse overlap is as low as possible, or the distance between successive pulses is as large as possible, while ensuring consistent trench depth will decide the optimal scan speed of the laser at a set pulse frequency. The distance between pulses, b , can be determined from

$$b = \frac{v}{f} \quad (5.2)$$

where v is the laser scanning speed and f is the pulse frequency. Therefore, using laser equipment with a higher scan speed and pulse frequency will result in faster processing times with the same quality since the distance between pulses remains the same.

Although for material removal and thickness reduction using ablation it is preferred to remove material up to a certain depth or line thickness, it can also be desirable to remove as much material as possible in a given laser scan. This can be done by determining the optimal peak fluence for a Gaussian beam which follows

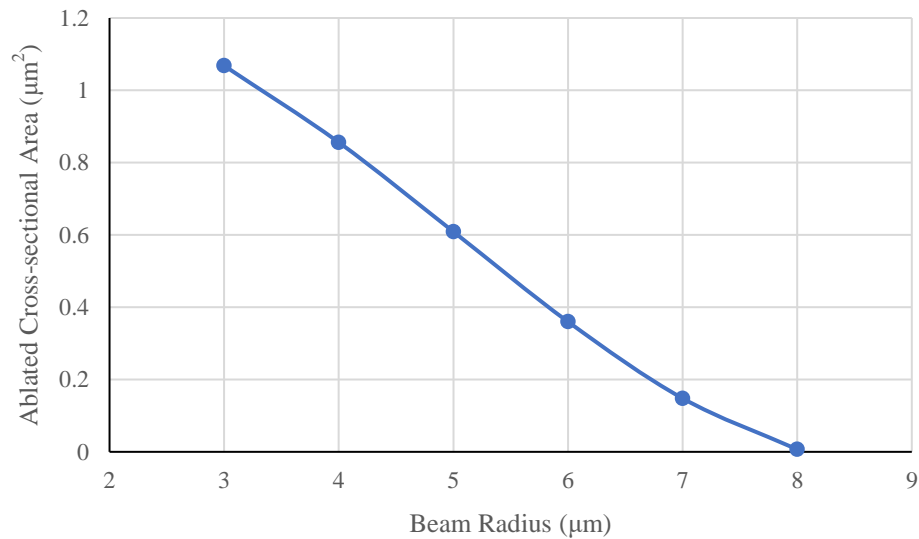
$$F = \frac{2E_p}{\pi\omega_0^2} \quad (5.3)$$

where E_p is the pulse energy and ω_0 is the laser spot radius.

It is apparent that decreasing ω_0 will increase the peak fluence resulting in larger temperatures within the material but decreasing ω_0 to a very small radius will result in the saturation fluence being reached and possibly unwanted damage to the material. Increasing ω_0 will heat a larger area of material but produces a lower peak fluence resulting in lower temperatures within the material. The influence of laser spot radius on material removal is investigated based on the laser parameters used in the experiment by Sinar *et al.* on rGO as shown in Table 5.4. Using a 2D axisymmetric TTM described in Section 4.1, the pulse energy is kept constant at 0.3 μJ and the beam radius is varied from 3 – 8 μm . Figure 5.7 shows the resultant cross-sectional material removal area.

Table 5.4 Laser parameters used for Sinar experiment [74].

Parameter (Symbol, Unit)	Value
Pulse width (τ_p , fs)	120 [74]
Wavelength (λ , nm)	775 [74]
Pulse energy (E, μ J)	0.3 [74]
Beam radius (ω_0 , μ m)	3 – 8

**Figure 5.7** Simulated cross-sectional area of ablation for rGO using different beam radii.

It is evident that a smaller beam radius will result in more material being removed which is due to the higher peak fluence. However, this higher material removal may not translate to more efficient material removal when considering that a smaller beam radius requires a smaller distance between pulses to achieve the same pulse overlap as larger beam radii. This can be expressed by

$$O = e^{-b^2/\omega_0^2} \quad (5.4)$$

where O is the pulse overlap. According to Equation 5.2, when b is decreased and f is fixed the scan speed will be smaller resulting in slower processing times. The beam radius must be chosen to find a balance between ablated cross-sectional area and laser scan speed for optimal material removal rate. This can be determined using

$$\dot{V} = fbA_c \quad (5.5)$$

where \dot{V} is the volume removal rate and A_c is the cross-sectional area determined from Figure 5.7.

Using a pulse frequency of 1000 Hz and a laser scan speed of 100 mm/min from the Sinar experiment, the distance between pulses was determined to be 1.67 μm . With a beam radius of 4 μm from the experiment, the pulse overlap was determined to be 0.84. This pulse overlap was then used in Equation 5.4 to determine the b values for each beam radius. Figure 5.8 shows the volume removal rate from Equation 5.5 plotted against different beam radii.

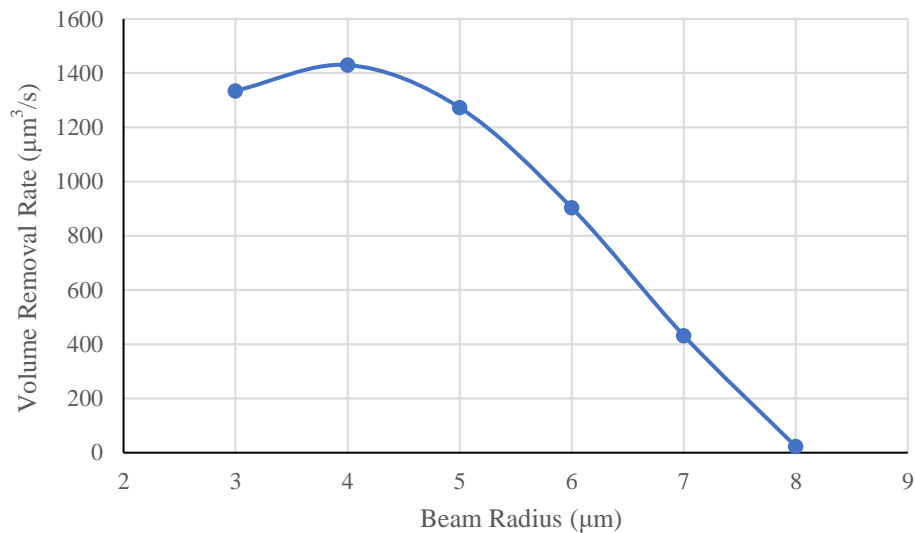


Figure 5.8 Simulated volume removal rate of rGO using different beam radii.

The volume removal rate reaches a peak at $\sim 1430 \mu\text{m}^3/\text{s}$ at a beam radius of 4 μm which corresponds to a peak laser fluence of $1.19 \text{ J}/\text{cm}^2$. This result agrees well with the

experiment by Sinar *et al.* as the beam diameter used was $\sim 8 \mu\text{m}$. It should be noted that this optimal fluence only corresponds to the average power of 0.3 mW used in the experiment and the optimal fluence for an increased average power will be slightly larger. There is some room for variability in the fluence or beam radius used as the volume removal rate for a beam radius of $3 \mu\text{m}$ and $5 \mu\text{m}$ is $1335 \mu\text{m}^3/\text{s}$ and $1275 \mu\text{m}^3/\text{s}$ respectively.

Some limitations associated with this study are computation times and the inability to simulate smaller beam radii. Each fluence simulation takes $\sim 2.5 - 3$ hours to compute as a fine relative tolerance and small timesteps are required to properly resolve the temperature distribution and resultant material removal. This can likely be improved by finetuning certain solver parameters and timesteps throughout the simulation. Smaller beam radii of $1 \mu\text{m}$ and $2 \mu\text{m}$ could not converge on a solution due to the highly nonlinear nature of the problem being solved with steep temperature gradients and crater profiles. This could also be improved by adjusting solver settings. The next section applies the same methodology used for the optimal ablation fluence to that of annealing.

5.5 Annealing Efficiency

The process of annealing involves heating a material to a threshold temperature for a set amount of time to cause changes to its physical properties. For the case of GO, ultrashort pulsed laser annealing offers an extremely precise method of removing residual groups to produce rGO which has a much better electrical conductivity and can be used in a variety of electronic applications. Under experimental conditions the process of determining appropriate laser parameters for reduction is largely performed by trial and error which can be inefficient in terms of both time and cost. The present study will investigate the role of laser parameters on annealing quality using the optimal fluence methodology from Section 5.4.

It has been shown that under ambient conditions, oxygen containing functional groups detach from the GO surface at $1000 - 1500 \text{ K}$ and at temperatures $> 3000 \text{ K}$ annealing of defects takes place resulting in an improved rGO structure [86]. Typical models that simulate the annealing of GO use complex molecular dynamic simulations with a domain on the molecular scale. Using FEA, the temperature distribution due to ultrashort pulsed

laser annealing can be computed and ideal laser parameters determined over a practical scale. The experiment by Sinar *et al.* recorded the sheet resistance of rGO samples using different combinations of laser power, scanning speed and number of passes where it was determined that the parameters giving the lowest sheet resistance are a laser power of 20 – 21 mW and a scan speed of 1200 mm/s. Using this laser power, simulations were performed with various beam radii to determine the optimal annealing fluence. Table 5.5 shows the laser parameters used in the simulation.

Table 5.5 Laser parameters for simulating the annealing process [74].

Parameter (Symbol, Unit)	Value
Pulse width (τ_p , fs)	120 [74]
Wavelength (λ , nm)	775 [74]
Pulse energy (E, μ J)	20.5 [74]
Beam radius (ω_0 , μ m)	60 – 160

Using a 2D axisymmetric TTM, the pulse energy is kept constant at 20.5 μ J and the beam radius is varied from 60 – 160 μ m. The cross-sectional area of material that reaches above 1000 K is determined by evaluating the integral of the 1000 K contour line in the simulation plot for each radius. Figure 5.9 shows the resultant cross-sectional area that reaches 1000 K.

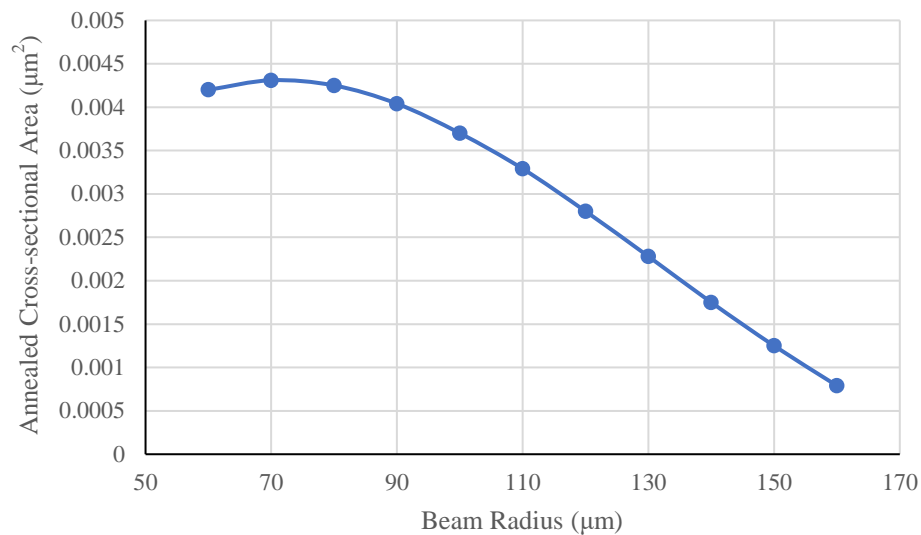


Figure 5.9 Simulated cross-sectional area of annealing for rGO using different beam radii.

The maximum annealed cross-sectional area occurs with a lower beam radius which is expected since the ablation study demonstrates the same relationship. From Equation 5.2 the distance between pulses is determined to be 20 μm and from Equation 5.4 the pulse overlap is determined to be 0.97. Using Equation 5.5 with a pulse frequency of 1000 Hz, Figure 5.10 shows the annealed volume rate for the different beam radii.

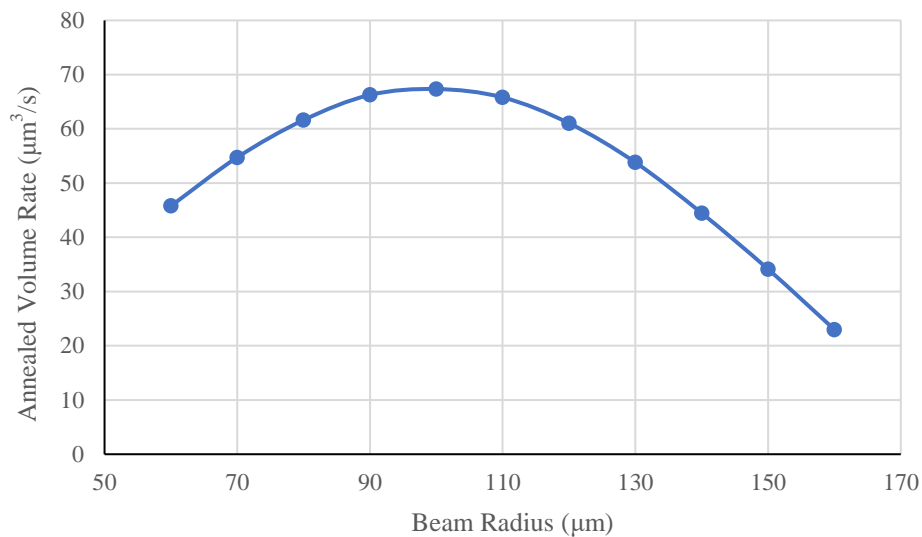


Figure 5.10 Simulated volume annealing rate of rGO using different beam radii.

A peak annealed volume rate of $67.34 \mu\text{m}^3/\text{s}$ is achieved at a radius of $\sim 100 \mu\text{m}$ corresponding to a peak fluence of $0.13 \text{ J}/\text{cm}^2$. However, unlike ablation, the total time at which the material remains at this temperature is important to consider for reduction. Figure 5.11 shows a plot of the time that the cross-sectional area from Figure 5.9 remains above 1000 K with respect to the beam radius.

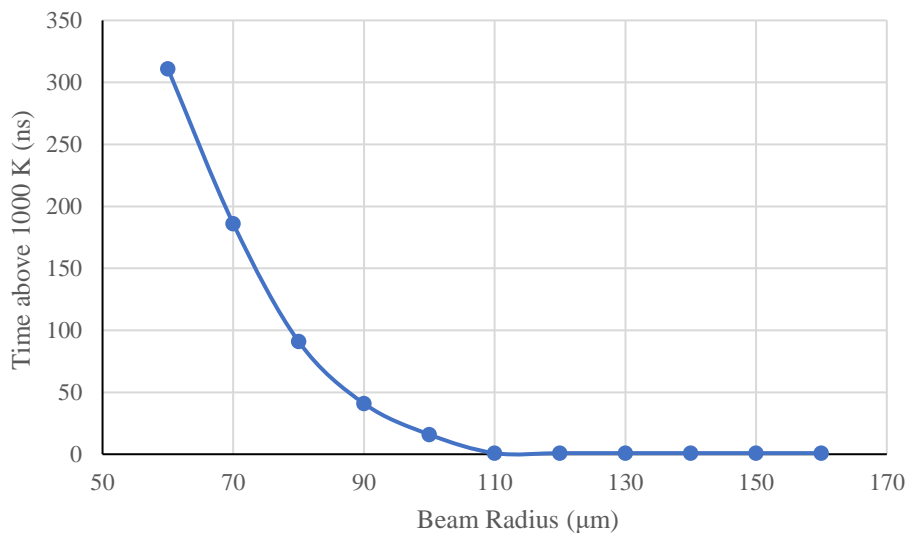


Figure 5.11 Time at which the cross-sectional area of rGO remain above 1000 K for different beam radii.

Figure 5.11 shows an exponential increase in exposure time as the beam radius decreases. Although a beam radius of 100 μm produces the optimal annealed volume rate, this will likely not give the best overall annealing quality since the volume is only heated above 1000 K for 16 ns. At smaller beam radii much longer exposure times occur which will result in greater reduction, but it is difficult to determine the balance between annealed volume rate and exposure time for optimal annealing efficiency. It should also be noted that at beam radii of 60 and 70 μm that the melting temperature of GO is exceeded causing unwanted damage to the material. This means that the optimal annealing beam radius should fall between 80 and 100 μm , or 0.13 to 0.2 J/cm^2 to achieve time efficient and high-quality annealing for an average power of 20.5 mW. These results will need to be confirmed by physical experiments to validate the accuracy of these simulations.

5.6 Concluding Remarks

Chapter 5 applied the 1D and 2D axisymmetric TTMs to understand the influence of laser parameters on annealing quality, ablation quality and substrate damage. Parametric studies

were performed on printed rGO and HOPG where it was identified that a laser wavelength of 800 nm or greater provides the greatest ablation depths. Parametric studies were performed on printed rGO to analyze the thermal damage to different substrates. It was found that PVA and PDMS see the most thermal damage with quartz and alumina seeing the least amount of thermal damage. In terms of thermal expansion polyimide and PET see the most expansion while alumina and quartz see the least. The ablation and annealing efficiency were also examined using parametric studies where it was found that the peak fluence at 0.3 mW for optimum material removal rate is 1.19 J/cm^2 and the peak fluence at 20.5 mW for optimum annealed volume rate lies between 0.13 to 0.2 J/cm^2 .

Chapter 6 Conclusions

6.1 Research Outcomes

The thesis presented an introduction to the theory and equations relating to laser-material interaction and develops a TTM to understand the influence of laser parameters on the micromachining of HOPG, rGO, and SLG and the annealing of rGO. The developed model can be used as a tool to identify efficient laser parameters to create carbon-based electronics without the need of performing time-consuming and costly experiments.

Chapter 1 identifies the research problem to be investigated in which there is need for a numerical model to study the relationship between laser processing parameters and annealing and micromachining quality and efficiency of graphene thin films. Potential applications of laser micromachining and annealing are also identified to underline the relevance of the work presented in this thesis. Currently, there has not been an extensive study on how laser parameters affect the annealing and ablation volume and their efficiency for printed rGO and there are also currently no numerical models concerning the ultrashort laser ablation of graphene or its derivatives.

Chapter 2 presents an introduction to the fundamental concepts of laser-material interaction and laser micromachining, as well as an overview of the key material properties for graphite, graphene, and graphene oxide. A state-of-the-art review was provided for the known thermal, optical and phonon properties of graphene and graphite. A review of laser experiments was also given for HOPG, rGO and SLG providing the reader with insight into how these materials react to ultrashort laser irradiation and the necessary laser parameters to anneal or ablate the material.

Chapter 3 presents the finite element model and simulation for the ultrashort laser ablation of HOPG based on the experiment by Shirk *et al.* [45] for validation with experiment. The TTM is presented with its corresponding equations and the material properties of HOPG and model settings are discussed. Chapter 4 applies the TTM to the pulsed laser ablation of printed rGO films for both single and multiple scanned pulses. The simulation results are compared with the experimental results of Sinar *et al.* [74]. Chapter 4 also extends the TTM to the MTM to simulate the pulsed laser ablation of SLG where the TTM and MTM results are compared.

Chapter 5 discusses the use of parametric studies to understand the relationship of laser processing parameters on annealing and ablation quality of GO/rGO and identifies the amount of thermal damage to different substrate materials. The results emphasize the importance of selecting optimal laser parameters to achieve efficient annealing and micromachining of printed rGO films.

6.2 Contributions

The thesis provided a detailed description of numerical models in COMSOL Multiphysics that simulate the ultrashort pulsed laser ablation and annealing of HOPG, rGO and SLG films. To the author's knowledge this is the first example of a numerical FEA model being developed for ultrashort laser ablation of graphite-based materials. The developed model serves as a tool to identify efficient laser processing parameters for the micromachining and heat treating of carbon-based electronic devices providing time and cost savings compared to conducting physical experiments.

Through the simulation of ultrashort pulsed laser ablation of HOPG using material properties obtained through literature, the model was found to be in good agreement at certain fluences achieving similar ablation depths to those recorded in experiment with the closest relative difference being only 11.4% for a fluence of 5.3 J/cm^2 . For multiple pulse simulations in a single spot, the model was found to be in good agreement and falls into the bounds of error of the physical experiment. For rGO, material properties were obtained from literature and the model was validated through a physical experiment. The simulated ablation depth was found to be in good agreement with the experiment with sufficient material removal up to the substrate. A relation was used to approximate the multiple pulses scanned in a line to a single spot under different pulse frequencies and were also in good agreement.

For SLG, material properties were obtained from literature and ultrashort pulsed laser ablation was simulated to compare fluence thresholds against physical experiment where the simulated fluence threshold was found to have a relative difference of 33% compared to experiment. The ablated crater diameter was also compared to experiment and found to have a relative difference of 6%. The TTM was then extended to an MTM although results

were found to be similar with a relative difference of 40% for fluence threshold and a relative difference of 6% for crater diameter.

Parametric studies were performed for different laser processing parameters. The most energy efficient laser wavelength for ablation and annealing was identified to be in the near infrared range at laser wavelengths greater than 800 nm. Multiple substrates were also analyzed using parametric studies to characterize thermal damage and expansion. It was found that PVA and PDMS experience the most thermal damage while quartz and alumina see the least. In terms of thermal expansion polyimide and PET see the most expansion while alumina and quartz see the least. Ablation and annealing optimization studies were also performed to identify the most time efficient fluences under constant pulse overlap. Under an average laser power of 0.3 mW the ideal fluence was found to be 1.19 J/cm² for maximum volumetric material removal rate. Under an average laser power of 20.5 mW the ideal laser fluence was found to be 0.13 to 0.2 J/cm² for maximum annealed volume rate.

6.3 Future Research

Although the developed model is validated through experiment for HOPG and rGO, future work can be conducted to acquire more accurate material properties and controlled experiments can be performed to better validate the model. In terms of material properties, most used in the model are obtained from experiments from other literature where the material properties may differ from the experiment used to validate the model. These properties include the refractive index and extinction coefficient which were obtained from another printed rGO film experiment and thermal properties such as thermal conductivity and specific heat capacity which were assumed to be the same as HOPG along with the electron-phonon coupling parameter.

Another property that was not included in the model is the c-axis electrical conductivity where it was assumed to be the same as the ab-plane electrical conductivity and could lead to different electron temperatures. The coefficient of thermal expansion can be determined for rGO to understand what substrates share similar values and can be used without causing unwanted strain on either material. Finally, the density was also taken from another experiment of printed rGO and would lead to different lattice heat capacity values that can

influence the ablation depths. For SLG, the MTM can be significantly improved by using temperature dependent phonon properties. The presented MTM used R.T properties for each phonon branch and with the ablation temperature being ~ 5000 K these properties can change significantly leading to a much different simulated fluence threshold. These phonon properties must be obtained through complex first principle calculations. Another area to achieve more accurate simulations for rGO can be found through the use of temperature dependent material properties such as the optical properties which can change significantly as the material reaches closer to its critical temperature.

Aside from improved material properties, the model can be calibrated through comparison with controlled experiments. This includes adjusting laser parameters such as the fluence, beam radius, scan speed and pulse frequency to observe inaccuracies in the ablation depth or crater diameter and adjust the model accordingly. For example, the saturation fluence can be determined through experiments under different fluences, scan speeds or pulse frequencies and an adjustment factor can be applied to the model to accurately predict when the saturation fluence will be reached. Experiments also need to be conducted to calibrate the model for annealing to understand the relationship of annealing time and annealing volume on the degree of reduction which will allow for a more accurate prediction of improved sheet resistance in rGO.

In terms of simulation results, more parametric studies can be performed to determine the optimal ablation and annealing fluence at different laser powers. This will allow for the most efficient fluence to be selected when different lasers are used. Modifications can also be made to the model to improve solution time, file size and solution convergence. Currently the model is unable to simulate very small beam radii relative to laser energy without receiving a convergence error due to the crater profile being too steep. This can be fixed by adjusting nonlinear solver settings such as tolerance and damping factors to achieve convergence. These settings can also be finetuned to achieve faster computation times due to better convergence. Finally, the solver timesteps can be finetuned and made to be variable based on laser parameters to solve for enough data points for an accurate solution without creating extremely large file sizes that can take a long time to plot.

References

- [1] P. R. Wallace, 'The Band Theory of Graphite', *Phys. Rev.*, vol. 71, no. 9, pp. 622–634, May 1947, doi: 10.1103/PhysRev.71.622.
- [2] R. Peierls, 'Quelques propriétés typiques des corps solides', *Ann. Inst. Henri Poincaré*, vol. 5, no. 3, pp. 177–22, 1935.
- [3] K. S. Novoselov *et al.*, 'Electric Field Effect in Atomically Thin Carbon Films', *Science*, vol. 306, no. 5696, pp. 666–669, Oct. 2004, doi: 10.1126/science.1102896.
- [4] F. Torrisi *et al.*, 'Inkjet-Printed Graphene Electronics', *ACS Nano*, vol. 6, no. 4, pp. 2992–3006, Apr. 2012, doi: 10.1021/nn2044609.
- [5] C.-P. Wang, C.-P. Chou, T.-L. Chang, and C.-Y. Chou, 'Micromachining of graphene based micro-capacitor using picosecond laser ablation', *Microelectron. Eng.*, vol. 189, pp. 69–73, Apr. 2018, doi: 10.1016/j.mee.2017.12.011.
- [6] S. Luo, Y. Wang, G. Wang, F. Liu, Y. Zhai, and Y. Luo, 'Hybrid spray-coating, laser-scribing and ink-dispensing of graphene sensors/arrays with tunable piezoresistivity for in situ monitoring of composites', *Carbon*, vol. 139, pp. 437–444, Nov. 2018, doi: 10.1016/j.carbon.2018.07.014.
- [7] S.-F. Tseng, 'Picosecond laser micropatterning of graphene films for rapid heating chips', *Appl. Surf. Sci.*, vol. 450, pp. 380–386, Aug. 2018, doi: 10.1016/j.apsusc.2018.04.212.
- [8] T.-L. Chang, Z.-C. Chen, and S.-F. Tseng, 'Laser micromachining of screen-printed graphene for forming electrode structures', *Appl. Surf. Sci.*, vol. 374, pp. 305–311, Jun. 2016, doi: 10.1016/j.apsusc.2015.12.031.
- [9] J. Narayan, 'Interface instability and cell formation in ion-implanted and laser-annealed silicon', *J. Appl. Phys.*, vol. 52, no. 3, p. 1289, Aug. 1998, doi: 10.1063/1.329753.
- [10] S. H. Huh, *Thermal Reduction of Graphene Oxide*. IntechOpen, 2011. doi: 10.5772/14156.
- [11] S. Gupta, P. Joshi, and J. Narayan, 'Electron mobility modulation in graphene oxide by controlling carbon melt lifetime', *Carbon*, vol. 170, pp. 327–337, Dec. 2020, doi: 10.1016/j.carbon.2020.07.073.

- [12] A. Bhaumik and J. Narayan, 'Conversion of p to n-type reduced graphene oxide by laser annealing at room temperature and pressure', *J. Appl. Phys.*, vol. 121, no. 12, p. 125303, Mar. 2017, doi: 10.1063/1.4979211.
- [13] P. R. Riley, P. Joshi, H. Penchev, J. Narayan, and R. J. Narayan, 'One-Step Formation of Reduced Graphene Oxide from Insulating Polymers Induced by Laser Writing Method', *Crystals*, vol. 11, no. 11, Art. no. 11, Nov. 2021, doi: 10.3390/cryst11111308.
- [14] S. Mishra and V. Yadava, 'Laser Beam MicroMachining (LBMM) – A review', *Opt. Lasers Eng.*, vol. 73, pp. 89–122, Oct. 2015, doi: 10.1016/j.optlaseng.2015.03.017.
- [15] J. P. Callan, 'Ultrafast dynamics and phase changes in solids excited by femtosecond laser pulses', Ph.D., Harvard University, United States -- Massachusetts, 2000. Accessed: Apr. 18, 2022. [Online]. Available: <https://www.proquest.com/docview/304595521/abstract/5CF66ED508AF43BBPQ/1>
- [16] X. Liu, D. Du, and G. Mourou, 'Laser ablation and micromachining with ultrashort laser pulses', *IEEE J. Quantum Electron.*, vol. 33, no. 10, pp. 1706–1716, Oct. 1997, doi: 10.1109/3.631270.
- [17] D. Perez and L. J. Lewis, 'Molecular-dynamics study of ablation of solids under femtosecond laser pulses', *Phys. Rev. B*, vol. 67, no. 18, p. 184102, May 2003, doi: 10.1103/PhysRevB.67.184102.
- [18] C. Cheng and X. Xu, 'Mechanisms of decomposition of metal during femtosecond laser ablation', *Phys. Rev. B*, vol. 72, no. 16, p. 165415, Oct. 2005, doi: 10.1103/PhysRevB.72.165415.
- [19] C. Lee, X. Wei, J. W. Kysar, and J. Hone, 'Measurement of the elastic properties and intrinsic strength of monolayer graphene', *Science*, vol. 321, no. 5887, pp. 385–388, Jul. 2008, doi: 10.1126/science.1157996.
- [20] A. A. Balandin *et al.*, 'Superior Thermal Conductivity of Single-Layer Graphene', *Nano Lett.*, vol. 8, no. 3, pp. 902–907, Mar. 2008, doi: 10.1021/nl0731872.
- [21] M. Cai, D. Thorpe, D. H. Adamson, and H. C. Schniepp, 'Methods of graphite exfoliation', *J. Mater. Chem.*, vol. 22, no. 48, pp. 24992–25002, Nov. 2012, doi: 10.1039/C2JM34517J.

- [22] G. Hu *et al.*, ‘Functional inks and printing of two-dimensional materials’, *Chem. Soc. Rev.*, vol. 47, no. 9, pp. 3265–3300, May 2018, doi: 10.1039/C8CS00084K.
- [23] Y. Zhu *et al.*, ‘Graphene and Graphene Oxide: Synthesis, Properties, and Applications’, *Adv. Mater.*, vol. 22, no. 35, pp. 3906–3924, 2010, doi: 10.1002/adma.201001068.
- [24] C. K. Chua and M. Pumera, ‘Chemical reduction of graphene oxide: a synthetic chemistry viewpoint’, *Chem. Soc. Rev.*, vol. 43, no. 1, pp. 291–312, Dec. 2013, doi: 10.1039/C3CS60303B.
- [25] I. Jung, D. A. Dikin, R. D. Piner, and R. S. Ruoff, ‘Tunable Electrical Conductivity of Individual Graphene Oxide Sheets Reduced at “Low” Temperatures’, *Nano Lett.*, vol. 8, no. 12, pp. 4283–4287, Dec. 2008, doi: 10.1021/nl8019938.
- [26] V. Strong *et al.*, ‘Patterning and Electronic Tuning of Laser Scribed Graphene for Flexible All-Carbon Devices’, *ACS Nano*, vol. 6, no. 2, pp. 1395–1403, Feb. 2012, doi: 10.1021/nn204200w.
- [27] L. X. Benedict, S. G. Louie, and M. L. Cohen, ‘Heat capacity of carbon nanotubes’, *Solid State Commun.*, vol. 100, no. 3, pp. 177–180, Oct. 1996, doi: 10.1016/0038-1098(96)00386-9.
- [28] K. I. Bolotin, K. J. Sikes, J. Hone, H. L. Stormer, and P. Kim, ‘Temperature-Dependent Transport in Suspended Graphene’, *Phys. Rev. Lett.*, vol. 101, no. 9, p. 096802, Aug. 2008, doi: 10.1103/PhysRevLett.101.096802.
- [29] H. O. Pierson, ‘3 - Graphite Structure and Properties’, in *Handbook of Carbon, Graphite, Diamonds and Fullerenes*, H. O. Pierson, Ed. Oxford: William Andrew Publishing, 1993, pp. 43–69. doi: 10.1016/B978-0-8155-1339-1.50008-6.
- [30] A. Alofi and G. P. Srivastava, ‘Evolution of thermal properties from graphene to graphite’, *Appl. Phys. Lett.*, vol. 104, no. 3, p. 031903, Jan. 2014, doi: 10.1063/1.4862319.
- [31] E. Pop, V. Varshney, and A. K. Roy, ‘Thermal properties of graphene: Fundamentals and applications’, *MRS Bull.*, vol. 37, no. 12, pp. 1273–1281, Dec. 2012, doi: 10.1557/mrs.2012.203.
- [32] J. H. Seol *et al.*, ‘Two-Dimensional Phonon Transport in Supported Graphene’, *Science*, vol. 328, no. 5975, pp. 213–216, Apr. 2010, doi: 10.1126/science.1184014.

- [33] W. Jang, Z. Chen, W. Bao, C. N. Lau, and C. Dames, 'Thickness-Dependent Thermal Conductivity of Encased Graphene and Ultrathin Graphite', *Nano Lett.*, vol. 10, no. 10, pp. 3909–3913, Oct. 2010, doi: 10.1021/nl101613u.
- [34] J. Crossno *et al.*, 'Observation of the Dirac fluid and the breakdown of the Wiedemann-Franz law in graphene', *Science*, vol. 351, no. 6277, pp. 1058–1061, Mar. 2016, doi: 10.1126/science.aad0343.
- [35] T. Y. Kim, C.-H. Park, and N. Marzari, 'The Electronic Thermal Conductivity of Graphene', *Nano Lett.*, vol. 16, no. 4, pp. 2439–2443, Apr. 2016, doi: 10.1021/acs.nanolett.5b05288.
- [36] R. R. Nair *et al.*, 'Fine Structure Constant Defines Visual Transparency of Graphene', *Science*, vol. 320, no. 5881, pp. 1308–1308, Jun. 2008, doi: 10.1126/science.1156965.
- [37] G. Xing, H. Guo, X. Zhang, T. C. Sum, and C. H. A. Huan, 'The Physics of ultrafast saturable absorption in graphene', *Opt. Express*, vol. 18, no. 5, pp. 4564–4573, Mar. 2010, doi: 10.1364/OE.18.004564.
- [38] B. Song *et al.*, 'Broadband optical properties of graphene and HOPG investigated by spectroscopic Mueller matrix ellipsometry', *Appl. Surf. Sci.*, vol. 439, pp. 1079–1087, May 2018, doi: 10.1016/j.apsusc.2018.01.051.
- [39] V. Schmiedova *et al.*, 'Physical Properties Investigation of Reduced Graphene Oxide Thin Films Prepared by Material Inkjet Printing', *J. Nanomater.*, vol. 2017, p. e3501903, Aug. 2017, doi: 10.1155/2017/3501903.
- [40] Y. Zhang, L. Zhang, and C. Zhou, 'Review of Chemical Vapor Deposition of Graphene and Related Applications', *Acc. Chem. Res.*, vol. 46, no. 10, pp. 2329–2339, Oct. 2013, doi: 10.1021/ar300203n.
- [41] N. I. Zaaba, K. L. Foo, U. Hashim, S. J. Tan, W.-W. Liu, and C. H. Voon, 'Synthesis of Graphene Oxide using Modified Hummers Method: Solvent Influence', *Procedia Eng.*, vol. 184, pp. 469–477, Jan. 2017, doi: 10.1016/j.proeng.2017.04.118.
- [42] T. Venkatesan *et al.*, 'Measurement of Thermodynamic Parameters of Graphite by Pulsed-Laser Melting and Ion Channeling', *Phys. Rev. Lett.*, vol. 53, no. 4, pp. 360–363, Jul. 1984, doi: 10.1103/PhysRevLett.53.360.

- [43] T. Dallas, M. Holtz, H. Ahn, and M. C. Downer, 'Structural phase of femtosecond-laser-melted graphite', *Phys. Rev. B*, vol. 49, no. 2, pp. 796–801, Jan. 1994, doi: 10.1103/PhysRevB.49.796.
- [44] K. Sokolowski-Tinten *et al.*, 'Femtosecond laser-induced ablation of graphite', in *Ultrafast Phenomena (2000)*, paper ThB4, Jul. 2000, p. ThB4. doi: 10.1364/UP.2000.ThB4.
- [45] M. D. Shirk and P. A. Molian, 'Ultra-short pulsed laser ablation of highly oriented pyrolytic graphite', *Carbon*, vol. 39, no. 8, pp. 1183–1193, Jul. 2001, doi: 10.1016/S0008-6223(00)00236-0.
- [46] M. Lenner, A. Kaplan, Ch. Huchon, and R. E. Palmer, 'Ultrafast laser ablation of graphite', *Phys. Rev. B*, vol. 79, no. 18, p. 184105, May 2009, doi: 10.1103/PhysRevB.79.184105.
- [47] M. Lenner, A. Kaplan, and R. E. Palmer, 'Nanoscale Coulomb explosion in ultrafast graphite ablation', *Appl. Phys. Lett.*, vol. 90, no. 15, p. 153119, Apr. 2007, doi: 10.1063/1.2721392.
- [48] A. A. Ionin and S. I. Kudryashov, 'Thermal melting and ablation dynamics on a femtosecond laser-heated highly-oriented pyrolytic graphite surface', *JETP Lett.*, vol. 104, no. 8, pp. 573–577, Oct. 2016, doi: 10.1134/S0021364016200042.
- [49] D. Sun *et al.*, 'Ultrafast Relaxation of Excited Dirac Fermions in Epitaxial Graphene Using Optical Differential Transmission Spectroscopy', *Phys. Rev. Lett.*, vol. 101, no. 15, p. 157402, Oct. 2008, doi: 10.1103/PhysRevLett.101.157402.
- [50] H. Wang *et al.*, 'Ultrafast relaxation dynamics of hot optical phonons in graphene', *Appl. Phys. Lett.*, vol. 96, no. 8, p. 081917, Feb. 2010, doi: 10.1063/1.3291615.
- [51] A. K. Vallabhaneni, D. Singh, H. Bao, J. Murthy, and X. Ruan, 'Reliability of Raman measurements of thermal conductivity of single-layer graphene due to selective electron-phonon coupling: A first-principles study', *Phys. Rev. B*, vol. 93, no. 12, p. 125432, Mar. 2016, doi: 10.1103/PhysRevB.93.125432.
- [52] A. Roberts, D. Cormode, C. Reynolds, T. Newhouse-Illige, B. J. LeRoy, and A. S. Sandhu, 'Response of graphene to femtosecond high-intensity laser irradiation', *Appl. Phys. Lett.*, vol. 99, no. 5, p. 051912, Aug. 2011, doi: 10.1063/1.3623760.

- [53] R. Sahin, E. Simsek, and S. Akturk, 'Nanoscale patterning of graphene through femtosecond laser ablation', *Appl. Phys. Lett.*, vol. 104, no. 5, p. 053118, Feb. 2014, doi: 10.1063/1.4864616.
- [54] Z. Lin *et al.*, 'Precise Control of the Number of Layers of Graphene by Picosecond Laser Thinning', *Sci. Rep.*, vol. 5, no. 1, Art. no. 1, Jun. 2015, doi: 10.1038/srep11662.
- [55] T. Dong, M. Sparkes, C. Durkan, and W. O'Neill, 'Evaluating femtosecond laser ablation of graphene on SiO₂/Si substrate', *J. Laser Appl.*, vol. 28, no. 2, p. 022202, May 2016, doi: 10.2351/1.4944510.
- [56] I. Bobrinetskiy, A. Emelianov, A. Nasibulin, I. Komarov, N. Otero, and P. M. Romero, 'Photophysical and photochemical effects in ultrafast laser patterning of CVD graphene', *J. Phys. Appl. Phys.*, vol. 49, no. 41, p. 41LT01, Oct. 2016, doi: 10.1088/0022-3727/49/41/41LT01.
- [57] A. Gil-Villalba, R. Meyer, R. Giust, L. Rapp, C. Billet, and F. Courvoisier, 'Single shot femtosecond laser nano-ablation of CVD monolayer graphene', *Sci. Rep.*, vol. 8, no. 1, Art. no. 1, Oct. 2018, doi: 10.1038/s41598-018-32957-3.
- [58] D. Sinar, G. K. Knopf, S. Nikumb, and A. Andrushchenko, 'Laser micromachining of oxygen reduced graphene-oxide films', in *Micromachining and Microfabrication Process Technology XIX*, Mar. 2014, vol. 8973, pp. 135–144. doi: 10.1117/12.2038423.
- [59] S.-F. Tseng, C.-H. Liao, W.-T. Hsiao, and T.-L. Chang, 'Ultrafast laser direct writing of screen-printed graphene-based strain electrodes for sensing glass deformation', *Ceram. Int.*, vol. 47, no. 20, pp. 29099–29108, Oct. 2021, doi: 10.1016/j.ceramint.2021.07.071.
- [60] D. Sinar, G. K. Knopf, and S. Nikumb, 'Laser assisted reduction of printed GO films and traces', in *14th IEEE International Conference on Nanotechnology*, Aug. 2014, pp. 549–553. doi: 10.1109/NANO.2014.6968086.
- [61] J. Ren, R. Ahmed, and H. Butt, 'Finite element analysis of nanosecond pulsed laser ablation of various materials', *World J. Eng.*, vol. 14, no. 6, pp. 489–496, Jan. 2017, doi: 10.1108/WJE-12-2016-0149.

- [62] S. Sinha, 'Nanosecond laser ablation of graphite: A thermal model based simulation', *J. Laser Appl.*, vol. 30, no. 1, p. 012008, Feb. 2018, doi: 10.2351/1.5021520.
- [63] X. Wang, Y. Huang, C. Li, and B. Xu, 'Numerical simulation and experimental study on picosecond laser ablation of stainless steel', *Opt. Laser Technol.*, vol. 127, p. 106150, Jul. 2020, doi: 10.1016/j.optlastec.2020.106150.
- [64] V. Jagota, A. P. S. Sethi, and K. Kumar, 'Finite Element Method: An Overview', *Walailak J. Sci. Technol. WJST*, vol. 10, no. 1, Art. no. 1, Jan. 2013.
- [65] T. Q. Qiu and C. L. Tien, 'Heat Transfer Mechanisms During Short-Pulse Laser Heating of Metals', *J. Heat Transf.*, vol. 115, no. 4, pp. 835–841, Nov. 1993, doi: 10.1115/1.2911377.
- [66] J. Cheng *et al.*, 'A review of ultrafast laser materials micromachining', *Opt. Laser Technol.*, vol. 46, pp. 88–102, Mar. 2013, doi: 10.1016/j.optlastec.2012.06.037.
- [67] J.-P. Issi, P. T. Araujo, and M. S. Dresselhaus, 'Electron and Phonon Transport in Graphene in and out of the Bulk', in *Physics of Graphene*, H. Aoki and M. S. Dresselhaus, Eds. Cham: Springer International Publishing, 2014, pp. 65–112. doi: 10.1007/978-3-319-02633-6_3.
- [68] S. Y. Zhou *et al.*, 'First direct observation of Dirac fermions in graphite', *Nat. Phys.*, vol. 2, no. 9, Art. no. 9, Sep. 2006, doi: 10.1038/nphys393.
- [69] H. Shinotsuka, S. Tanuma, C. J. Powell, and D. R. Penn, 'Calculations of electron inelastic mean free paths. X. Data for 41 elemental solids over the 50 eV to 200 keV range with the relativistic full Penn algorithm', *Surf. Interface Anal.*, vol. 47, no. 9, pp. 871–888, 2015, doi: 10.1002/sia.5789.
- [70] N. Medvedev and I. Milov, 'Electron-phonon coupling in metals at high electronic temperatures', *Phys. Rev. B*, vol. 102, no. 6, p. 064302, Aug. 2020, doi: 10.1103/PhysRevB.102.064302.
- [71] A. I. Savvatimskiy, S. V. Onufriev, and S. A. Konyukhov, 'Thermophysical properties of graphite HOPG and HAPG in the solid state and under melting (from 2000 K up to 5000 K)', *J. Phys. Conf. Ser.*, vol. 891, p. 012319, Nov. 2017, doi: 10.1088/1742-6596/891/1/012319.

- [72] G. V. Samsonov, *Handbook of the Physicochemical Properties of the Elements*, 1st ed. Springer New York, NY. Accessed: Aug. 04, 2022. [Online]. Available: <https://link.springer.com/book/10.1007/978-1-4684-6066-7>
- [73] H. R. Leider, O. H. Krikorian, and D. A. Young, ‘Thermodynamic properties of carbon up to the critical point’, *Carbon*, vol. 11, no. 5, pp. 555–563, Oct. 1973, doi: 10.1016/0008-6223(73)90316-3.
- [74] D. M. Sinar, ‘Synthesis and Drop-on-Demand Deposition of Graphene Derivative Inks for Flexible Thin Film Electronics’, Ph.D., Western University, 2018.
- [75] Z. Xie, L. Liu, N. Xiao, Y. Zhong, and X. Jing, ‘Preparation and Application of Carbon-Based Conductive Ink Based on Graphene’, in *Advanced Graphic Communication, Printing and Packaging Technology*, Singapore, 2020, pp. 623–629. doi: 10.1007/978-981-15-1864-5_85.
- [76] Z. Lu, A. Vallabhaneni, B. Cao, and X. Ruan, ‘Phonon branch-resolved electron-phonon coupling and the multitemperature model’, *Phys. Rev. B*, vol. 98, no. 13, p. 134309, Oct. 2018, doi: 10.1103/PhysRevB.98.134309.
- [77] M. H. Ervin, L. T. Le, and W. Y. Lee, ‘Inkjet-Printed Flexible Graphene-Based Supercapacitor’, *Electrochimica Acta*, vol. 147, pp. 610–616, Nov. 2014, doi: 10.1016/j.electacta.2014.10.006.
- [78] S.-H. Bae, Y. Lee, B. K. Sharma, H.-J. Lee, J.-H. Kim, and J.-H. Ahn, ‘Graphene-based transparent strain sensor’, *Carbon*, vol. 51, pp. 236–242, Jan. 2013, doi: 10.1016/j.carbon.2012.08.048.
- [79] H. Chi, L. J. Ze, X. Zhou, and F. Wang, ‘GO film on flexible substrate: An approach to wearable colorimetric humidity sensor’, *Dyes Pigments*, vol. 185, p. 108916, Feb. 2021, doi: 10.1016/j.dyepig.2020.108916.
- [80] D. J. Finn *et al.*, ‘Inkjet deposition of liquid-exfoliated graphene and MoS₂ nanosheets for printed device applications’, *J. Mater. Chem. C*, vol. 2, no. 5, pp. 925–932, Jan. 2014, doi: 10.1039/C3TC31993H.
- [81] Y. Zhang *et al.*, ‘Direct imprinting of microcircuits on graphene oxides film by femtosecond laser reduction’, *Nano Today*, vol. 5, no. 1, pp. 15–20, Feb. 2010, doi: 10.1016/j.nantod.2009.12.009.

- [82] Y. Zhou *et al.*, ‘Microstructuring of Graphene Oxide Nanosheets Using Direct Laser Writing’, *Adv. Mater.*, vol. 22, no. 1, pp. 67–71, 2010, doi: 10.1002/adma.200901942.
- [83] R. Ghosh, A. Midya, S. Santra, S. K. Ray, and P. K. Guha, ‘Chemically Reduced Graphene Oxide for Ammonia Detection at Room Temperature’, *ACS Publications*, Jul. 31, 2013. <https://pubs.acs.org/doi/pdf/10.1021/am4019109> (accessed Aug. 04, 2022).
- [84] Y. Z. N. Htwe, I. N. Hidayah, and M. Mariatti, ‘Performance of inkjet-printed strain sensor based on graphene/silver nanoparticles hybrid conductive inks on polyvinyl alcohol substrate’, *J. Mater. Sci. Mater. Electron.*, vol. 31, no. 18, pp. 15361–15371, Sep. 2020, doi: 10.1007/s10854-020-04100-4.
- [85] A. M. Abdelkader, N. Karim, C. Vallés, S. Afroj, K. S. Novoselov, and S. G. Yeates, ‘Ultraflexible and robust graphene supercapacitors printed on textiles for wearable electronics applications’, *2D Mater.*, vol. 4, no. 3, p. 035016, Jul. 2017, doi: 10.1088/2053-1583/aa7d71.
- [86] N. D. Orekhov *et al.*, ‘Mechanism of graphene oxide laser reduction at ambient conditions: Experimental and ReaxFF study’, *Carbon*, vol. 191, pp. 546–554, May 2022, doi: 10.1016/j.carbon.2022.02.018.

Appendix

Appendix A: Preliminary Simulation Results

A.1: Stainless Steel Ultrashort Laser Ablation

A preliminary TTM simulation was conducted for the ultrashort laser ablation of stainless steel based on a simulation by Wang *et al.* [63]. The crater profile is shown in Figure A1, and the electron and lattice temperature plots are shown Figure A2. This model served as a test to obtain results using a TTM on COMSOL Multiphysics compared to a simulation with known results. The results correspond to a single pulse with an energy of $6 \mu\text{J}$ and a pulsewidth of 10 ps. The material properties can be found in [63].

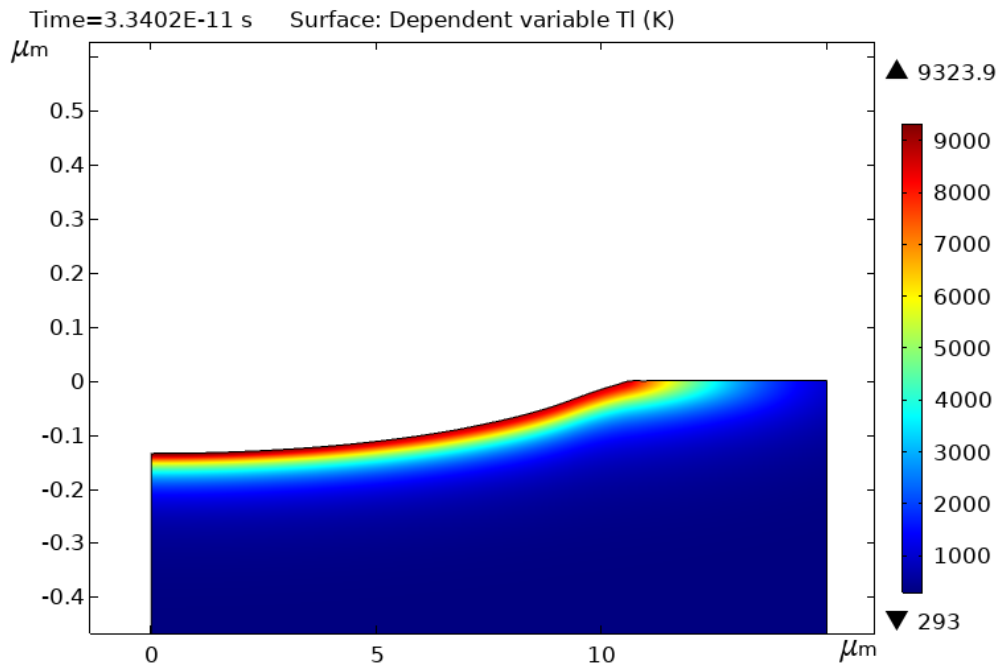


Figure A1 Single pulse crater profile of stainless steel for pulse energy of $6 \mu\text{J}$ and a 10 ps pulsewidth

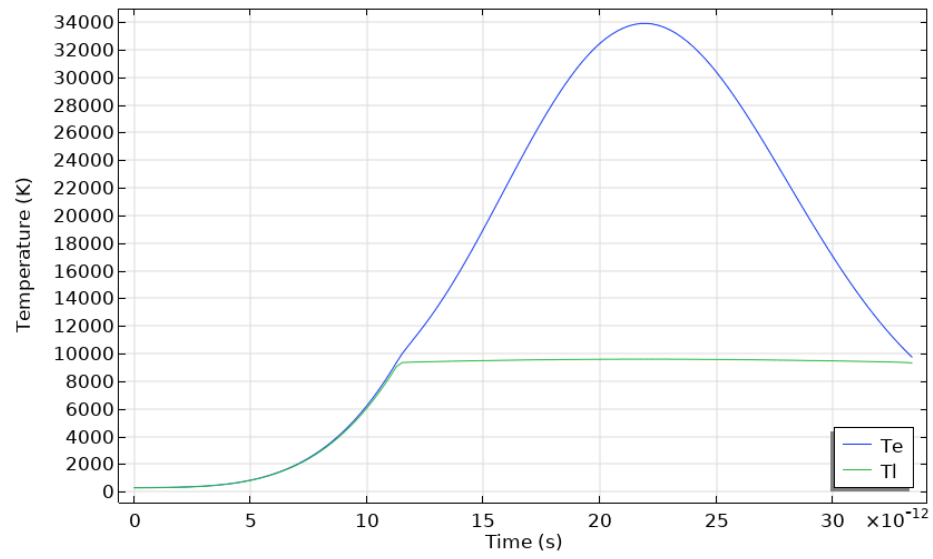


Figure A2 Electron and lattice temperature over time for single pulse ablation of stainless steel

Curriculum Vitae

Name: Andrew J. Dwyre

Post-secondary Education and Degrees: The University of Western Ontario
London, Ontario, Canada
2016-2020 BESc

The University of Western Ontario
London, Ontario, Canada
2020-2022 MEd

Related Work Experience Teaching Assistant
The University of Western Ontario
2020-2022